



저작자표시-비영리-변경금지 2.0 대한민국

이용자는 아래의 조건을 따르는 경우에 한하여 자유롭게

- 이 저작물을 복제, 배포, 전송, 전시, 공연 및 방송할 수 있습니다.

다음과 같은 조건을 따라야 합니다:



저작자표시. 귀하는 원저작자를 표시하여야 합니다.



비영리. 귀하는 이 저작물을 영리 목적으로 이용할 수 없습니다.



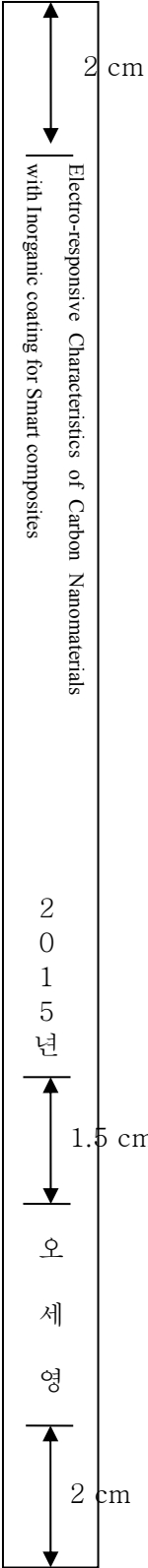
변경금지. 귀하는 이 저작물을 개작, 변형 또는 가공할 수 없습니다.

- 귀하는, 이 저작물의 재이용이나 배포의 경우, 이 저작물에 적용된 이용허락조건을 명확하게 나타내어야 합니다.
- 저작권자로부터 별도의 허가를 받으면 이러한 조건들은 적용되지 않습니다.

저작권법에 따른 이용자의 권리는 위의 내용에 의하여 영향을 받지 않습니다.

이것은 [이용허락규약\(Legal Code\)](#)을 이해하기 쉽게 요약한 것입니다.

[Disclaimer](#)



공학박사학위논문

**Electro-responsive Characteristics of  
Carbon Nanomaterials with Inorganic  
Coating for Smart Composites**

스마트 복합재료를 위한  
무기물이 코팅된 탄소나노물질의 전기응답특성

2015년 8월

서울대학교 대학원

재료공학부

오 세 영

# Electro-responsive Characteristics of Carbon Nanomaterials with Inorganic Coating for Smart Composites

스마트 복합재료를 위한  
무기물이 코팅된 탄소나노물질의 전기응답특성

지도교수 강 태 진

이 논문을 공학박사 학위논문으로 제출함

2015년 5월

서울대학교 대학원

재료공학부

오 세 영

오 세 영의 공학박사 학위논문을 인준함

2015년 7월

위원장 :           윤  재  륜           (인)

부위원장 :           강  태  진           (인)

위원 :           서  용  석           (인)

위원 :           이  승  구           (인)

위원 :           유  웅  열           (인)

**Electro-responsive Characteristics of  
Carbon Nanomaterials with Inorganic  
Coating for Smart Composites**

**ADVISOR: TAE JIN KANG, PROFESSOR**

**BY**

**SE YOUNG OH**

**SUBMITTED FOR THE DEGREE OF  
DOCTOR OF PHILOSOPHY**

**IN THE  
DEPARTMENT OF MATERIALS SCIENCE AND ENGINEERING  
AT  
SEOUL NATIONAL UNIVERSITY**

**AUGUST 2015**

# ABSTRACT

## **Electro-responsive Characteristics of Carbon Nanomaterials with Inorganic Coating for Smart Composites**

Se Young Oh

Department of Materials Science and Engineering

The Graduate School

Seoul National University

The inorganic-coated carbon nanomaterials with anisotropic core-shell structure were fabricated for electrorheological (ER) fluid as well as the fiber webs encapsulating ER fluid were produced via a coaxial electrospinning technique for instantly hardening material.

First, Multi-walled carbon nanotubes (MWNTs) were used to the template for the fabrication of one dimensional nanomaterials with adequate electrical conductivity ( $10^{-7}\sim 10^{-9}$  S/cm) and high elastic modulus. Silica-coated MWNTs (S-MWNTs) and titania-coated MWNTs (T-MWNTs) with cylindrical structure were synthesized to investigate the ER effects of inorganic materials with

different dielectric constant. The electrorheological and dielectric properties of the two different inorganic-coated MWNTs ER fluids were measured using the rheometer and impedance analyzer. The T-MWNTs ER fluids have shown higher dynamic yield stress as well as viscoelastic properties compared to the S-MWNTs ER fluids under external electric field. Furthermore, the T-MWNTs ER fluids have shown higher permittivity and shorter relaxation time of interfacial polarization than those of S-MWNTs. It was caused by intrinsic properties of different inorganic materials which used as shell material.

Second, we prepared S-MWNTs with three different shell thickness and inorganic-coated MWNTs with double layer to modify dielectric properties and electrical conductivity of MWNTs. The electrical conductivity of S-MWNTs decreased with an increase of the shell thickness. However, the dynamic yield stress and viscoelastic properties of S-MWNTs suspension increased with an increase the shell thickness and then decreased to the shell thickness 40 nm. This indicates that the electrical conductivity of particles is an important parameter in the ER performance. In the case of ER fluids with double layer, the dynamic yield stress of silica-titania-coated MWNTs (ST-MWNTs) suspension was higher compared to titania-silica-coated MWNTs (TS-MWNTs) suspension at the same volume fraction. It has been found that the outermost shell material plays an important role in the ER performance.

Third, titania-coated graphene sheets (TCGSs) were synthesized by a sol-gel method to investigate influence of the difference between 1D and 2D

structure and the mixture of T-MWNTs and TCGSs fluids. The  $\Delta\varepsilon'$  value of TCGSs suspension was 2.11, which is similar to the T-MWNTs based ER fluids (2.17). However, the relaxation time of T-MWNTs is faster than that of TCGSs. This is caused by the degree of entanglement and specific surface area between T-MWNTs and TCGSs. Furthermore, mixture effect of T-MWNTs and TCGSs suspension on ER and dielectric properties has been analyzed. The mixture suspension showed the good stability of standing, the enhanced ER performance due to a unique interconnected nanostructure with high contact points and a large surface area, which shows a synergic effect and improves the interfacial interaction between inter-particles and conducting 3D network.

Finally, fiber mats composed inorganic-coated MWNTs ER fluids as core part and poly(ethylene terephthalate) (PET) as shell component were produced using co-axial electrospinning technique for instantly hardening textile. The effect of core particle concentration and external field strength on mechanical properties of fiber mats was investigated. The modulus and tensile strength of the fiber mats is enhanced as well as the breaking elongation is reduced under the external electric field due to the increase of fibrillation number in core part.

**Keywords:** Carbon nanomaterials, Inorganic coating, Electroreological fluids, Smart composites

**Student Number:** 2006-23054

# Contents

<b>ABSTRACT .....</b>	<b>i</b>
<b>CONTENTS .....</b>	<b>iv</b>
<b>LIST OF FIGURES .....</b>	<b>vii</b>
<b>LIST OF TABLES .....</b>	<b>xiii</b>
<b>1. Introduction.....</b>	<b>1</b>
<b>2. Literature Review.....</b>	<b>8</b>
2.1 Electrorheological fluid.....	8
2.1.1 Historical background and definitions.....	8
2.1.2 Mechanisms of the ER effect.....	10
2.1.3 Critical parameters on the ER effect.....	16
2.1.4 The electrorheological materials.....	20
2.1.5 Application of the ER fluid.....	24
2.2 Carbon nanomaterials.....	25
2.2.1 Carbon nanotubes.....	25
2.2.2 Graphene.....	29
2.3 Sol-gel polymerization.....	33
2.4 Electrospinning.....	37
<b>3. Experimental.....</b>	<b>39</b>

3.1 Synthesis of inorganic-coated MWNTs.....	39
3.1.1 Materials.....	39
3.1.2 Preparation of functionalized-MWNTs.....	39
3.1.3 Synthesis of silica-coated MWNTs.....	40
3.1.4 Synthesis of titania-coated MWNTs.....	41
3.1.5 Synthesis of double layer inorganic-coated MWNTs.....	42
3.1.6 Preparation of ER fluids.....	45
3.2 Synthesis of titania-coated graphene sheets.....	46
3.2.1 Materials.....	46
3.2.2 Synthesis of titania-coated graphene sheets.....	46
3.2.3 Preparation of ER fluids.....	48
3.3 Preparation of fiber mats including ERF.....	50
3.3.1 Materials.....	50
3.3.2 Preparation of ER fluids and PET solution.....	50
3.3.3 Coaxial electrospinning setup.....	51
3.4 Measurements.....	53
<b>4. Results and discussion.....</b>	<b>55</b>
4.1 Inorganic-coated MWNTs.....	55
4.1.1 Synthesis and characterization.....	55
4.1.2 Rheological properties.....	71
4.1.3 Dielectrical properties.....	100
4.1.4 Temperature and sedimentation effects.....	107
4.1.5 Summary.....	112

4.2 Titania-coated graphene sheets.....	114
4.2.1 Synthesis and characterization.....	114
4.2.2 Rheological properties.....	122
4.2.3 Dielectrical properties.....	134
4.2.4 The effect of T-MWNTs and TCGSs mixture fluids.....	136
4.2.5 Summary.....	143
4.3 The fiber mats including ER fluid.....	144
4.3.1 Characterization.....	144
4.3.2 Mechanical properties.....	151
4.3.3 Summary.....	157
<b>5. Conclusions.....</b>	<b>158</b>
<b>6. Bibliography.....</b>	<b>161</b>
<b>Korean Abstract.....</b>	<b>182</b>

# LIST OF FIGURES

**Figure 2.1** Scheme of ER fluid behavior of (a) before and (b) after an external electric field is applied.

**Figure 2.2** The classification of ER materials.

**Figure 2.3** Mother of all graphitic forms, Graphene is a 2D building material for carbon materials of all other dimensionalities. It can be wrapped up into 0D buckyballs, rolled into 1D nanotubes or stacked into 3D graphite.

**Figure 2.4** Structure of CNTs. Possible vectors specified by the pairs of integers (n,m) for general carbon nanotubes. Schematic models of single-walled CNTs. armchair CNT, zigzag CNT and chiral CNT.

**Figure 2.5** (a) Energy bands near the Fermi level in graphene. The conduction and valence bands cross at points K and K'. (b) Conic energy bands in the vicinity of the K and K' points. (c) Density of states near the Fermi level with Fermi energy  $E_F$ .

**Figure 2.6** Mechanism for hydrolysis and condensation of alkoxy silanes

**Figure 2.7** Schematic diagram of set up of electrospinning apparatus

**Figure 3.1** Scheme for the fabrication of silica-coated MWNTs (S-MWNTs) and titania-coated MWNTs (T-MWNTs).

**Figure 3.2** Graphical illustration of the synthesis process to fabricate ER particles with various shell sequence such as S-, T-, ST-, and TS-MWNTs. (S: silica, T: titania).

**Figure 3.3** Scheme of graphite oxidation using Hummer's method

- Figure 3.4** Graphical illustration of the synthesis process to fabricate TCGSs
- Figure 3.5** A schematic diagram illustrating the fabrication process of core/sheath structured fibers by the coaxial electrospinning apparatus.
- Figure 4.1** HR-TEM images of functionalized multi-walled carbon nanotubes.
- Figure 4.2** HR-TEM images of S-MWNTs with an average diameter of 60 nm at (a) low and (b) high magnification (scale bar = 100, 20 nm).
- Figure 4.3** HR-TEM images of T-MWNTs with an average diameter of 60 nm at (a) low and (b) high magnification (scale bar = 100, 20 nm)
- Figure 4.4** Line profiles and EDX spectroscopy: (a) the line profiles of Si, O and C recorded along the solid line for S-MWNTs, (b) EDX spectrum of S-MWNTs, (c) the line profiles of Ti, O and C recorded along the solid line for T-MWNTs, and (d) EDX spectrum of T-MWNTs.
- Figure 4.5** FT-IR spectroscopic analysis of (a) F-MWNTs, and (b) S-MWNTs and T-MWNTs synthesized by silica and titania precursor.
- Figure 4.6** The XRD patterns of the (a) F-MWNTs, (b) S-MWNTs and (c) T-MWNTs synthesized by silica and titania precursor.
- Figure 4.7** HR-TEM images of S-MWNTs with shell thickness of 10 nm (a, b), 20 nm (c, d) and 40 nm (e, f) (scale bar = 100, 20 nm)
- Figure 4.8** STEM images and cross-sectional compositional line profiles of core/shell nanotube structure along the diagonal (indicated by a red line) (a) T-MWNTs; (b) ST-MWNTs and (c) TS-MWNTs.
- Figure 4.9** FT-IR spectroscopic analysis of inorganic-coated MWNTs with various sequences.
- Figure 4.10** Shear stress (a)-(b) and shear viscosity (c)-(d) of function of shear rate for suspensions of the S-MWNTs and T-MWNTs with 20nm shell thickness under different electric field strength (5 vol.%, T = 25 °C).

**Figure 4.11** ER efficiency as a function of electric field strength for S-MWNT-20(3, 5, 10), and T-MWNT-20(3, 5) suspensions.

**Figure 4.12** Dynamic yield stress as a function of electric field strength for S-MWNT-20(3, 5, 10), and T-MWNT-20(3, 5) suspensions.

**Figure 4.13** Storage modulus ( $G'$ , solid points) and loss modulus ( $G''$ , open points) as a function of frequency for (a) S-MWNT-20(5) suspensions and (b) T-MWNT-20(5) suspensions under different electric fields ( $T = 25\text{ }^{\circ}\text{C}$ ).

**Figure 4.14** Steady flow curves of shear stress and shear viscosity as the function of shear rate for S-MWNTs suspension with shell thickness of 10 nm (a, d); 20 nm (b, e) and 40 nm (c, f) under external electric field (20 vol.%,  $T = 25\text{ }^{\circ}\text{C}$ ).

**Figure 4.15** (a) Yield stress as a function of electric field strength for S-MWNTs suspensions with different shell thickness of 10, 20 and 40 nm (b) Current density of S-MWNTs suspensions with different shell thickness under electric fields

**Figure 4.16** The electrical conductivity of S-MWNTs as shell thickness.

**Figure 4.17** The shear stress of S-MWNTs suspensions with different shell thickness as a function of particle volume fraction ( $T = 25\text{ }^{\circ}\text{C}$ , 4 kV/mm).

**Figure 4.18** Steady flow curves of shear stress as the function of shear rate for (a) T-MWNT-40, (b) TS-MWNT-40, and (c) ST-MWNT-40 suspension under external electric field ( $T = 25\text{ }^{\circ}\text{C}$ , 20 vol.%).

**Figure 4.19** (a) Yield stress as a function of electric field strength for inorganic-coated MWNT suspensions with different shell sequences, (b) current density of inorganic-coated MWNT suspensions with different shell sequences under electric fields.

- Figure 4.20** Yield stress of inorganic-coated MWNTs suspensions with various shell sequence as a function of particle volume fraction ( $T = 25\text{ }^{\circ}\text{C}$ ,  $4\text{ kV/mm}$ ).
- Figure 4.21** The electrical conductivity of inorganic-coated MWNTs particles with various shell sequence.
- Figure 4.22** Storage modulus ( $G'$ , solid points) and loss modulus ( $G''$ , open points) as a function of frequency for (a) S-MWNT-20(20) suspension under different electric fields and (b) S-MWNTs suspension with different shell thickness under electric field of  $2\text{ kV/mm}$  (c) inorganic-coated MWNTs with various shell sequence under electric field of  $4\text{ kV/mm}$  ( $T = 25\text{ }^{\circ}\text{C}$ ).
- Figure 4.23** Dielectric spectra of suspensions containing S-MWNT-20(5), S-MWNT-20(10), T-MWNT-20(3) and T-MWNT-20(5) nanoparticles ( $T=25\text{ }^{\circ}\text{C}$ ). Fitting lines are generated from the Cole-Cole equation (4.6).
- Figure 4.24** Dielectric spectra of suspensions containing S-MWNT-40, T-MWNT-40, ST-MWNT-40 and TS-MWNT-40 nanoparticles ( $T= 25\text{ }^{\circ}\text{C}$ ,  $5\text{ vol.}\%$ ). Fitting lines are generated from the Cole-Cole equation (4.6).
- Figure 4.25** Temperature dependence of shear stress ( $2\text{ kV/mm}$ , shear rate =  $10.0\text{ s}^{-1}$ ) of S-MWNT-20 and T-MWNT-20 suspension ( $T = 25\text{ }^{\circ}\text{C}$ ,  $5\text{ vol.}\%$ ).
- Figure 4.26** Temperature dependence of dielectric property of ER fluid containing T-MWNT-20 ( $5\text{ vol.}\%$ ). Fitting lines are generated from the Cole-Cole equation (4.6).
- Figure 4.27** S Sedimentation as a function of time for S-MWNT-20(5) and T-MWNT-20(5) suspensions ( $T = 25\text{ }^{\circ}\text{C}$ ).

- Figure 4.28** Sedimentation as a function of time for suspensions including inorganic-coated MWNTs with various core/shell structures ( $T = 25$  °C, 5 vol.%).
- Figure 4.29** (a) TEM image of GO sheets and EDX pattern of the boxed area in (a), (b) TEM image of TCGSs and (c) EDS mapping of titanium (Ti), oxygen (O) and carbon (C), by EDS analysis on the selected area of the TCGSs.
- Figure 4.30** FT-IR spectra of GO sheets and TCGSs.
- Figure 4.31** (a) XRD patterns of GO sheets and TCGSs (b) the magnified XRD patterns of TCGSs.
- Figure 4.32** (a) XPS spectra of the TCGSs and high-resolution XPS spectra of (b) C 1s, (c) O 1s and (d) Ti 2p.
- Figure 4.33** Microscope images of chain formation in a silicone oil suspension of P25 and TCGSs (1 wt% in silicone oil) (a, c) without an electric field and (b, d) with an applied electric field of 1 kV/mm. The gap distance between the two electrodes was 1.0 mm.
- Figure 4.34** (a) Shear stress and (b) viscosity as a function of shear rate for 5 vol.% TCGSs suspension under an applied electric field strength.
- Figure 4.35** Dynamic yield stress and current density as a function of electric field strength for TCGSs and T-MWNTs suspensions with 5 vol.%.
- Figure 4.36** Dynamic yield stress as a function of volume fraction for TCGSs suspensions under external electric field of 4 kV/mm.
- Figure 4.37** Storage modulus ( $G'$ , solid points) and loss modulus ( $G''$ , open points) as a function of frequency for TCGSs suspension with 5 vol.% under different electric fields.
- Figure 4.38** Creep-recovery behavior of ER fluids containing TCGSs with 5 vol.% ( $T = 25$  °C).

**Figure 4.39** Permittivity and dielectric loss factor as a function of the frequency of 5 vol.% TCGSs and T-MWNTs suspension. The dash lines are obtained from equation (4.6).

**Figure 4.40** Dynamic yield stress and current density of T-MWNTs/TCGSs mixture suspensions with 3 vol.% as a function of TCGSs ratio.

**Figure 4.41** (a) Dielectric constant and (b) dielectric loss of T-MWNTs/TCGSs mixture suspensions with 3 vol.% as a function of frequency ( $T = 25\text{ }^{\circ}\text{C}$ ). Fitting lines are generated from the Cole-Cole equation (4.6).

**Figure 4.42** SEM and TEM images of the core (ERF)/sheath (PET) fiber mats with the ST-MWNTs concentrations of (a) 1 wt%, (b) 2 wt%, (c) 4 wt%, and (d) 8 wt%.

**Figure 4.43** SEM and TEM images of the core (ERF)/sheath (PET) fiber mats fabricated at different core flow rates of (a) 0.45 ml/h, and (b) 0.6 ml/h, when the shell flow rate was fixed at 2 ml/h.

**Figure 4.44** Diameter distribution diagrams of the core (ERF)/sheath (PET) fiber (a) as various concentrations of core fluids and (b) as under different core flow rate (4 wt% core particles).

**Figure 4.45** A schematic diagram of tensile test with an electric field.

**Figure 4.46** Typical stress-strain curves of (a) the core (ERF)/sheath (PET) fiber mats as various concentrations of core fluids and (b) fiber mats including 4 wt% core particles as under different external electric fields.

# LIST OF TABLES

- Table 2.1** The experimental characteristics of an ER fluid.
- Table 2.2** The characteristic comparison between CNT and graphene.
- Table 4.1** Absorption bands in the FT-IR spectra of T-MWNTs, S-MWNTs and T-MWNTs synthesized by silica and titania precursor.
- Table 4.2** The elemental composition of various inorganic-coated MWNTs.
- Table 4.3** Optimal parameters in Bingham and CCJ model fitting to flow curves of S-MWNT-20(5) and T-MWNT-20(5) suspensions according to electric field strengths.
- Table 4.4** Optimal parameters in Bingham and CCJ model fitting to flow curves of S-MWNTs suspension with shell thickness of 10, 20 and 40 nm according to electric field strengths.
- Table 4.5** Optimal parameters in Bingham and CCJ model fitting to flow curves of T-MWNT-40(20), TS-MWNT-40(20), and ST-MWNT-40(5) suspensions according to electric field strengths.
- Table 4.6** Dielectric parameters of S-MWNT-20(5), S-MWNT-20(10), T-MWNT-20(3) and T-MWNT-20(5) suspensions obtained from the Cole-Cole fitting.
- Table 4.7** Dielectric parameters of S-MWNT-40(5), T-MWNT-40(5), ST-MWNT-40(5) and TS-MWNT-40(5) suspensions obtained from the Cole-Cole fitting.
- Table 4.8** Dielectric parameters of T-MWNT-20 as temperature changes obtained from the Cole-Cole fitting.

- Table 4.9** Binding energy, FWHM, and peak area percentage of TCGSs, as determined after curve fitting of the XPS high resolution spectra.
- Table 4.10** Dielectric parameters of T-MWNTs/TCGSs mixture suspensions as TCGSs ratio obtained from the Cole-Cole fitting
- Table 4.11** The change in viscosity and conductivity values against core particle concentration.
- Table 4.12** The comparison of dynamic yield stress and  $\tau_y/\phi^2$  of various ER particle suspensions.
- Table 4.13** Tensile properties of the fiber mats without and with an electric field (140 V/mm).
- Table 4.14** Tensile properties of fiber mats including 4 wt% core particles as different electric fields.

# 1. Introduction

Smart protective textiles are materials with properties that can be significantly altered in a controlled fashion by external stimuli, such as stress, temperature, pH, moisture, electric or magnetic fields. Among the smart protective textiles, instantly hardening textiles which can respond to external stimuli have attracted many military researchers' attention. The smart protective textiles maintain their flexibility and wearability in ordinary time, but show the instantly hardening properties in case of emergency. So, one area of research interest is the use of non-Newtonian fluids to augment the performance of current soft armor materials. Magneto-rheological (MR)/ electro-rheological (ER) fluids, which have their viscoelastic and rheological properties altered in the presence of an external field, offer an opportunity to add energy dissipation to the fabric as well as the significant changes in spring rate can be used to control stiffness. MR/ER fluids also introduce the possibility of tuning or switching the fluid in order to affect the impact response of the fabric, since the shear strength or shear viscosity of MR/ER fluids can be adjusted by varying the external field to which they are subjected.

Carbon nanotube (CNT) is an ideal candidate material for bulletproof vests due to its unique combination of exceptionally high elastic modulus and high yield strain. A Young's modulus of about 1000 GPa, strength ranging between 13-53 GPa, and strain at tensile failure predicted to be as high as ~16% typically characterize CNT.

ER fluid comprises a suspension of dielectric or electrical conductive particles in a dielectric carrier liquid. Since the pioneering discovery of ER fluids was reported by Winslow [1], many studies have been carried out to understand the basic physics of ER responses and to correlate the ER performance with the material properties of the ER fluids. The ER fluids have been recognized as a smart and intelligent material. Their structural and rheological changes under the external electric fields are typically reversible and have swift transition between the liquid and the solid state [2-5]. The ER fluids can potentially be used as an interface that translates electrical signals into mechanical signals, opening the possibility of actively controllable clutches, dampers, valves, locks, and impact absorption [6-8]. In order to implement their high potential as ER application, ER fluids are required to show high yield stress or ER efficiency, low current density, wide temperature range stability, dispersion stability, and low off-field viscosity. However, conventional ER fluids based on micro-sized particles are subjected to challenges in practical applications due to the lack of versatile performances and the high sedimentation.

To improve these problems, various substances have been developed such

as dielectric inorganics [9-11], polar polymers [12, 13], semi-conducting polymers [14-16], carbonaceous particles [17-18], mesoporous particles [19, 20], and core-shell particles [21, 22]. Particularly, core-shell structures or one dimensional nano-size materials have received considerable attention in order to obtain remarkable ER properties. ER particles with these structures enhance the longitudinal polarizability and reduce particle sedimentation compared to the conventional granular micro-sized particles. One dimensional nano-size materials such as titanate and silica nanotubes, nanofiber-type conductive polymers and carbon nanotubes were recently investigated as potential ER fluids [23-30].

Carbon nanomaterials, such as carbon nanotubes (CNTs) and graphene, have attracted much attention for various applications, such as transparent conductivity films, field-effect transistors, field emitters, supercapacitors, and high strength composites, due to their superior intrinsic physical properties such as mechanical strength, electrical and thermal conductivity [31-35]. These carbon nanomaterials have been considered for electrorheological (ER) application due to its several attractive features, such as its peculiar nanostructure, high surface area, and good mechanical strength.

However, the carbon nanomaterial suspensions showed short current due to large electrical conductivity and a negative ER effects due to the phase separation to the direction of the electric field under external electric field [36-38]. Moreover, the large van der Waals forces and strong  $\pi$ - $\pi$  interaction

between carbon-based nanomaterials result in weak shear stress and low colloidal stability under electric fields. So, it is inappropriate to use for application of ER fluids. To overcome these problems, many research reported various kinds of inorganic coated carbon-based nanomaterials, i.e. SiO<sub>2</sub>/TiO<sub>2</sub> coated MWNTs [39, 40], GO/TiO<sub>2</sub> nanocomposite [41, 42] or carbon material-polymer mixture particles, i.e. CNTs/PMMA nanocomposites [43], CNTs/PS micro sized particles [44], PANI decorated graphene nanocomposites [45], chitosan/graphene nanocomposites [46]. These materials were fabricated through the crosslinking or assembling of carbon-based materials by covalent or non-covalent approaches in order to tuning the dielectric permittivity and electrical conductivity of nanoparticles.

Combination of graphene with CNTs can produce mixture materials with new structural characteristics and different properties compared to the individual components. These mixture systems can have better functional performance than that of only graphene or CNTs. It is known that bridging between two nanoparticles, such as carbon nanotubes and graphene sheets, brings about a co-supporting network of both carbon nanomaterials [47, 48]. The combination of 2D graphene sheets and 1D carbon nanotubes with its various advantages, such as high aspect ratio, light weight and high surface area and the surface modification, yields a broad scope of promising mixture graphitic nanofillers. Another important reason applying a mixtureization of CNTs and graphene is the agglomeration tendency of the both fillers, which makes it more difficult to

processing composites.

The two most popular theories are the polarization model and the conduction model. The polarization model derived from the Maxwell–Wagner interaction [49] gives a quadratic variation of yield stress under an external electric field. The conduction model exhibits a power law dependency of yield stress under an external electric field [50]. In general, the electrostatic polarization is attributed to interfacial, dipole-orientation, atomic and electronic polarization. Among them, it is known that the interfacial polarization plays an important role in the ER behaviors. The rate of interfacial polarization is considered an important factor to maintain chain-like structures formed by particles dispersed in a medium under an applied electric field.

Smart and high performance textiles have been currently used for protection or have been investigated by researchers for protective applications. Among the fiber fabrication methods, electrospinning has gained growing interest in the past decade because this technique is quite versatile and cost-effective for producing functional nanofibers from variety of materials including polymers, polymer blends, emulsions, suspensions, sol-gels, metal oxides, composite structures as well as nonpolymeric systems [51-56].

Electrospun nanofibers and their nanowebs have remarkable characteristics including a very high specific surface area, pore sizes within the nanoscale and very lightweight. Moreover, the control of the fiber surface morphology, fiber orientation, and cross-sectional configuration, and design flexibility for physical

/chemical modification is quite feasible for obtaining multifunctional electrospun nanofibers. Nanofibers with core-sheath, hollow, or porous structures have many potential applications in microfluidics, photonics, sensor, biomedical and energy storage [57-62].

The objective of this study is to improve electrorheological performances using anisotropic carbon nanomaterials as dispersal phases and to fabricate smart composites encapsulating ERF materials within a polymer sheath well responded to an applied electric field via a coaxial electrospinning technique. Firstly, silica-coated MWNTs (S-MWNTs) and titania-coated MWNTs (T-MWNTs) with one dimensional nano-size were synthesized using sol-gel process with tetraethyl orthosilicate (TEOS) and titanium butoxide (TBT) respectively as precursor for a new ER material. To examine the influence of dielectric constant on ER behavior, S-MWNTs and T-MWNTs with the same thickness of 20 nm were fabricated. Secondly, to investigate the effect of dielectric properties and electrical conductivity on ER fluid we prepared S-MWNTs with three different shell thickness (10, 20, 40 nm) and inorganic-coated MWNTs with double layer. The ER properties of inorganic-MWNTs suspensions were examined under various conditions, such as different shear rate, dynamic oscillatory shear modes, particle volume fraction and electric field strength. Furthermore, the dielectric properties of inorganic-MWNTs ER fluids were examined using impedance analyzer and calculated on the basis of the dielectric loss model using Cole-Cole equation. The dispersion stability and temperature dependence of inorganic-

MWNTs suspensions were examined. Thirdly, we prepared titania-coated graphene sheets (TCGSs) to compare the difference between 1D and 2D structure and mixture effect of TCGSs/T-MWNTs fluid. Finally, we prepared the core (ER fluid)/sheath (PET) fiber mats by coaxial electrospinning process to achieve instantly hardening textile. The mechanical properties of core/sheath fiber mats were investigated as core particle concentration and external field strength. Tensile strength and modulus of fiber mats including ER fluids enhanced with increase the core particle concentration and the external electric fields.

## **2. Literature Review**

### **2.1. Electrorheological fluid**

#### **2.1.1. Historical background and definitions**

The electrorheological effect, called the “Winslow effect”, was first reported by Willis M. Winslow in 1949 [1]. It was reported that the nonaqueous silica suspensions activated with a small amount of water rapidly transformed to solid-phase in the originally liquid-phase material under an electric field. He thought the fluid could be applied in a great deal of electromechanical devices such as clutches, brakes, and valves that can be controlled by an electric field [63]. Although considerable research has examined this interesting effect, commercial application has been limited due to material properties such as narrow temperature range, low dispersion stability, and lack of range of viscosity [64]. These problems have prevented ER fluids from being used practically in industrial applications.

Although MR fluids reported to Jacob Rabinow at the US National Bureau of Standards in the late 1940s [65] are less well known than ER fluids, both fluids are non-colloidal suspensions of polarizable particles having a size on the order of a few microns. So the research about MR fluids was almost concurrent with Winslow's ER fluid work. The late 1940s and early 1950s actually saw more patents and publications relating to MR fluids than to ER fluids [65]. However, for the last two decades, new types of ER materials such as liquid crystal polymer based fluids or core-shell structured particle based fluids have shown stronger effects than the typical ER fluids. Moreover, recently the new kind of ER materials with giant ER effects may be able to overcome the disadvantages of ER fluids [2].

In general, ER fluids are composed of non-conducting or weakly conduction particles dispersed in an insulating liquid. As shown in Figure 2.1, ER fluids show a Newtonian behavior under no electric field, but a Bingham behavior with the yield stress under an external electric field. This specific response is caused by the transient alignment of particles due to the attractive forces among the dipolar moments induced on each particle by the external electric field.

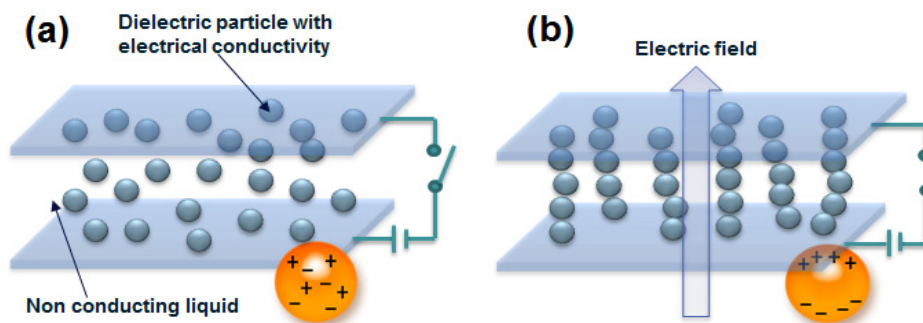


Figure 2.1 Scheme of ER fluid behavior of (a) before and (b) after an external electric field is applied.

### 2.1.2. Mechanisms of the ER effect

Since the innovation of ER fluids, the mechanism of the ER effect has been extremely studied. Various models or mechanisms were proposed to explain the ER phenomena.

The electrical double layer (EDL) model and water bridge mechanism was proposed by Klass [66, 67] and Stangroom [68] to explain a role of water and a relationship between the formation rate of the fibrillation and the ER response. Because the formation rate of the fibrillation would be rather slow compared with the ER response rate, the fibrillation model is inadequate to describe ER phenomena. The ER effect is caused by the distortion of the electric double layer

in the water absorbed on dispersoids under an external electric field. However, the EDL model could not explain the experimental results which showed an increase of rheological properties of several orders of magnitude. And anhydrous electrorheological fluids could not be explained by the EDL model and water bridge model.

The polarization models is relate to the material parameters, such as the dielectric properties of the liquid and solid particles, the particle volume fraction, the electric field strength, etc., to the rheological properties of the whole suspension, in combination with other microstructure features. Using an idealized physical model ER system - a uniform, hard dielectric sphere (real dielectric constant  $\varepsilon_p$ , diameter  $2r$ ) dispersed in a Newtonian continuous medium (real dielectric constant  $\varepsilon_m$ ), the derived electrostatic force was found to be dependent on the dielectric constant mismatch between the particle and continuous medium [69-75]. A universal form could be written as:

$$F = k\varepsilon_m(2r)^2 f^2 E^2 S \quad (2.1)$$

where,  $F$  is the electrostatic force,  $k$  is a constant,  $f = (g - 1) / (g + 2)$  and  $g = \varepsilon_p / \varepsilon_m$ ,  $S$  is a factor related to the particle microstructure.

The shear modulus would increase linearly with the dielectric constant ratio

$\varepsilon_p / \varepsilon_m$  [50], indicating that a high particle dielectric constant would give a strong ER effect. The material of an extremely high dielectric constant was thus used experimentally as the solid particulate phase of the ER fluid, and a strong ER effect was anticipated according to the derivation of the polarization model.

A barium titanate suspension ( $\text{BaTiO}_3$ , its dielectric constant approx. 2000), however, presents a surprising result: inactive under a dc field, and active after adsorbing a small amount of water [76, 77] or being stimulated by an ac field [78]. Clearly, the polarization model fails to describe other important ER experimental observations, such as the rheological property dependence on the electric field frequency and the particle conductivity.

After that, modifications were made to the polarization model. Atten [79] and Foulc [80] thus proposed a conduction model in which the ER effect was thought to be determined by the particle-to-liquid conductivity ratio  $\sigma_p / \sigma_m$  if  $\sigma_p > \sigma_m$ ; if  $\sigma_p < \sigma_m$ , a negative ER effect would be expected. The conduction model could successfully explain ER phenomena that are unexplainable by using the polarization model. It could predict the current density, the yield stress and the temperature dependence of the ER suspension. However, the conduction model can only be used for the situation where the suspension microstructure has been fully formed.

The conduction model only considers the particle interaction, regardless of the microstructure change after an electric field is applied. It therefore could not

give an explanation of the dynamic phenomena, such as the response time of ER fluid. However, they cannot still predict the yield stress based on the physical properties of ER suspension components and on the operating conditions (field strength, temperature, frequency, etc.).

Hao and co-workers [81-83] proposed a dielectric loss model to understand the ER mechanism on the basis of their experimental findings. This model emphasized two dynamic processes such as the particle polarization process and particle turning step. Particle turning step was determined by the particle dielectric loss. The second step is the most important one, which distinguishes the ER particle from non-ER particle. In other words, both the ER particle and non-ER particle could be polarized under an electric field, however, the ER particle could re-orientate along the electric field direction, building the fibrillated bridges between two electrodes. The non-ER particle does not have such ability. The possible reason is that the ER particle has a comparatively high dielectric loss tangent, approximately 0.1 at 1000 Hz, which could generate a large amount of bounded surface charge. The non-ER particle could not gain enough surface charge due to its low dielectric loss. Although they still could be polarized, the total inter-particle force would be cancelled out owing to the diversity of particle dipole vectors. Based on this fact, Hao et al. theoretically came to the conclusion that the particle dielectric loss tangent maximum value should be larger than 0.10, which agrees well with the empirical criteria put forward before [84].

Assuming that the static dielectric constants of the liquid medium and the particle are  $\epsilon_{sm}$  and  $\epsilon_{sp}$  respectively, and  $T$  is temperature, a strong positive ER effect will occur if  $4\epsilon_{sm} < \epsilon_{sp}$  and  $d\epsilon_{sp}/dT > 0$ . A weak or no ER effect is expected if  $4\epsilon_{sm} < \epsilon_{sp}$  and  $d\epsilon_{sp}/dT < 0$ , and equation (2.2) is satisfied; a negative ER effect is anticipated if  $4\epsilon_{sm} < \epsilon_{sp}$  and  $d\epsilon_{sp}/dT < 0$ , and equation (2.3) is satisfied.

$$\frac{d\epsilon_{sp}/dT}{d\epsilon_{sm}/dT} < \frac{(1+3\Phi)(2\epsilon_{sm} + \epsilon_{sp})^3 + 54\Phi^2\epsilon_m(\epsilon_{sp}^2 - 1.5\epsilon_{sm}\epsilon_{sp} - \epsilon_{sm}^2)}{27\Phi^2\epsilon_{sm}^2(\epsilon_{sp} - 4\epsilon_{sm})} \quad (2.2)$$

$$\frac{d\epsilon_{sp}/dT}{d\epsilon_{sm}/dT} > \frac{(1+3\Phi)(2\epsilon_{sm} + \epsilon_{sp})^3 + 54\Phi^2\epsilon_m(\epsilon_{sp}^2 - 1.5\epsilon_{sm}\epsilon_{sp} - \epsilon_{sm}^2)}{27\Phi^2\epsilon_{sm}^2(\epsilon_{sp} - 4\epsilon_{sm})} \quad (2.3)$$

If  $4\epsilon_{sm} > \epsilon_{sp}$ , physically  $d\epsilon_{sp}/dT$  would unlikely be less than zero, thus a weak or negative ER effect would become possible at this condition. A yield stress equation was derived on the basis of the dielectric loss mechanism described above. Assuming that only interfacial polarization would contribute to the ER effect and the ER particle would form the bct structure under an electric field, a yield stress equation could be expressed as [83]:

$$\tau_y = \frac{126\Phi^2 E^2}{4\pi(1-\Phi) - 18\Phi} \times \left\{ \begin{aligned} & -\frac{3\varepsilon_{sm}(\xi^2 + \xi - 2)}{(2 + \xi)^3} + \frac{2\beta_m T(\xi^2 - 1.5\xi - 1)(\varepsilon_{sm}^2 + \varepsilon_{sm} - 2)}{(2 + \xi)^3} \\ & + \frac{T\beta_p p(\xi - 4)(\varepsilon_{sm}\xi + 2)^2}{(2 + \xi)^3} \end{aligned} \right\} \quad (2.4)$$

where,  $\tau_y$  is the yield stress,  $\beta_m$  and  $\beta_p$  are the liquid medium and solid particle linear expansion coefficient, respectively,  $\xi = \varepsilon_{sp} / \varepsilon_{sm}$ ,  $p = [(n-1)p_s - (n+2)p_\infty]$ ,  $n$  is a constant, between 4 and 19.7,  $p_s = (\varepsilon_{sp} - 1) / (\varepsilon_{sp} + 2)$ , and  $p_\infty = (\varepsilon_{\infty p} - 1) / (\varepsilon_{\infty p} + 2)$ .

Equation (2.4) indicates that the yield stress of ER fluid would increase with the square of the applied electric field and the particle volume fraction. If  $p$  is a positive value, the yield stress thus will increase with  $\xi$  increasing, as the numerator increases much faster than the denominator with  $\xi$ . However, if  $p$  is a negative value, then the yield stress will decrease with increasing of  $\xi$ , which cannot be explained by the polarization model.

### 2.1.3. Critical parameters on the ER effect

The ER effect depends on the applied electric field strength, frequency of the electric field, particle conductivity, particle dielectric properties, particle volume fraction and temperature etc.

#### - The electric field strength

The yield stress of an ER fluid extremely depends on the applied electric field strength. The critical electric field strength ( $E_c$ ) exists and the yield stress linearly increases with the electric field [85] :

$$\tau_y = k(E - E_c) \quad (2.5)$$

where,  $\tau_y$  represents the yield stress of an ER fluid,  $k$  is a constant,  $E$  is the applied electric field strength. However, other researchers [86-88] asserted that the yield stress should be proportional to the square of the electric field strength because the yield stress and the apparent viscosity tend to become saturated in high electric field.

### **- Frequency of the electric field**

A dc electric field is generally used to engender an observable ER effect. On the other hand, an ac electric field is very helpful to understand the mechanism of the ER effect and to determine the response time of an ER fluid. Its viscosity and yield stress are expected to decrease with increasing frequency, because it would be unable to catch up with the change of the electric field at high frequency. Hao [89] used the Wanger-Maxwell polarization [90-92] to understand the frequency dependence of the yield stress. He found that the yield stress decrease corresponds to the decrease of dielectric constant of the whole suspension when frequency increases. The particle conductivity determines whether the yield stress decrease appears at high or low frequency. High conductivity particles give an obvious ER effect even in very high frequency fields, indicating a short response time.

### **- Particle conductivity**

Block [14] studied how the particle conductivity influences the ER effect by using the acene-quinone radical polymer/silicone oil, and found that the static yield stress peaks at a particle conductivity of approximately  $10^{-5}$  S/m. A similar tendency was found in the oxidized polyacrylonitrile/silicone oil system [84], however, the yield stress peaks at a particle conductivity of approximately  $10^{-7}$  S/m, rather than  $10^{-5}$  S/m. Besides the influence on the ER effect, the particle conductivity also determines the current density of the whole suspension and the

response time of the ER fluid. The response time was found to be inversely proportional to the particle conductivity [89, 93].

#### **- Particle dielectric property**

Since the ER effect is induced by an external electric field, the polarization is believed to play an important role, and the particle dielectric property should be dominant in the ER effect. Deinega [94] found the dielectric constant increases with the electric field strength (0.4~4 kV/mm), and levels off at high electric field. And Block [14] suggested that the polarization rate and its magnitude are very important for ER response. Kawai [95] and Ikazaki [96] proposed that for a good ER fluid, its dielectric relaxation frequency should be between  $10^2$  and  $10^5$  Hz and the difference of the dielectric constant below and above the relaxation frequency must be large. Hao [84] studied how the particle dielectric properties alter the ER effect. By analyzing the dielectric data of currently used ER materials, an empirical criterion was proposed for selecting ER material: the particle dielectric loss tangent should be approximately 0.10 at 1000 Hz.

#### **- Particle volume fraction**

The yield stress and the apparent viscosity of an ER suspension are largely dependent on the particle volume fraction. A linear relationship between the yield stress and the particle volume fraction was derived on the basis of the

fibrillation model [97]. However, other researchers found theoretically that the yield stress goes through a maximum as the particle volume fraction increases, and the maximum appears at a very high particle volume fraction [98]. Block [14] and Xu [88] found the yield stress parabolically increases with the particle volume fraction. Hao [99] found that there is a critical particle volume fraction for the ER suspension. When the particle volume fraction exceeds this critical value, a sharp increment of the rheological property should be observed.

### **- Temperature**

There are two reasons that temperature might change the ER effect substantially. The first is that temperature can definitely change the polarizability of the ER suspension, as the particle conductivity and dielectric constant vary with temperature. The second is that temperature would directly impact particle thermal motion. If the Brownian motion would be intensified at high temperature, thus the ER effect would become weak. But an improved ER response was found at higher temperatures in several ER suspensions, including both the inorganic and polymeric systems [66, 67, 100, 101]. The change of the particle intrinsic property was thought to be responsible for the ER effect enhancement in an anhydrous ER system. Hao [84] found that the temperature dependence of the yield stress is dependent on the particle conductivity. There is an optimal particle conductivity at which the ER effect peaks. A decrease in shear stress with elevated temperature would be found in a suspension with the

particle conductivity greater than the optimal value, while an increase would be found if the particle conductivity is less than the optimal value.

#### **2.1.4. The electrorheological materials**

The ER particulate material includes inorganic non-metallic, organic and polymeric semi-conductive materials. The inorganic materials are basically the ionic crystalline material, while organic and polymeric semi-conductive materials generally have a  $\pi$  bond conjugated structure, and are electronic conductive materials.

The continuous liquid phase is usually polydimethylsiloxane oil (silicone oil), vegetable oil, mineral oil, paraffin and chlorinated hydrocarbon oils, etc. These oils must have a low conductivity and high breakdown strength. A good ER fluid should have:

- (1) A yield stress should be larger than 5 kPa under an electric field.
- (2) A low current density passing through the ER fluid less than  $20 \mu\text{A}/\text{cm}^2$
- (3) A strong ER effect should work within temperature range  $-30$  to  $120$  °C.
- (4) A short response time. The response time of an ER fluid scales at  $10^{-3}$  s.
- (5) High stability.

The ER fluid should be chemically and physically stable. There should be no particle sedimentation and material degradation problems. The experimental

characteristics of ER fluids are shown in table 2.1.

Before 1985, all ER fluids contained small amounts of water. Such ER fluids have many shortcomings, such as narrow working temperature range due to the water evaporation at high temperatures; high current density due to the higher conductivity of water; and device erosion caused by water, etc. In 1985 Block [102] developed a water-free acenequinone radical polymer ER fluid, which was thought to be a new class ER fluid termed as the anhydrous ER fluid.

Anhydrous ER fluid is believed to be much more promising from the standpoint of industrial applications. It thus received greater attention afterwards, and many other kinds of water-free ER fluids were developed thereafter [103, 104]. In the late 1980s, it was realized that water-free ER fluid had another big problem; particle sedimentation, which could cause the ER fluid to malfunction completely, thus severely limiting practical applications.

Effort was then expended to develop a homogeneous ER fluid with no particulate material inside. Low molecular liquid crystalline (LC) materials were extensively studied. In the early 1960s, the viscosity of LC materials was found to increase under an electric field, though the increment was only a few times [105, 106]. In 1992 an extremely large ER effect was found by Yang and Inoue [107] in certain LC materials. Other LC ER systems were developed later on for the purpose of mechanism study [108-110]. The mechanism of the rheological response of the oil-in-oil emulsion system was addressed by Ha [111] quite recently. Homogeneous ER fluids are believed to offer a new and promising type

of ER fluid. However, higher viscosity under zero electric field and liquid/liquid segregation problems are obvious obstacles for such systems.

In the heterogeneous group, there are inorganic, organic or polymeric particulate materials. In the inorganic group, oxide and non-oxide materials give a quite different ER effect, and are therefore discussed separately. Figure 2.2 shows the tree structure of the ER fluid, and we will follow this classification.

Table 2.1 The experimental characteristics of an ER fluid

	Liquid phase	Particle	ER suspension
Relative dielectric constant	$\sim 2$	$2 \sim 10^4$	
Conductivity (S/m)	$10^{-10} \sim 10^{-16}$	$10^{-7}$	$10^{-9} \sim 10^{-16}$
Viscosity in no electric field (Pa·s)	$0.01 \sim 10$		$0.1 \sim 10$

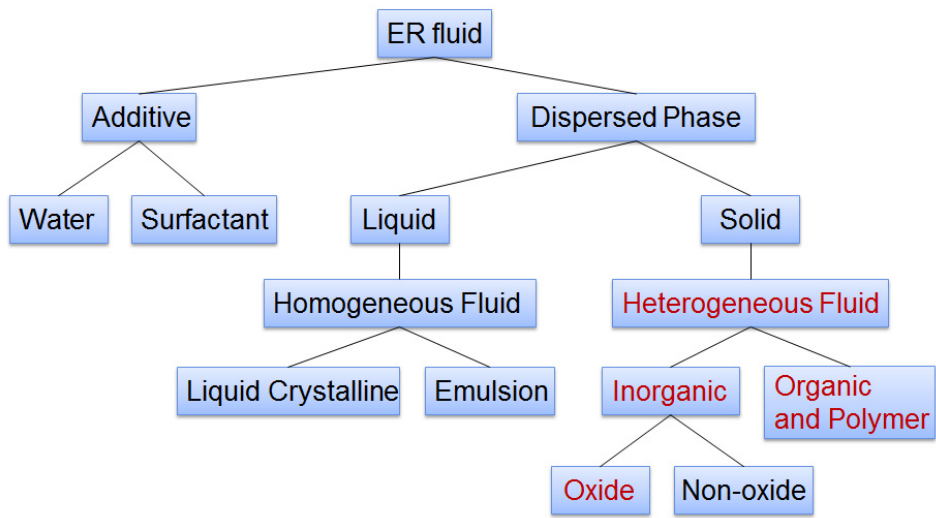


Figure 2.2 The classification of ER materials

### **2.1.5. Application of the ER fluid**

The ER fluid could be used as a mechanical electronic device for transferring and controlling mechanical force. A great number of ER devices have been reported including clutches, brakes, damping devices, actuators, fuel injection valves, hydraulic valves, and body armour [112-118]. In addition, an ER fluid could also be used for a photonic crystal, light shutter, mechanical polisher, display, ink jet printer, human muscle stimulator, mechanical sensor [119-121], etc. Although the ER devices have not yet been commercialized because of many problems, more ER devices will surely be developed in the future.

## **2.2. Carbon nanomaterials**

Carbon-based nanomaterials, composed entirely of  $sp^2$  bonded graphitic carbon, including zero-dimensional (0D) fullerenes, 1D carbon nanotubes (CNTs), and 2D graphene sheets (figure 2.3), have attracted much interest in diverse research fields since their discoveries in 1985, 1991, and 2004, respectively [122-124]. Carbon-based nanomaterials have been employed as the basis of electronic [125-127], optoelectronic [128], photovoltaic [129, 130], sensing [131-133] applications and nanocomposites [134-136] due to their unique structural and physical properties.

### **2.2.1. Carbon nanotubes**

Carbon nanotubes, long thin cylinders of carbon, were discovered in 1991 by Iijima's. Carbon nanotubes are graphitic sheets that are curled up into seamless cylinders, which have revolutionized experimental low-dimensional physics and are utilized in a wide variety of state-of-the-art nano-scientific research. These are cylindrical carbon molecules which are unique for their size, shape and remarkable physical properties. The amazing mechanical and

electronic properties of the nanotubes stem in their quasi-one dimensional (1D) structure and the graphite-like arrangement of the carbon atoms in the shells.

In general carbon nanotubes are synthesized by arc discharge or chemical vapor deposition methods. During the synthesis process, carbon nanotubes possess a wide range of electrical and optical properties stemming not only from their extended sp<sup>2</sup> carbon but also from their tunable physical properties due to the various structure changes such as diameter, length, single-walled, multi-walled and chirality. This is explained by their chiral (or wrapping) vector,  $c$  such that  $c = na_1 + ma_2$  where  $a_1$  and  $a_2$  are the basis vectors of the graphene lattice and  $m, n$  are integers as shown in figure 2.4. Those tubes with chiral vectors of the form  $(n, 0)$  are termed zigzag tubes whereas when  $n = m$  a so-called 'armchair' tube results. All other values of  $n$  and  $m$  produce a chiral tube. Their electronic properties could be changed between metallic or semiconducting simply by varying the tube diameter or their helicity. For example, armchair nanotubes are metallic when  $n - m = 3p$  ( $p$  an integer) the tubes are metallic; otherwise they are semiconducting by changing the values of  $n$  and  $m$ . The carbon nanotubes have also high Young's modulus and tensile strength. Thus carbon nanotubes have been utilized as reinforcing elements for composite materials such as polymers and metal alloys. However, CNT-incorporated composites have difficulty with meeting super high-strength load-bearing materials due to their poor interaction with the matrices and van der Waals force between carbon nanotubes, which leads to inefficient load transfer

from the matrices to the CNTs [137].

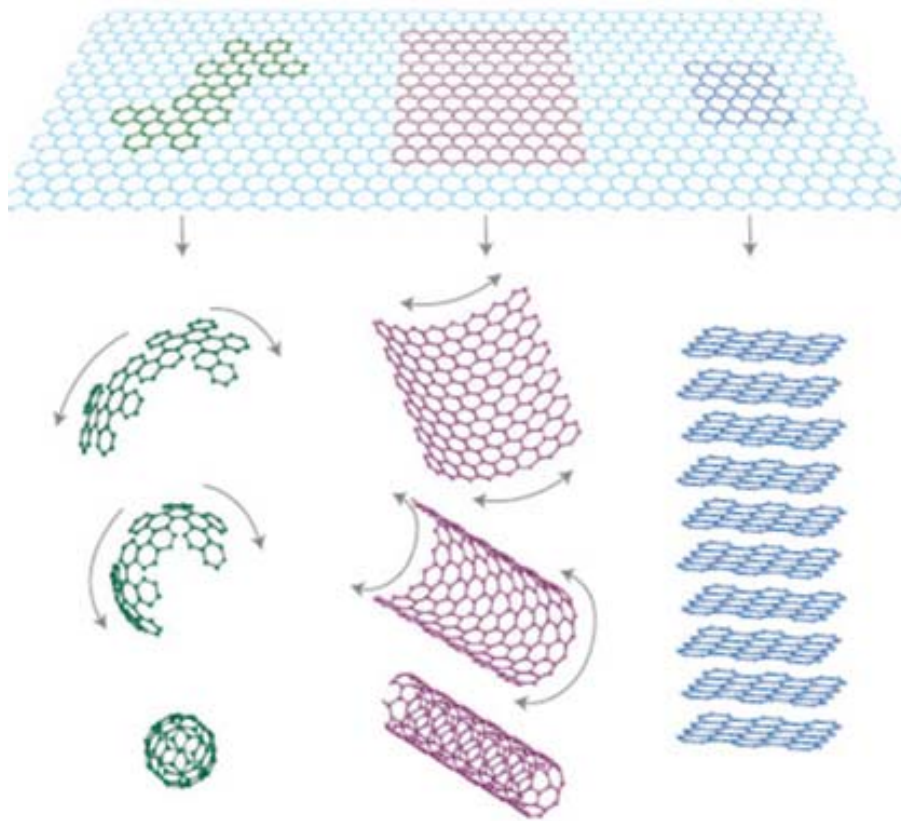


Figure 2.3 Mother of all graphitic forms, Graphene is a 2D building material for carbon materials of all other dimensionalities. It can be wrapped up into 0D buckyballs, rolled into 1D nanotubes or stacked into 3D graphite.

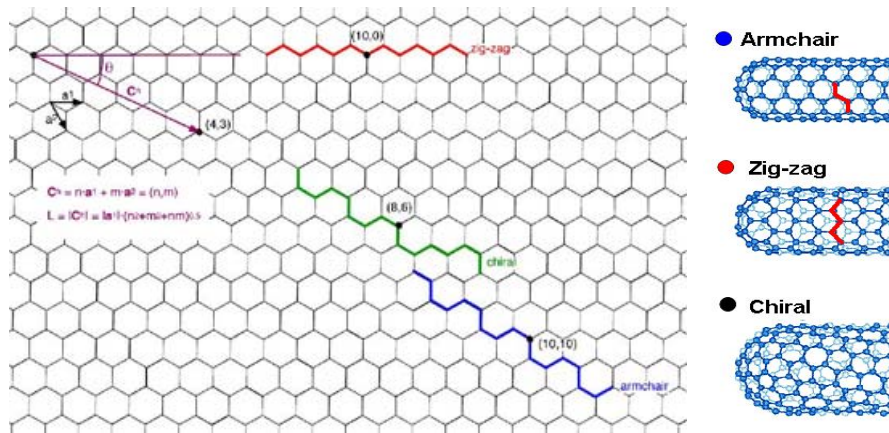


Figure 2.4 Structure of CNTs. Possible vectors specified by the pairs of integers  $(n, m)$  for general carbon nanotubes. Schematic models of single-walled CNTs; armchair CNT, zigzag CNT and chiral CNT.

### 2.2.2. Graphene

Graphene is an allotrope of carbon, whose structure is one-atom-thick planar sheets of sp<sup>2</sup>-bonded carbon atoms that are densely packed in a honeycomb crystal lattice and is a basic building block for graphitic materials. For example, it can be wrapped up into 0D fullerenes, rolled into 1D nanotube or stacked into 3D graphite. Theoretically, graphene has been studied for sixty years [138-140] and widely used for describing properties of various carbon-based materials. Recently, it was realized that graphene provide an excellent condensed-matter analogue of (2+1)-dimensional quantum electrodynamics [141-143], which propelled graphene into a thriving theoretical model. On the other hand, although known as integral part of 3D materials, graphene was presumed no to exist in the free state, being believed to be unstable with respect to the formation of curved structures such as fullerenes and nanotubes. However, since the experimental discovery of graphene by Novoselov group [122], theoretical and experimental studies of the 2D crystals have actively been made.

Previous reported results have shown that the electronic mobility of graphene is very high, with above 15,000 cm<sup>2</sup>/Vs) even under ambient conditions and theoretically potential limits of 200,000 cm<sup>2</sup>/Vs [87, 122, 144, 145]. It is said that graphene electrons act very much like photons in their mobility due to their lack of mass. These charge carries are able to travel sub-

micrometer distances without scattering, which is a phenomenon known as ballistic transport. As shown in figure 2.5, the E-k relation is linear for low energies near the six corners of the two-dimensional hexagonal Brillouin zone, leading to zero effective mass for electrons and holes. Due to this linear or conical dispersion relation at low energies, electrons and holes near these six points, two of which are inequivalent, behave like relativistic particles described by the Dirac equation for spin 1/2 particles. Hence, the electrons and holes are called Dirac fermions, and the six corners of the Brillouin zone are called the Dirac points.

The equation describing the E-k relation is  $E = \hbar v_F \sqrt{k_x^2 + k_y^2}$ , the Fermi velocity is  $v_F \sim 10^6$  m/s.

Another of graphene properties is its inherent strength. Due to the strength of its 0.142 nm carbon bonds, graphene is the strongest material ever discovered, with an ultimate tensile strength of 130 GPa [146], which is a breaking strength 200 times greater than steel or aramid (Kevlar). Graphene is not only extraordinarily strong but also very light at 0.77 mg/m<sup>2</sup>. Using an atomic force microscope (AFM), the spring constant of suspended graphene sheets has been measured. The results showed that spring constant of graphene sheets was in the range 1–5 N/m and the Young's modulus was 0.5 TPa, which differs from that of the bulk graphite. These high values make graphene very strong and rigid.

Finally, graphene has a very high optical transmission with only 2.3%

absorption of white light [147]. This is because the electrons act like massless charge carriers with very high mobility. Graphene's optical properties can be applied such as transparent, conductive electrodes, liquid crystals display and solar cell systems. The different properties between carbon nanotubes and graphene sheets are listed in table 2.2.

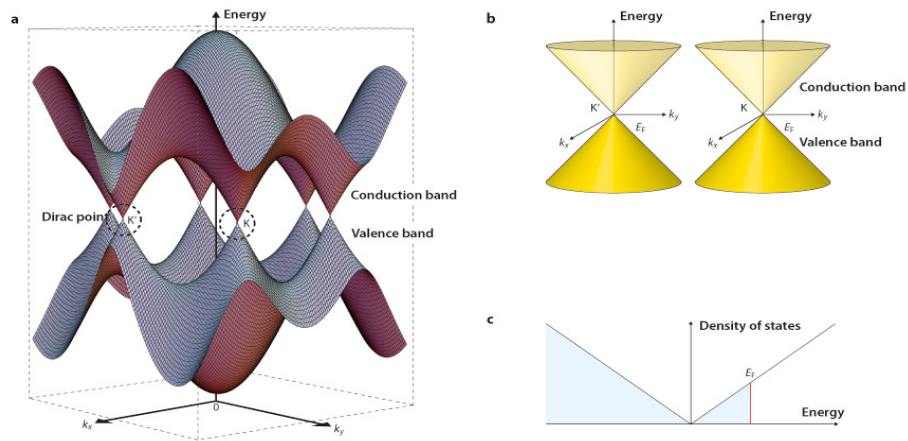


Figure 2.5 (a) Energy bands near the Fermi level in graphene. The conduction and valence bands cross at points  $K$  and  $K'$ . (b) Conic energy bands in the vicinity of the  $K$  and  $K'$  points. (c) Density of states near the Fermi level with Fermi energy  $E_F$ .

Table 2.2 The characteristic comparison of CNT and graphene

	CNT	Graphene
<b>Band-gap</b>	<b>0.5~1.0 eV</b>	<b>0 eV</b>
<b>Carrier mobility</b>	<b>~100,000 cm<sup>2</sup>/V·s</b>	<b>~200,000 cm<sup>2</sup>/V·s</b>
Specific resistance	1.6x10 <sup>-6</sup> ohm·cm	1.0x10 <sup>-6</sup> ohm·cm
Thermal conductivity	3,000 W/Km	5,000 W/Km
Current density	10 <sup>9</sup> A/cm <sup>2</sup>	10 <sup>8</sup> A/cm <sup>2</sup>
Young's modulus	1 TPa	0.9~1.1TPa
Tensile strength	30~180 GPa	120~140 GPa
<b>Surface area</b>	<b>1500 m<sup>2</sup>/g</b>	<b>2630 m<sup>2</sup>/g</b>
<b>Structure</b>	<b>1D</b>	<b>2D</b>

### **2.3. Sol-gel polymerization**

The sol-gel process is a wet-chemical technique widely employed recently in the fields of materials science and ceramic engineering. Such methods are used generally for the fabrication of metal oxide starting from a chemical solution which acts as the precursor for an integrated network of either discrete particles or network polymers. Because sol-gel process can be applied under extraordinarily mild conditions, it can be used to obtain products of various sizes, shapes and formats (e.g., fibers, films, monoliths, and nano-sized particles).

Metal alkoxides and metal chlorides are typically used as precursors, which go through various forms of hydrolysis and condensation reactions. The formation of a metal oxide entails connecting the metal centers with either oxo (M-O-M) or hydroxo (M-OH-M) bridges and generating metal-oxo or metal-hydroxo polymers in solution. Thus the sol evolves towards the formation of a gel-like diphasic system containing both liquid and solid phases whose morphologies range from discrete particles to continuous polymer networks.

The inherent advantages of the sol-gel process are summarized as follows [148]:

- (1) Better homogeneity and purity from raw materials.
- (2) Low processing temperature.
- (3) Effective control of particle size, shape, and properties.

- (4) Production of new composition glasses.
- (5) The creation of new non-crystalline solids outside the range of normal glass formation.
- (6) Mild and easily controlled condition.
- (7) The fine tuning of chromatographic selectivity via the possibility of creating mixture organic-inorganic materials.
- (8) The possibility of designing the material structure and property through the proper selection of sol-gel precursor and other building blocks.

Because of the various advantages, sol-gel technology has found increasing applications in the development of new materials for catalysis [149, 150], chemical sensors [151, 152], membranes [153], fibers [154], optical gain media [155], photochromic and non-linear applications [156-158], and in solid state electrochemical devices [159]. The technology is utilized in a diverse range of scientific and engineering fields, such as the ceramic industry and electronics industry [160].

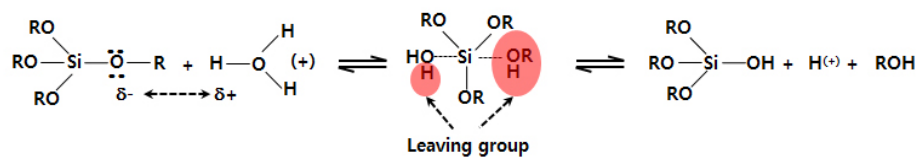
The sol-gel process has two distinct reactions which consist of hydrolysis of the alcohol groups and condensation of the resulting hydroxyl groups. Under acidic conditions, it is likely that an alkoxide group is protonated in a rapid first step. Electron density is withdrawn from the silicon atom, making it more electrophilic and thus more susceptible to attack from water. This results in the formation of a penta-coordinate transition state with significant SN<sub>2</sub>-type

character. The transition state decays by displacement of an alcohol and inversion of the silicon tetrahedron, as seen in Figure 2.6.

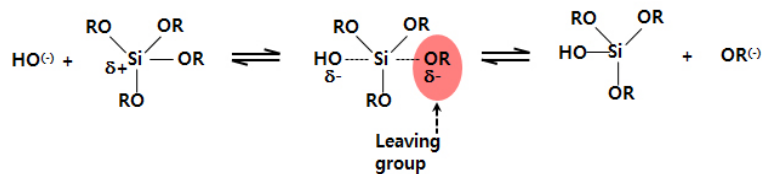
On the other hand, base-catalyzed hydrolysis of silicon alkoxides proceeds much more slowly than acid-catalyzed hydrolysis at an equivalent catalyst concentration. Basic alkoxide oxygens tend to repel the nucleophile,  $\text{-OH}$ . However, once an initial hydrolysis has occurred, following reactions proceed stepwise, with each subsequent alkoxide group more easily removed from the monomer than the previous one. Therefore, more highly hydrolyzed silicones are more prone to attack. Additionally, hydrolysis of the forming polymer is more sterically hindered than the hydrolysis of a monomer. Although hydrolysis in alkaline environments is slow, it still tends to be complete and irreversible.

Thus, under basic conditions, it is likely that water dissociates to produce hydroxyl anions in a rapid first step. The hydroxyl anion then attacks the silicon atom. Again, an  $\text{S}_{\text{N}}2$ -type mechanism has been proposed in which the  $\text{-OH}$  displaces  $\text{-OR}$  with inversion of the silicon tetrahedron.

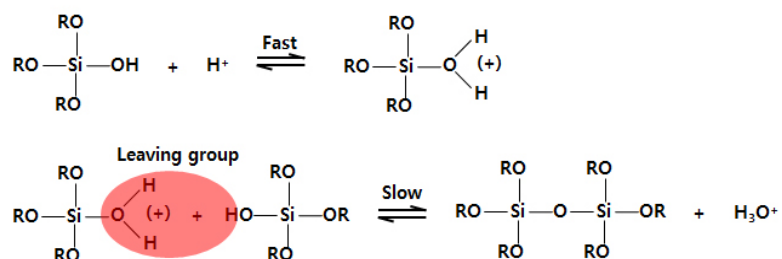
### Acid-Catalyzed Hydrolysis



### Base-Catalyzed Hydrolysis



### Acid-Catalyzed Condensation



### Base-Catalyzed Condensation

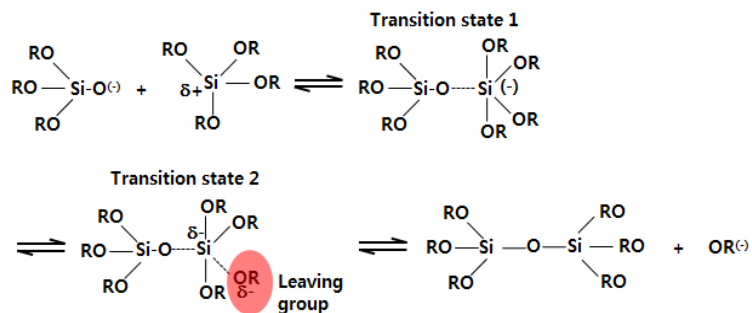


Figure 2.6 Mechanism for hydrolysis and condensation of alkoxy silanes.

## 2.4. Electrospinning

Electrospinning technique is a unique approach using electrostatic forces to produce fine fibers from polymer solutions or melts. Electrospinning method can obtain fibers with a thinner diameter (from nanometer to micrometer) and a larger surface area than those produced from conventional spinning processes. As shown in figure 2.7, the basic electrospinning set-up consists of the power supply, syringe with metallic needle, syringe pump, and metallic collector. In the electrospinning proceeds, a polymer solution at the end of a capillary tip is subjected to an electric field and an electric charge is induced on the liquid surface due to this electric field. When the electric field applied reaches a critical value, the repulsive electrical forces overcome the surface tension forces. Eventually, a charged jet of the solution is ejected from the tip of the Taylor cone and an unstable and a rapid whipping of the jet occurs in the space between the capillary tip and collector which leads to evaporation of the solvent [161]. In order to fabricate high quality nanofibers, the material and processing parameters should be controlled. The fluid parameters are viscosity, electrical conductivity, dielectric constant, and surface tension whereas the processing parameters are flow rates, applied voltage, and tip-to-collector distance, etc [162]. The core/shell nanofibers are applied to a great number of potential

applications due to the unique structural and functional properties. Indeed, the co-axial electrospun nanofibers have showed their multi-functionality by combining the core and shell materials such as drug delivery [163], photocatalyst [164], and lithium ion battery electrode [165].

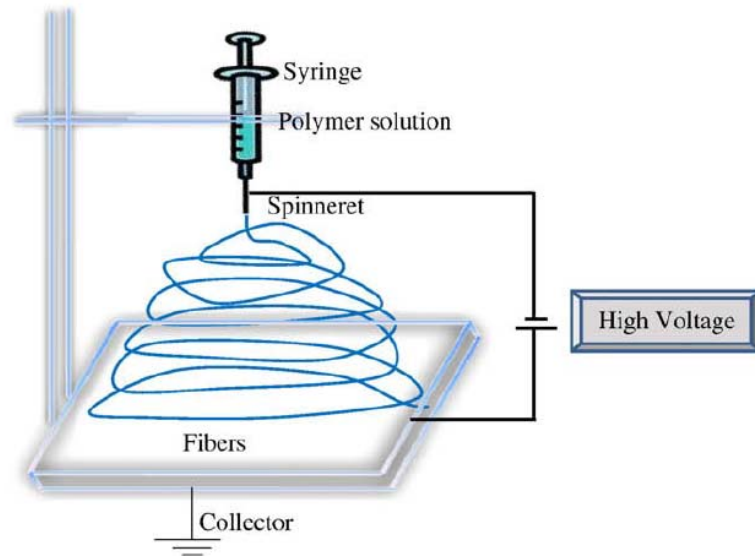


Figure 2.7 Schematic diagram of set up of electrospinning apparatus

## **3. Experimental**

### **3.1. Synthesis of inorganic-coated MWNTs**

#### **3.1.1. Materials**

The MWNTs (diameter 20-40 nm) were purchased from Hanwha Nanotech. Nitric acid ( $\text{HNO}_3$ ) and sulfuric acid ( $\text{H}_2\text{SO}_4$ ) were used for oxidation of MWNTs. The ethanol, ammonium hydroxide ( $\text{NH}_4\text{OH}$ , 28~30 %), tetraethoxysilane (TEOS) and titanium butoxide (TBT) were used for synthesis of the silica/titania coated MWNTs with core/shell structure. Silicon oil (50 cs, shinetsu) was used as a medium to prepare the ER fluids.

#### **3.1.2. Preparation of functionalized-MWNTs**

F-MWNTs were prepared from MWNTs with a purity of 95% using a mixed solution of  $\text{HNO}_3$  and  $\text{H}_2\text{SO}_4$ . The purpose of acid treatment is to remove transition metal and to introduce functional groups ( $-\text{COOH}$ ,  $-\text{OH}$ ,  $\text{C}=\text{O}$ ) on the

MWNTs surface for subsequent process. 0.3 g of unrefined MWNTs was added to 400 ml of HNO<sub>3</sub> and H<sub>2</sub>SO<sub>4</sub> mixed solution (1:1 volume ratio) and maintained at 100 °C for 24 h under a reflux system. The product was filtrated and washed 5 times with deionized water, and dried in vacuum for 24 h.

### **3.1.3. Synthesis of silica-coated MWNTs**

F-MWNTs (50 mg) was ultrasonically dispersed into ethanol (100 ml) for 1 h and stirred for 15 min. After dispersion, NH<sub>4</sub>OH (4 ml, 28~30 vol.%) and distilled water (4 ml) were added to the mixture of ethanol and F-MWNTs. The mixture was treated by bath sonicator for 30 min and was stirred vigorously for another 15 min to obtain a stable and homogeneous suspension. The TEOS (4ml) was quickly injected into the flask and the reaction vessel was stirred vigorously at room temperature for 12 h [166]. The S-MWNTs with three different thicknesses (10, 20 and 40 nm) were obtained by controlling the amount of TEOS, H<sub>2</sub>O and NH<sub>4</sub>OH. After synthesis, the prepared solution is centrifuged at a 4000 rpm for 30 min. In order to fully remove free silica particles, the resultant sediment is ultrasonically re-dispersed in ethanol for 15 min. The same procedure is repeated cycling of the three times. Finally, the darkish product was washed by ethanol and water solution until the supernatant became colorless using 1 µm membrane filter and dried under a vacuum for 24 h.

### **3.1.4. Synthesis of titania-coated MWNTs**

To fabricate the titania-coated MWNTs, F-MWNTs (50 mg) was ultrasonically dispersed into ethanol (100 ml) for 1 h and stirred for 15 min. After dispersion, distilled water (1 ml) was added to the mixture of ethanol and F-MWNTs. The mixture was treated by bath sonicator for 30 min and was stirred vigorously for another 15 min to obtain a stable and homogeneous suspension. The TBT (2 ml) was quickly injected into the flask and the reaction vessel was stirred vigorously at room temperature for 4 h. After synthesis, the prepared solution was centrifuged at a 4000 rpm for 30 min. In order to fully remove free titania particles, the resultant sediment was ultrasonically re-dispersed in ethanol for 15 min. The same procedure was repeated cycling of the three times. Finally, the darkish product was washed by ethanol and water solution until the supernatant became colorless using 1  $\mu\text{m}$  membrane filter and dried under a vacuum for 24 h. Figure 3.1 shows a schematic diagram of the silica-coated MWNTs (S-MWNTs) and titania-coated MWNTs (T-MWNTs) fabricated by sol-gel synthesis.

### **3.1.5. Synthesis of double layer inorganic-coated MWNTs**

To fabricate the silica (inner shell)/titania (out shell)-coated MWNTs, S-MWNTs (100 mg) with coating thickness of 20 nm was ultrasonically dispersed into ethanol (100 ml) for 1 h and stirred for 15 min. Distilled water (2 ml) and acetic acid (1 ml) was added to the mixture of ethanol and S-MWNTs. The mixture was treated by bath sonicator for 30 min and was stirred vigorously for another 15 min to obtain a stable and homogeneous suspension. The TBT (1 ml) was quickly injected into the flask and the reaction vessel was stirred vigorously at room temperature for 4 h. And To fabricate the titania (inner shell)/silica (out shell)-coated MWNTs, T-MWNTs (75 mg) with coating thickness of 20 nm was ultrasonically dispersed into ethanol (50 ml) for 1 h and stirred for 15 min. Distilled water (1.2 ml) and ammonium hydroxide (1 ml) was added to the mixture of ethanol and T-MWNTs. The mixture was treated by bath sonicator for 30 min and was stirred vigorously for another 15 min to obtain a stable and homogeneous suspension. The TEOS (1 ml) was quickly injected into the flask and the reaction vessel was stirred vigorously at room temperature for 12 h. After reaction is complete, centrifuged, washing and drying procedure of particles were performed sequentially as described in section 3.1.3 above. Figure 3.2 schematically shows the synthesis process to fabricate ER particles with core/shell structure nanotube.

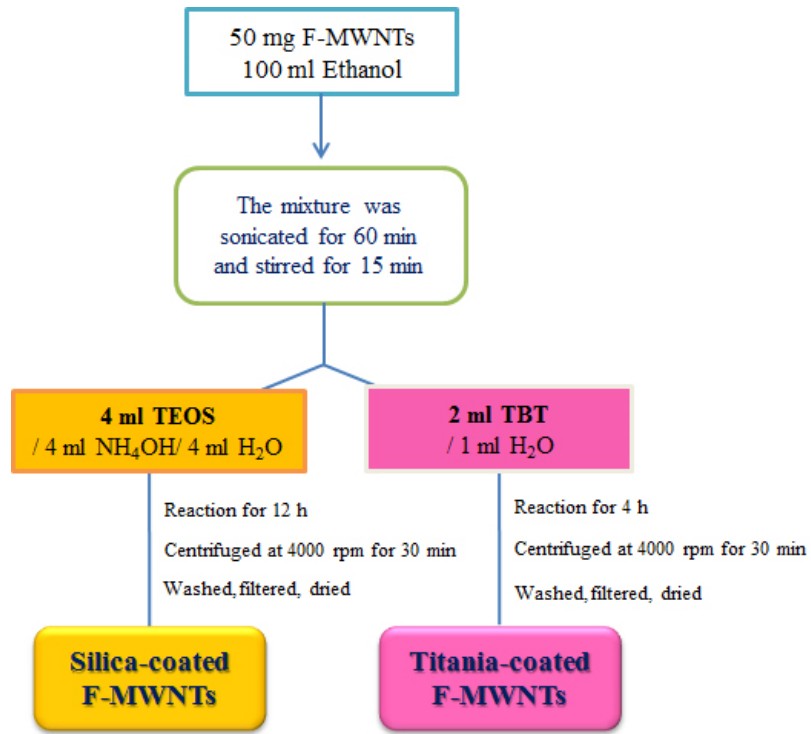


Figure 3.1 Scheme for the fabrication of silica-coated MWNTs (S-MWNTs) and titania-coated MWNTs (T-MWNTs).

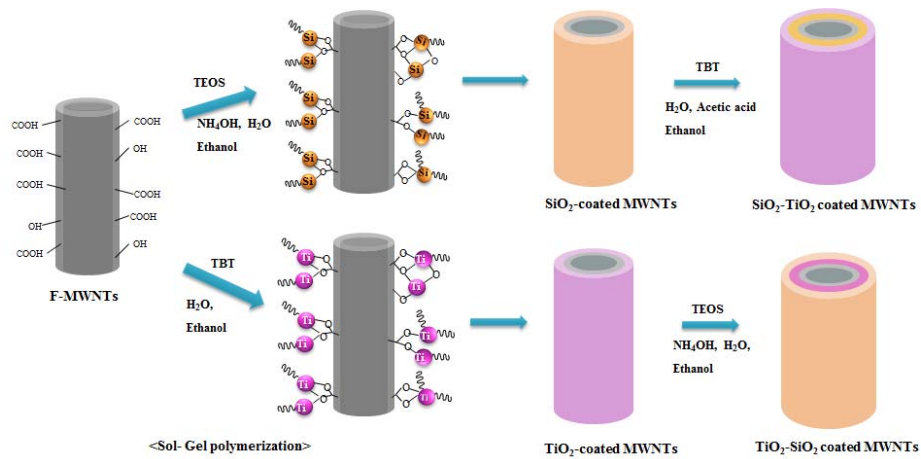


Figure 3.2 Graphical illustration of the synthesis process to fabricate ER particles with varying shell sequence such as S-, T-, ST-, and TS-MWNTs. (S: silica, T: titania).

### **3.1.6 Preparation of ER fluids**

ER fluids were prepared by dispersion of the dry nanoparticles in silicon oil (Dielectric constant of 2.7, viscosity of 50 cS, density of 0.96 g/cm<sup>3</sup> at 25 °C) using mechanical stirring and ultrasonic, respectively. The volume fraction of particles in suspensions was defined as the ratio of the volume of particle to the volume of total suspension. The density of particles was measured in oil medium with a pycnometer. The pycnometer was placed into a shaking water bath to maintain the temperature of samples at 25°C. And then the pycnometer was placed in a chamber connected to a vacuum pump to decrease the effect of porosity on density. The density of particles was calculated through the difference in weight between the ER fluid and oil medium [27]. The volume fraction of various core/shell nanoparticles fabricated by the above procedure was adjusted to 3~20 vol.%.

## **3.2. Synthesis of titania-coated graphene sheets**

### **3.2.1. Materials**

Carbon flake graphite (grade 3763 40 mesh flake) was provided by Asbury Graphite Mills, Inc. Nitric acid ( $\text{HNO}_3$ , 70%) and sulfuric acid ( $\text{H}_2\text{SO}_4$ , 98%) Grade AR was purchased from Samchun Chemical Ltd. Sodium nitrate ( $\text{NaNO}_3$ ), hydrogen peroxide ( $\text{H}_2\text{O}_2$ ), and potassium permanganate ( $\text{KMnO}_4$ ) were obtained from Aldrich Chemical Co. The ethanol and titanium butoxide (TBT) were used for synthesis of the titania-coated carbon based materials. Silicone oil (50 cS, shinetsu) was used for fabrication of the electrorheological fluids.

### **3.2.2. Synthesis of titania-coated graphene sheets**

Graphene oxide (GO) sheets were synthesized from natural graphite powder using a modified Hummers' method as shown in figure 3.3 [167]. Briefly, 2.5 g of graphite and 1.25 g of  $\text{NaNO}_3$  were added in 150 ml of  $\text{H}_2\text{SO}_4$  solution. Then, 7 g of  $\text{KMnO}_4$  were slowly added over about 30 min and continued for 2 h in an ice bath with less than  $-5\text{ }^\circ\text{C}$ . After the mixture was stirred vigorously for 5 days at room temperature, 300 ml of 5 wt%  $\text{H}_2\text{SO}_4$  aqueous solution was slowly

added in resultant made above with kept at 98 °C. Then, reaction was continued at 98 °C for 2h. Finally, the mixture was separated by centrifugation, washed repeatedly with 5 % H<sub>2</sub>O<sub>2</sub> and distilled water, dried in a vacuum oven at 50 °C for 24 h.

GO sheets (20 mg) are ultrasonically dispersed into ethanol (20 ml) for 1 h and stirred for 10 min. Distilled water (2 ml) were added to the mixture. The mixture was treated using a bath sonicator for 30 min and was stirred vigorously for another 15 min to obtain a stable and homogeneous suspension. Immediately afterward, water and TBT (0.5 ml) is injected into the vial under stirring, and kept there for 12h without stirring. The whole reaction is carried out at room temperature. The color of the solution changed from dark yellow to pale yellow during the reaction, indicating that TiO<sub>2</sub> was formed by the sol-gel reaction. After the reaction, the mixture is centrifuged at a 2000 rpm speed. In order to fully remove free titania particles, the resultant sediment is ultrasonically re-dispersed in ethanol for 15min, and vacuum filtered. The same procedure is repeated at three cycles. Finally, the pale yellow product is obtained by filtration through 1µm cellulose mixed membrane and vacuum dried. Figure 3.4 schematically shows the synthesis process to fabricate titania-coated graphene sheets (TCGSs).

ER fluids were prepared by dispersion of the dry nanoparticles in silicone oil (Dielectric constant of 2.2-2.7, viscosity of 50 cS, and density of 0.96g/cm<sup>3</sup> at 25 °C) using a ultrasonic waves and mechanical stirring. To prepare the mixture

suspensions, the T-MWNTs and TCGSs were mixed by various compositions such as 0% T-MWNTs (TCGSs-only), mixture ratio with 10, 30, 50, 70, 90% TCGSs and 100% TCGSs. The particle concentration was fixed at 3 vol% of the total solution weight.

### **3.2.3. Preparation of ER fluids**

ER fluids were prepared by dispersion of the dry TCGSs in silicon oil (Dielectric constant of 2.7, viscosity of 50 cS, density of 0.96 g/cm<sup>3</sup> at 25 °C) using a sonication for 30 min and mechanical stirring for 24 h, respectively. To prepare the mixture suspensions, the T-MWNTs and TCGSs were mixed by various compositions such as 0% TCGSs (T-MWNTs-only), mixture ratio with 10, 30, 50, 70, 90% TCGSs and 100% TCGSs. The particle concentration was fixed at 3 vol% of the total solution weight.

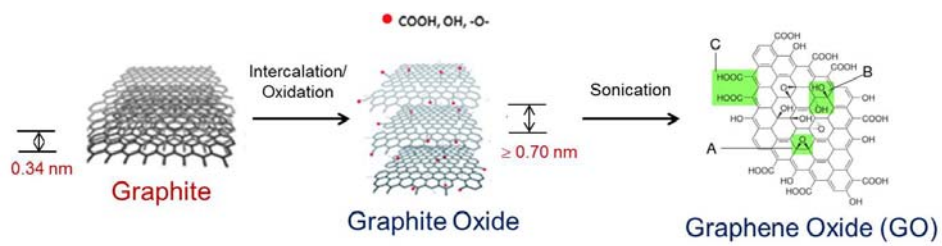


Figure 3.3 Scheme of graphite oxidation using Hummer's method

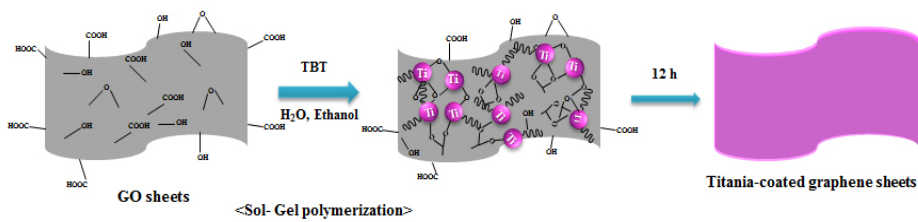


Figure 3.4 Graphical illustration of the synthesis process to fabricate TCGSs

### **3.3. Preparation of fiber mats including ERF**

#### **3.3.1. Materials**

The MWNTs (diameter 20-40 nm) were purchased from Hanwha Nanotech. Nitric acid ( $\text{HNO}_3$ ) and sulfuric acid ( $\text{H}_2\text{SO}_4$ ) were used for oxidation of MWNTs. The ethanol, ammonium hydroxide ( $\text{NH}_4\text{OH}$ , 28~30 %), tetraethyl orthosilicate (TEOS) and titanium butoxide (TBT) were used for synthesis of the inorganic-coated MWNTs nanoparticle. Silicon oil (shinetsu) was used as a medium to prepare the ER fluids. Trifluoroacetic acid (TFA, 99%) was purchased from SAMCHUN chemicals, Korea. Poly (ethylene terephthalate) (PET, Mw 19,200) bright chip was purchased from TORAY SAEHAN.

#### **3.3.2. Preparation of ER fluids and PET solution**

ER fluids were prepared by dispersion of the dried inorganic-coated MWNTs in silicone oil (Dielectric constant of 2.7, density of  $0.96 \text{ g/cm}^3$  at  $25^\circ\text{C}$ ) using mechanical stirring and ultrasonic waves. For core solution, 50 cS and 1000 cS silicone oil were mixed to obtain the solution with the suitable spinning viscosity. The weight fraction of particles was adjusted to 1, 2, 4 and 8 wt%. For

sheath solution with 12 wt%, the PET was dissolved into TFA and stirring vigorously for 6 h.

### **3.3.3. Coaxial electrospinning setup**

The coaxial electrospinning apparatus was schematically represented in Figure 3.5. Coaxial electrospinning was performed with varying flow rates of inner and outer dope to determine appropriate spinning conditions. The basic setup was composed of two syringe pumps, a high power voltage supply, a grounded collector and a coaxial spinneret. The inner and outer spinneret with 16 gauge (1.660 mm) and 21 gauge (0.8 mm) were used for dual capillary, respectively. The shell flow rate fixed to 2.0 ml/h and the core flow rate varied from 0.3 to 0.6 ml/h. The applied voltages ranged from 13 to 15 kV. Distance between spinneret and collector was kept at 15 cm. A colored paper above a flat metal plate is used as a collector.

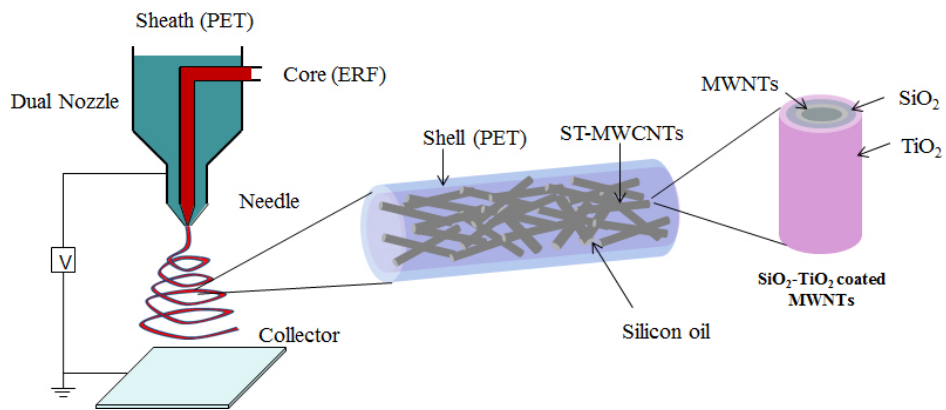


Figure 3.5 A schematic diagram illustrating the fabrication process of core/sheath structured fibers by the coaxial electrospinning apparatus.

### 3.4. Measurements

The morphology of the samples was examined using High Resolution-Transmission electron microscopy (HR-TEM, JEOL-3010F, Japan) and Field Emission Scanning electron microscopy (FE-SEM, JSM-6700F, Japan). The line profiles of elements analysis were observed by Analytical TEM (Tecnai F20, USA). Fourier transform infrared spectrometer (FT-IR, Nicolet 6700, USA) was used to detect the chemical groups on the surface of inorganic-coated nanomaterials. And the crystal structure of the particle was determined by High Resolution X-ray Diffraction pattern (Bruker D8, Germany). Surface chemistry was analyzed by XPS (Sigma Probe, Thermo-VG, UK) with monochromatic Al K $\alpha$  (1486.7 eV) X-ray source and a beam size of 400  $\mu\text{m}$  diameter. The ER performance of suspensions was measured by a stress controlled rotational rheometer (MCR 301, Physica, Germany) equipped with a high voltage power supply (HCP 14-12500, 12.5 kV, 1 mA). With changing the electric field strength, the flow curves were obtained on a wide range of shear rate of 0.1~1000  $\text{s}^{-1}$  with the time interval of 15s at room temperature. The deformation was recorded at the time interval of 15s. Before each measurement, all the suspensions were pre-sheared at shear rate (300  $\text{s}^{-1}$ ) to achieve complete deaggregation of ER particles and then external electric field was applied. The dynamic viscoelastic properties were measured as a function of frequency at a

constant stress in the linear viscoelastic regions. The same test procedure was repeated three times. The dielectric properties of the samples were measured by an impedance analyzer (Agilent 4294A) with a liquid test fixture (16452A, Agilent, USA) in the  $10^2\sim 10^7$  Hz frequency range at room temperature to examine the interfacial polarization. Automatic Hydraulic Press (US, Platen Carver 3894) is used to measure the DC conductivity of particles. DC resistances of ER particles were measured using a Keithly 6517A Electrometer/High Resistance Meter with a Model 8009 Resistivity Test Fixture capable of measuring surface resistivity as high as  $10^{18}$  ohms/cm.

Tensile tests were performed on various core/sheath fiber mat specimens of 100 mm x 20 mm size using a universal testing machine (Instron 5543). We used the electric field generator to apply the uniform field gradient. The electric field intensity was from 100 to 160 V/mm. The specimens were located in the midst of the electric fields device. The apparatus setting was illustrated in figure 4.45. The extension speed was 50 mm/min. At least five specimens were tested for each sample and the tensile properties are reported on average.

## **4. Results and discussion**

### **4.1. Inorganic-coated MWNTs**

#### **4.1.1 Synthesis and characterization**

To examine the ER properties of two different coating materials on MWNTs surface, the silica-coated MWNTs and titania-coated MWNTs were prepared. The silica-coated MWNTs and titania-coated MWNTs were fabricated by using sol-gel process [166, 168-170]. The F-MWNTs were employed as a template material and the silica and titania layer were obtained from reaction of tetraethoxysilane (TEOS) and titanium butoxide (TBT) used as precursor. Nanoparticles with core/shell structure can be coated with silica using the TEOS preferred absorption on the F-MWNTs surface in the presence of ammonium ion ( $\text{NH}_4^+$ ).

The F-MWNTs, as shown in Figure 4.1, have diameters of 15-20 nm and lengths of 2-3  $\mu\text{m}$ . After being synthesized with TEOS, the nanofibrous morphology of F-MWNTs was well preserved but the diameter was increased to

60-70 nm, as shown in Figure 4.2 The average thickness of the SiO<sub>2</sub> coating layer was 20-25 nm. As shown in figure 4.3, the T-MWNTs also have diameters of 60-70 nm and lengths of 2-3 μm. After coating with titania, the core/shell structure was formed and the titania shell thickness was similar to the silica shell thickness of 20-25 nm.

The energy-dispersive analysis of X-ray (EDX) was conducted to characterize the elemental composition of the S-MWNTs and T-MWNTs. As shown in figure 4.4, the formation of core/shell structures and Si, O, and C elements in S-MWNTs and Ti, O, and C elements in T-MWNTs were confirmed by the EDX and the line profiles recorded perpendicular to the long axis of carbon nanotubes in both S-MWNTs and T-MWNTs.

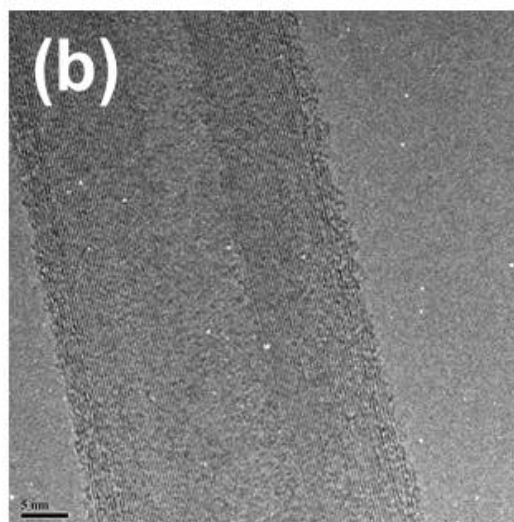
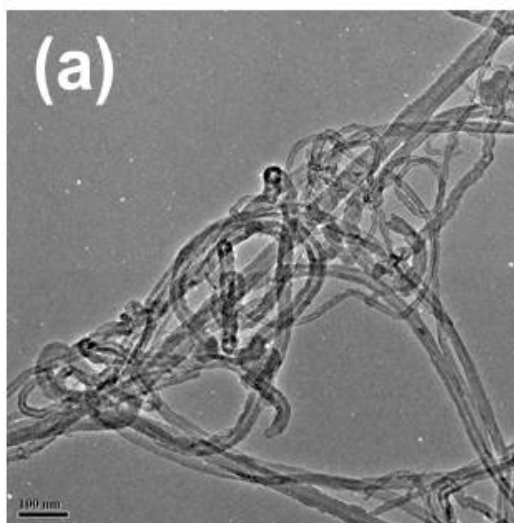


Figure 4.1 HR-TEM images of functionalized multi-walled carbon nanotube

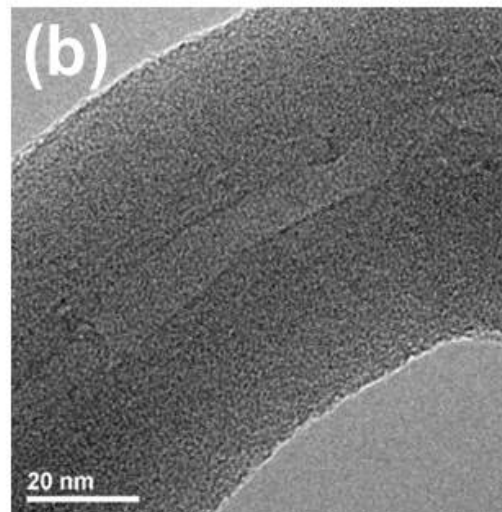
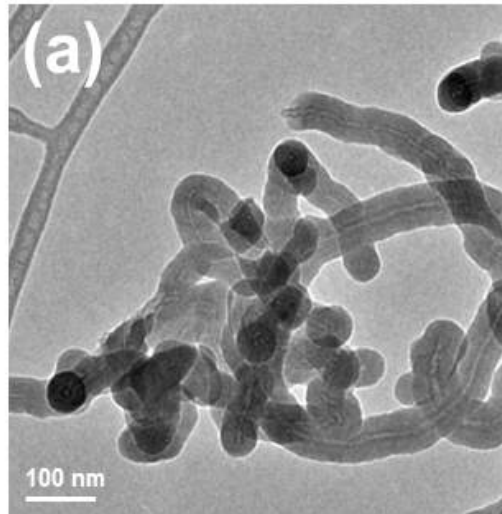


Figure 4.2 HR-TEM images of S-MWNTs with an average diameter of 60 nm at (a) low and (b) high magnification (scale bar = 100, 20 nm).

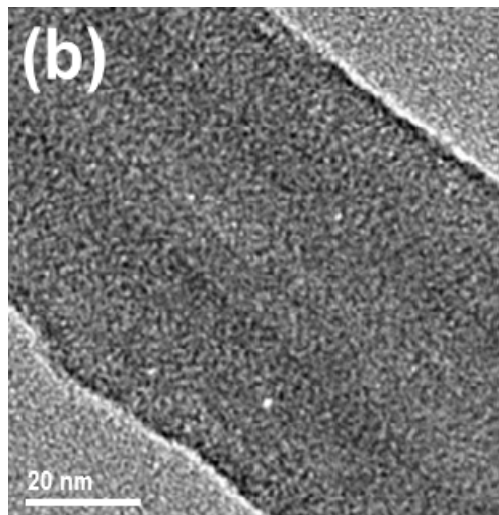
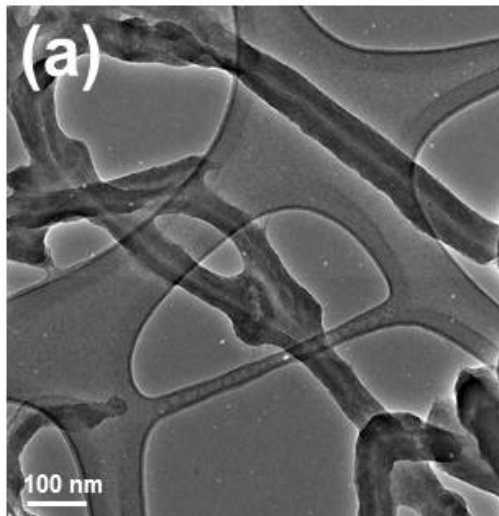
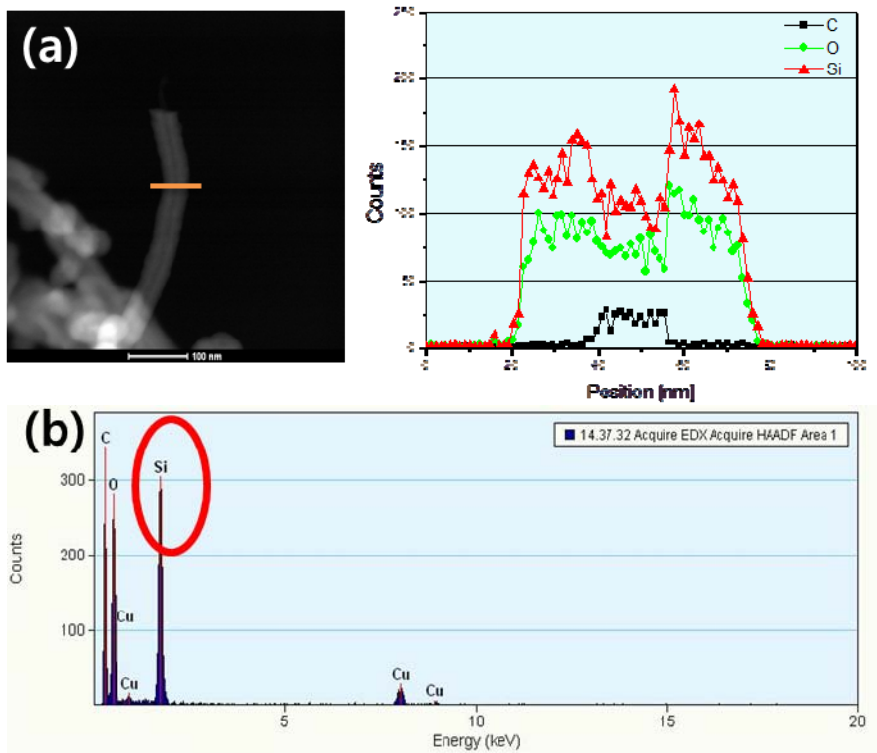


Figure 4.3 HR-TEM images of T-MWNTs with an average diameter of 60 nm at (a) low and (b) high magnification (scale bar = 100, 20 nm).



(continued)

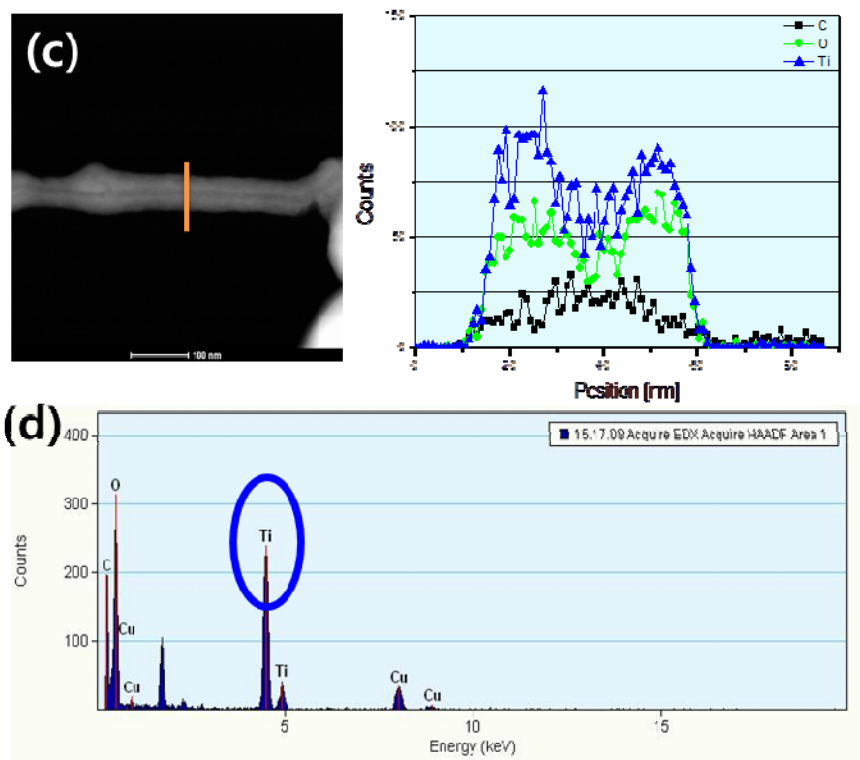


Figure 4.4 Line profiles and EDX spectroscopy: (a) the line profiles of Si, O and C recorded along the solid line for S-MWNTs, (b) EDX spectrum of S-MWNTs, (c) the line profiles of Ti, O and C recorded along the solid line for T-MWNTs, and (d) EDX spectrum of T-MWNTs.

Figure 4.5 shows the IR spectra of F-MWNTs, S-MWNTs and T-MWNTs. Figure 4.5 (a) shows the characteristic five peaks of the C=C stretching ( $1580\text{ cm}^{-1}$ ) and the C-C stretching ( $1413\text{ cm}^{-1}$ ) by MWNTs main chain, the O-H stretching vibrations ( $3420\text{ cm}^{-1}$ ) by hydroxyl group, the C=O stretching ( $1690\text{ cm}^{-1}$ ) and the C-O stretching ( $1160\text{ cm}^{-1}$ ) by carboxyl group. On the other hand, Figure 4.5 (b) shows weak peaks around  $1700$  and  $3430\text{ cm}^{-1}$  corresponding to the carboxyl and hydroxyl group, respectively. The adsorption peak belonging to the Si-O stretching vibration of Si-OH bond appears at  $951\text{ cm}^{-1}$ . The strong absorption peaks at  $1106$ ,  $802$  and  $473\text{ cm}^{-1}$  are respectively attributed to the Si-O-Si asymmetric stretching and the Si-O-Si symmetric vibration which were formed by the hydrolysis and condensation of silica precursor.

In case of CNT/titania nanocomposites, the broad absorption peak located at between  $500$  and  $800\text{ cm}^{-1}$  was assigned to the Ti-O-Ti bond. After silica and titania coating, the carbonyl group band at  $1700\text{ cm}^{-1}$  disappeared. This result indicated that the functional groups such as the -COOH and -C-OH on F-MWNTs were converted to Si-O-C and Ti-O-C bands. The characteristic absorption peaks of F-MWNTs, S-MWNTs and T-MWNTs synthesized by silica and titania precursor are listed in table 4.1.

Figure 4.6 shows the X-ray diffraction patterns of the F-MWNTs, S-MWNTs and T-MWNTs. The F-MWNTs show three major peaks at  $2\theta = 26.0^\circ$ ,  $42.9^\circ$  and  $53.7^\circ$  corresponding to the graphite planes  $(hkl) = (0\ 0\ 2)$ ,  $(1\ 0\ 0)$  and

(0 0 4), respectively. As shown in Figure 4.6(b), only a broad diffraction peak centered at about  $23^\circ$  indicates that the  $\text{SiO}_2$  layers created through sol-gel process have amorphous structure [169]. It was found that amorphous peak of  $\text{SiO}_2$  over-lapped with the (0 0 2) carbon diffraction peak during the silica-coating process. In case of T-MWNTs nanoparticles, the weak diffraction peak was indicated that the synthesized  $\text{TiO}_2$  layer is amorphous structure, as shown in Figure 4.6 (b).

Table 4.1 Absorption bands in the FT-IR spectra of F-MWNTs, S-MWNTs and T-MWNTs synthesized by silica and titania precursor.

Chemical group	Absorption band ( $\text{cm}^{-1}$ )	Chemical group	Absorption band ( $\text{cm}^{-1}$ )
-OH groups	3420	Si-O-Si groups (asymmetric stretching)	1106
C=O groups	1696	Si-OH groups	951
C-O groups	1168	Si-O-Si groups (symmetric vibration)	802
C=C groups	1554	Si-O-Si groups (bending)	473
C-C groups	1413	Ti-O-Ti groups	500-800

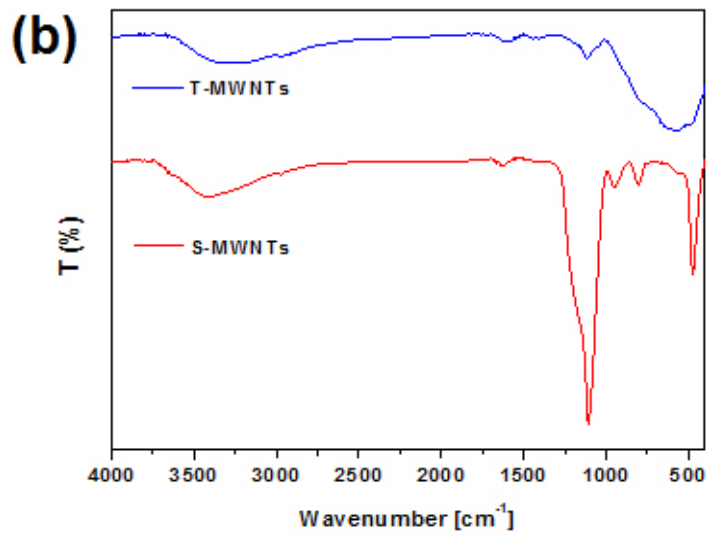
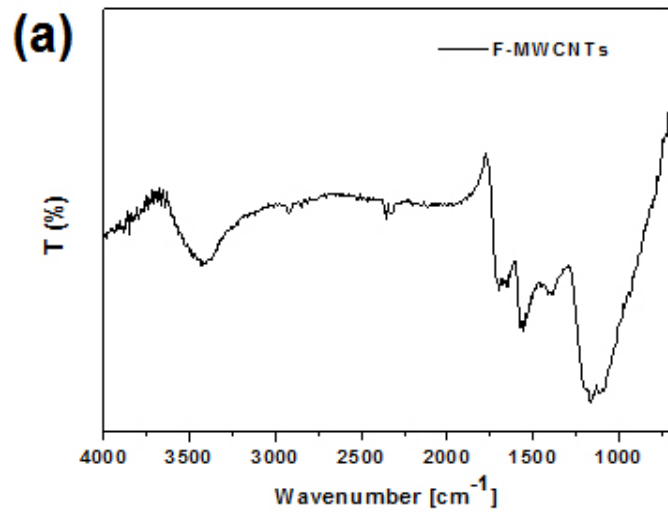


Figure 4.5 FT-IR spectroscopic analysis of (a) F-MWNTs, and (b) S-MWNTs and T-MWNTs synthesized by silica and titania precursor.

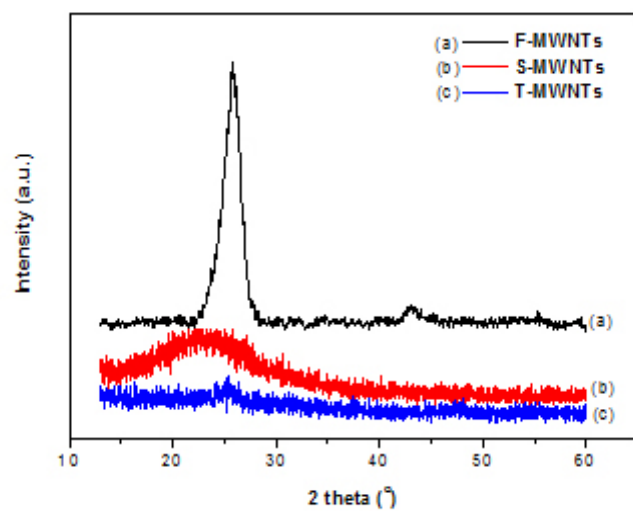


Figure 4.6 The XRD patterns of the (a) F-MWNTs, (b) S-MWNTs and (c) T-MWNTs synthesized by silica and titania precursor.

To examine the effects silica-coating thickness on the ER performance, the silica-coated MWNTs with three different coating thicknesses were prepared by using sol-gel process. Figure 4.7 shows the HR-TEM images of S-MWNTs with shell thickness of 10, 20 and 40 nm. After completion of the reaction, the nanofibrous morphology of F-MWNTs was well preserved as well as the thickness of the silica shell was formed uniformly. However, the shell thickness was gradually increased with increase amount of TEOS, H<sub>2</sub>O and ammonia hydroxide. The average shell thickness of the SiO<sub>2</sub> coating layer was about 10, 20 and 40 nm, respectively.

The energy-dispersive analysis of X-ray (EDX) was conducted to characterize the elemental composition of the silica-coated MWNTs core/shell nanoparticles. Silicon (Si), oxygen (O), and carbon (C) elements originated from F-MWNTs and silica dioxide were confirmed by the EDX. The elemental composition ratio of S-MWNTs with the different thickness and core/shell nanotube particles synthesized by silica is summarized in table 4.2. The increase of the ratio C and Si element indicate that shell thickness are increased with increase of TEOS and ammonia hydroxide amount as well as the silica-coated MWNTs nanoparticles was successfully fabricated.

To investigate the effect of coating sequence on ER activity, the silica/titania coated MWNTs with four different sequences (the silica-, titania-, silica/titania-, titania/silica-coated MWNTs) are prepared. As shown in the Figure 4.8, the formation of core/shell structures and C, O and Ti elements in T-

MWNTs and atomic elements, such as C, O, Si and Ti, of inorganic-coated MWNTs with different shell sequence were confirmed by the TEM image (figure 4.8 (a-c)) and the line profiles (figure 4.8 (d-f)) recorded perpendicular to the long axis of carbon nanotubes, respectively. In order to exclude the effects of the shell thickness on ER performance, shell thickness of all samples was adjusted to 40 nm. And inner- and outer-shell thicknesses of the ST- and TS-MWNTs are controlled to 20 nm, respectively.

Figure 4.9 shows the FT-IR spectra of core/shell nanoparticles with various sequences. As shown the Figure 4.9, however, after coating with silica or titania on the surface of MWNTs, the peaks around 1700 and 3430  $\text{cm}^{-1}$  disappeared in all samples. This result indicated that the functional groups such as the  $-\text{COOH}$  and  $-\text{C}-\text{OH}$  on F-MWNTs were converted to  $\text{Si}-\text{O}-\text{C}$  and  $\text{Ti}-\text{O}-\text{C}$  bands. The adsorption peak belonging to the  $\text{Si}-\text{O}$  stretching vibration of  $\text{Si}-\text{OH}$  bond in the S-40, ST-40 and TS-40 sample appears at 951  $\text{cm}^{-1}$ . The absorption peaks at 1106, 802 and 473  $\text{cm}^{-1}$  are respectively attributed to the  $\text{Si}-\text{O}-\text{Si}$  asymmetric stretching and the  $\text{Si}-\text{O}-\text{Si}$  symmetric vibration which were formed by the hydrolysis and condensation of silica precursor. In case of titania-coated MWNTs, the broad absorption peak located at between 500 and 800  $\text{cm}^{-1}$  was assigned to the  $\text{Ti}-\text{O}-\text{Ti}$  bond. In the case of ST-40 and TS-40, it can be conformed the absorption peak formed by  $\text{Si}-\text{O}-\text{Si}$  bond at between 500 and 800  $\text{cm}^{-1}$  was tilted by  $\text{Ti}-\text{O}-\text{Ti}$  bond.

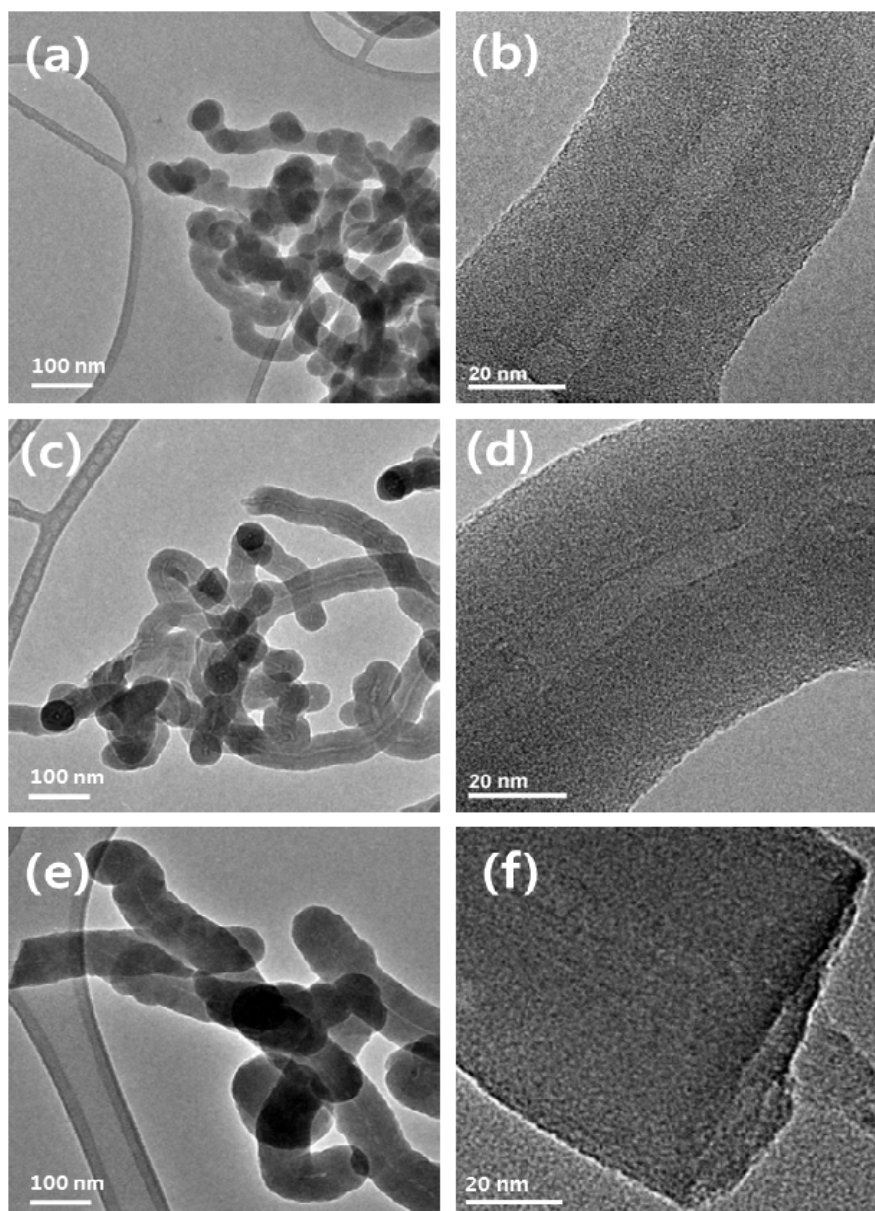


Figure 4.7 HR-TEM images of S-MWNTs with shell thickness of 10 nm (a, b); 20 nm (c, d) and 40 nm (e, f) (scale bar = 100, 20 nm)

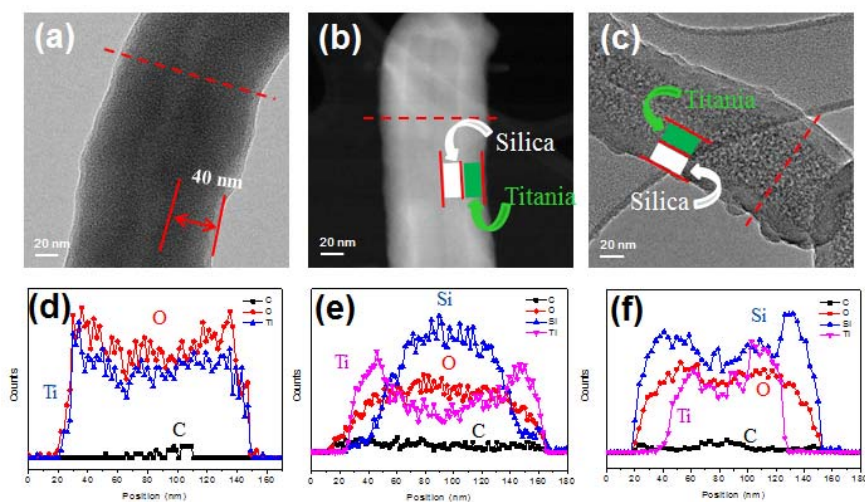


Figure 4.8 STEM images and cross-sectional compositional line profiles of core/shell nanotube structure along the diagonal (indicated by a red line) (a) T-MWNTs; (b) ST-MWNTs and (c) TS-MWNTs.

Table 4.2 The elemental composition of inorganic-coated MWNTs.

Sample	S-10	S-20	S-40	T-40	ST-40	TS-40
C (%)	8.24	3.95	1.85	1.17	3.49	2.21
O (%)	38.51	40.24	41.76	56.58	27.7	30.34
Si (%)	53.25	55.81	56.39	-	37.2	46.25
Ti (%)	-	-	-	42.24	31.15	21.2

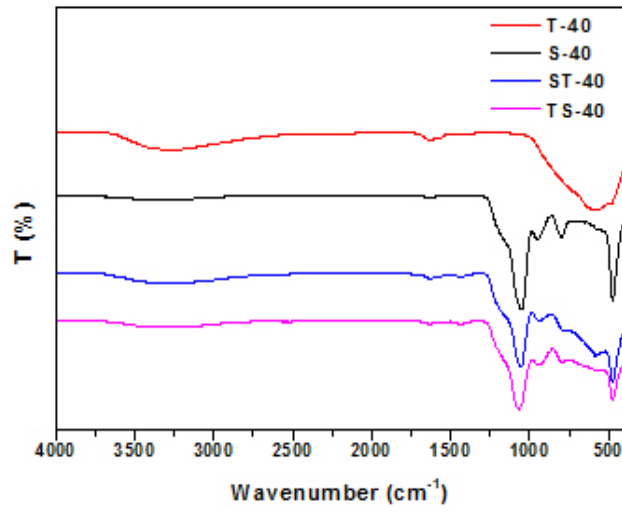


Figure 4.9 FT-IR spectroscopic analysis of inorganic-coated MWNTs with various sequences.

### 4.1.2 Rheological properties

Electro-rheometer studies are conducted to observe the electric field induced reversible viscosity change and ER response of S-MWNTs or T-MWNTs nanoparticle suspensions. Figure 4.10 shows the flow curves of the shear stress versus shear rate and viscosity versus shear rate for ER fluids containing S-MWNTs or T-MWNTs nanoparticles with 20 nm shell thickness of 5 vol.% under external electric fields, respectively. As shown in Figure 4.10 (a)-(b), ER fluids containing S-MWNTs or T-MWNTs nanoparticles show a typical Bingham plastic behavior in the low shear rate region under external electric fields. This Bingham plastic behavior is associated with the chain-like or column-like structures formed by electrostatic interactions between electrically charged particles. This strong interaction was attributed to interfacial polarization between silica or titania coated nanoparticles.

The steady shear behavior of ER fluids is influenced by competition between electrostatic interactions within the particles and hydrodynamic shear flow. The electrostatic interaction is dominant until the critical shear rate ( $\dot{\gamma}_{crit}$ ), the  $\dot{\gamma}_{crit}$ , where the points exhibited pseudo-Newtonian behavior, located at the end of the plateau region. Beyond the  $\dot{\gamma}_{crit}$ , the shear stress increases gradually with increasing shear rate, giving a typical curve of Newtonian fluid behavior. The  $\dot{\gamma}_{crit}$  value increases gradually with the increase of external electric field

intensity. This indicates that the ER particle form more stable chain structure with the increase of external electric field intensity.

As a general model for an ER suspension, the Bingham model is expressed as follows:

$$\begin{aligned} \tau &= \tau_0 + \eta_0 \dot{\gamma}, \quad \tau \geq \tau_0 \\ \dot{\gamma} &= 0, \quad \tau < \tau_0 \end{aligned} \quad (4.1)$$

where  $\tau$  is the shear stress,  $\tau_0$  is the yield stress, which is related to an electric field,  $\dot{\gamma}$  is the shear rate, and  $\eta_0$  is the shear viscosity. But the flow curves of ER fluid could not be fitted with the simple Bingham model in the low shear rate region. To fit a whole shear rate region of ER fluids, Cho-Choi-Jhon (CCJ) model has been adopted. The CCJ model with six parameters is described by the equation as below:

$$\tau = \frac{\tau_0}{1 + (t_1 \dot{\gamma})^\alpha} + \eta_\infty \left[ 1 + \frac{1}{(t_2 \dot{\gamma})^\beta} \right] \dot{\gamma} \quad (4.2)$$

where  $\tau$  is the shear stress,  $\tau_0$  is the yield stress defined as the extrapolated stress at the low shear rate region,  $\dot{\gamma}$  is the shear rate,  $\eta_\infty$  is the viscosity at a high shear rate and is interpreted as the viscosity in the absence of an electric

field. The exponents  $\alpha$  and  $\beta$  ( $0 < \beta \leq 1$ , since  $d\tau/d\dot{\gamma} \geq 0$ ) are related to the decrease and increase in shear stress, respectively. The parameters  $t_1$  and  $t_2$  are time constants. Optimal fitting parameters were derived from flow curves of ER fluids using these two models and are listed in table 4.3.

The flow curve of ER fluids produced by different kinds of inorganic materials shows a similar Newtonian behavior in high shear rate region. This phenomenon could be due to insufficient time for formation of the chain-like structure against rapid shear deformation. In high shear rate region, the destruction of the chain-like structure occurs faster than the re-formation of the fiber-like structure with the increase of shear rates. In other words, the fibrous structures formed by polarization forces between ER particles were destroyed under the high shear force.

As shown in Table 4.3, yield stress value of S-MWNTs suspensions under external electric field of 2 kV/mm is about 7.5 Pa but that of T-MWNTs suspensions is 45.5 Pa. It indicates that interfacial polarization ability of the MWNTs coated by titania approximately 6 times higher than that of the MWNTs coated by silica. In case of T-MWNTs ER fluids, however, electrical short occurred under external electric field of 3 kV/mm. And it was impossible to measure rheological properties of 10 vol.% T-MWNTs suspensions under external electric field due to a large increase in electrical conductivity with increasing volume fraction.

Generally the electrical conductivity of a suspension depends on the particle

size, charge, and volume fraction. When metal oxide nanoparticles such as ZnO, TiO<sub>2</sub>, or Al<sub>2</sub>O<sub>3</sub> were dispersed in a fluid, these particles gain surface charge due to the protonation or deprotonation of a surface group such as a hydroxyl ligand (–OH) [171]. It indicates that the insulation resistance of T-MWNTs particles is lower than that of S-MWNTs particles.

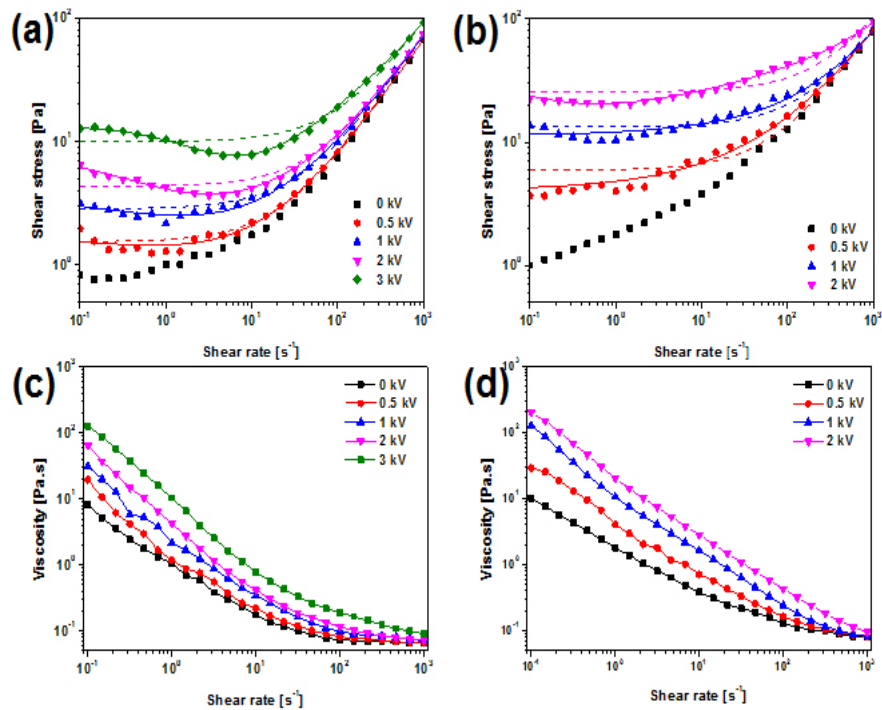


Figure 4.10 Shear stress (a)-(b) and shear viscosity (c)-(d) of function of shear rate for suspensions of the S-MWNTs and T-MWNTs with 20nm shell thickness under different electric field strength (5 vol.%, T = 25 °C).

Table 4.3 Optimal parameters in Bingham and CCJ model fitting to flow curves of S-MWNT-20(5) and T-MWNT-20(5) suspensions according to electric field strengths.

Model	Parameters	S-MWNT-20 (5 vol.%)				T-MWNT-20 (5 vol.%)		
		Electric field strength (kV/mm)						
		0.5	1	2	3	0.5	1	2
Bingham	$\tau_0$	1.543	2.848	4.317	9.897	5.926	13.3	25.63
	$\eta_0$	0.065	0.069	0.069	0.083	0.078	0.069	0.077
CCJ	$\tau_0$	2.032	4.449	7.583	13.02	7.083	15.3	45.56
	$\eta_0$	0.062	0.062	0.065	0.055	0.064	0.057	0.038
	$t_1$	1.002	2.6	3.717	0.526	4570	5.145	49.23
	$t_2$	0.07	0.023	0.015	0.002	0.008	0.003	6.1E-4
	$\alpha$	0.304	0.35	0.674	0.904	0.047	0.199	0.595
	$\beta$	0.671	0.612	0.795	0.562	0.705	0.819	0.822

The ER efficiency of the ER fluids with two different volume fractions of particles was determined using the following equation:

$$ER_{efficiency} = \frac{\eta_{E \neq 0} - \eta_{E=0}}{\eta_{E=0}} \quad (4.3)$$

where,  $\eta_{E \neq 0}$  and  $\eta_{E=0}$  are shear viscosity of ER fluids under external electric field and without external electric field, respectively. At the equal total particle volume fraction (5 vol.%), it is observed that the ER efficiency of T-MWNTs ER fluids is much higher than that of S-MWNTs ER fluids under the same external electric field of 2 kV/mm. And the ER efficiency of S-MWNTs fluids with 10 vol.% is much higher than that of S-MWNTs fluids with 5 vol.% at the same external electric field of 2 kV/mm. As shown in Figure 4.11, the ER efficiency of T-MWNTs ER fluids shows similar trends to that observed from S-MWNTs ER fluids. Interfacial polarization force between the dispersed dielectric particles increases faster with increasing particle concentration. The relationship between the external electric field (E) and the polarization force ( $F_p$ ) are given as the following equation:

$$F_p = \frac{6\epsilon r^6 E^2}{h^4} \quad (4.4)$$

where  $\varepsilon$  is the dielectric constant of the particles,  $r$  is the radius of particles, and  $h$  is the inter-particle distance. According to the equation (4.4), the polarization force ( $F_p$ ) increases with decreasing inter-particle distances and the degree of polarization is proportional to the external electric field.

Figure 4.12 shows the dynamic yield stress as a function of electric field strength for ER fluids with different volume fraction. This is defined to be the maximum stress that makes the solidified ER fluids flow. It is found that the yield stress of the T-MWNTs ER fluids with 5 vol.% is significantly higher than that of the S-MWNTs ER fluids with 5 vol.% under the same external electric field. And the yield stress of both S-MWNTs and T-MWNTs ER fluids increases with increasing volume fraction. The correlation between the dynamic yield stress and the external electric field is expressed as the power law relationship  $\tau_y \propto E^\alpha$  [26].

It is found that the exponent  $\alpha$  is different from the value of 2 predicted by dielectric polarization model and the value of 1.5 predicted by conduction model [70]. This can be attributed to the fact that the polarization model treats dielectric particles as ideal point dipoles and thus the electrostatic interaction between dielectric particles is treated as a dipole-dipole interaction only. In actual ER fluids, however, several factors such as particle concentration, shape, multi-dispersion, and nonlinear conductivity of oil, etc. influence the exponent  $\alpha$  [79, 172]. The exponent ( $\alpha=1.42$ ) of the T-MWNTs-5 ER fluids follows

conduction model but the exponent ( $\alpha=1.01$ ) of the S-MWNTs-5 ER fluids is smaller than 1.5 due to low dielectric loss tangent. This may be especially related to the different coating materials on MWNTs because other factors such as particle shape and concentration are all the same. The similar result is also observed in the ER fluids of inorganic SiO<sub>2</sub>-TOC and TiO<sub>2</sub>-TOC particles [173].

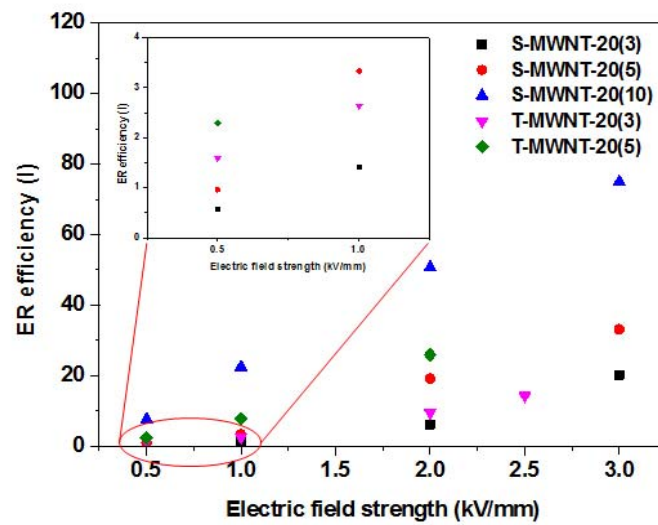


Figure 4.11 ER efficiency as a function of electric field strength for S-MWNT-20(3, 5, 10), and T-MWNT-20(3, 5) suspensions

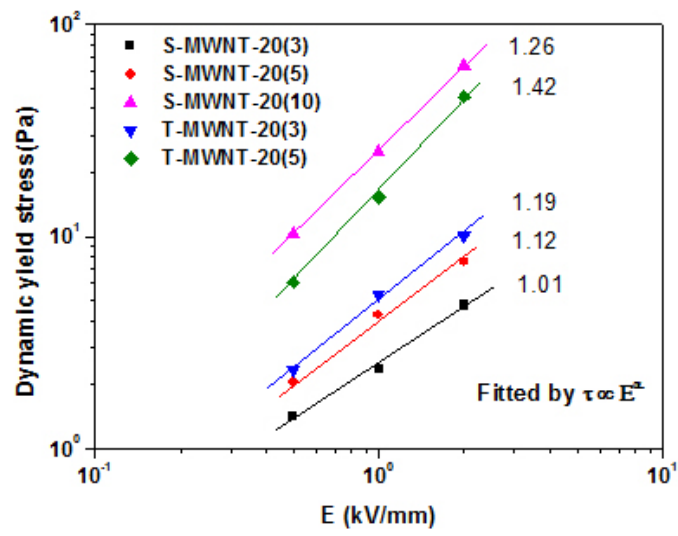


Figure 4.12 Dynamic yield stress as a function of electric field strength for S-MWNT-20(3, 5, 10), and T-MWNT-20(3, 5) suspensions.

Dynamic viscoelastic properties are also important to characterize the rheology of the ER fluids under external electric field. Figure 4.13 shows the frequency dependence of the storage modulus ( $G'$ ) and loss modulus ( $G''$ ) of S-MWNTs-5 and T-MWNTs-5 ER fluids at a strain of 0.1 % in the linear viscoelastic region. All ER fluids exhibit a solid-like behavior under external electric fields. Namely, the storage modulus ( $G'$ ) is substantially greater than the loss modulus ( $G''$ ) and both  $G'$  and  $G''$  remain at a near plateau in a frequency range from 0.1 to  $10^2$  Hz. At the same time, it is observed that the shear modulus increase with increasing external electric field strength. The storage modulus ( $G'$ ) of T-MWNTs-5 ER fluids was 3 times higher than that of the S-MWNTs-5 ER fluids under same external electric field (2 kV/mm). This indicates that the solidification or interfacial polarization ability of the T-MWNTs ER fluids is larger than that of the S-MWNTs ER fluids.

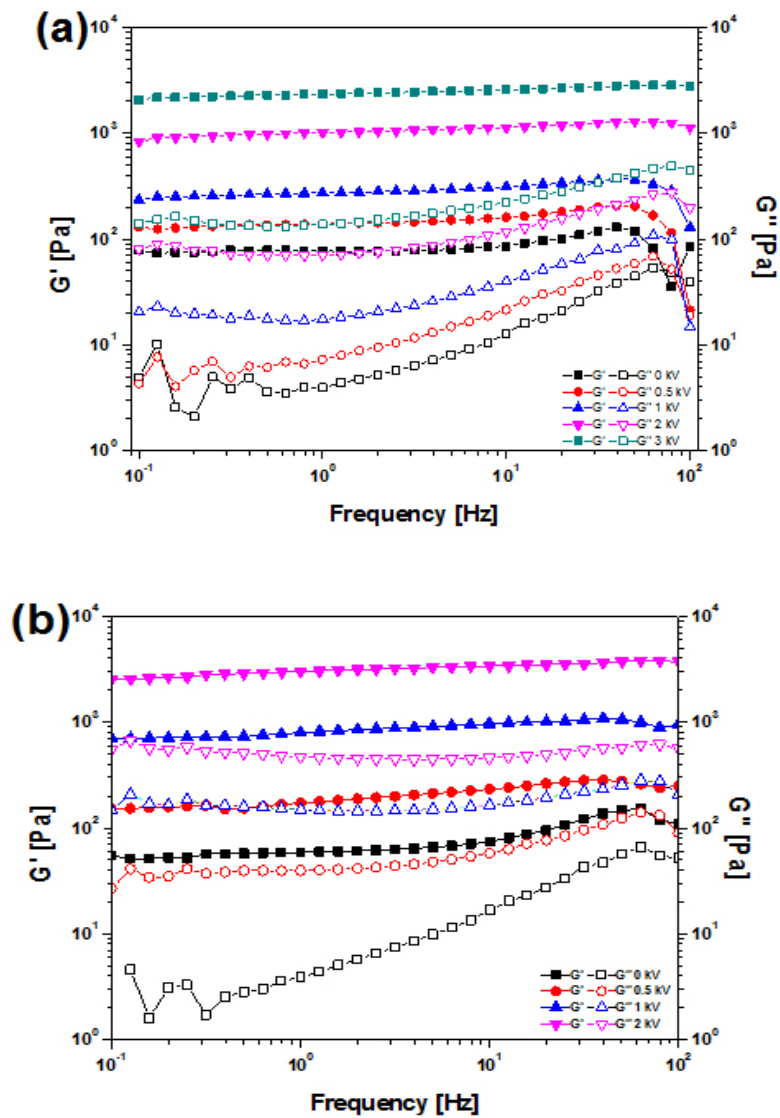


Figure 4.13 Storage modulus ( $G'$ , solid points) and loss modulus ( $G''$ , open points) as a function of frequency for (a) S-MWNT-20(5) suspensions and (b) T-MWNT-20(5) suspensions under different electric fields ( $T = 25$  °C).

Electro-rheometer studies are conducted to observe viscosity change and ER behavior of inorganic-coated MWNTs suspension with different shell thickness under the external electric field. It is known that most of the ER fluid acts as a Bingham plastic behavior under shear force. This Bingham plastic behavior is associated with the chain-like or column-like structures formed by electrostatic interactions between electrically charged particles. However, many papers adopt the modified equation such as the Cho–Choi–John equation (4.2) to understand the shear stress curve [15]. Optimal fitting parameters were derived from flow curves of S-MWNTs suspension with shell thickness of 10, 20 and 40 nm using Bingham and CCJ models and are listed in table 4.4.

Figure 4.14 shows the flow curves of the shear stress versus shear rate and viscosity versus shear rate for ER fluids containing silica-coated MWNTs with different shell thickness of 20 vol.% under external electric fields. ER fluids containing silica-coated MWNTs with different shell thickness show good ER properties within a wide range of shear rates. The shear stress and viscosity increase with the increase of the electric field strength. This strong interaction was caused by interfacial polarization between silica-coated MWNTs.

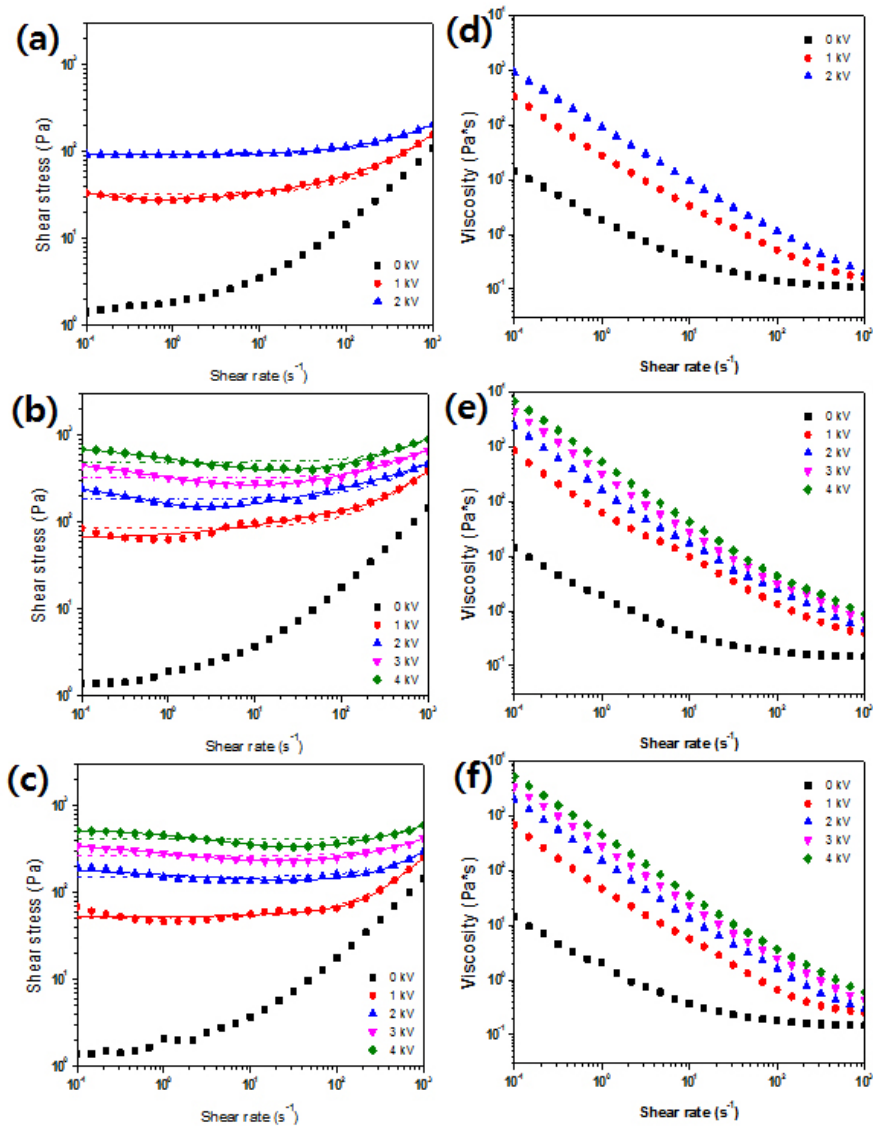


Figure 4.14 Steady flow curves of shear stress and shear viscosity as the function of shear rate for S-MWNTs suspension with shell thickness of 10 nm (a, d); 20 nm (b, e) and 40 nm (c, f) under external electric field ( $T = 25\text{ }^{\circ}\text{C}$ , 20 vol.%).

Table 4.4 Optimal parameters in Bingham and CCJ model fitting to flow curves of S-MWNTs suspension with shell thickness of 10, 20 and 40 nm according to electric field strengths.

Model	Parameters	S-MWNT-10(20)		S-MWNT-20(20)				S-MWNT-40(20)					
		Electric field strength (kV/mm)											
		1	2	1	2	3	4	1	2	3	4		
Bingham	$\tau_0$	32.6	94.4	84.0	186	322	4948	51.5	150	265	410		
	$\eta_0$	0.13	0.12	0.32	0.32	0.37	0.4	0.19	0.13	0.14	0.15		
CCJ	$\tau_0$	53.8	132	73	230	478	797	58	197	351	523		
	$\eta_\infty$	0.10	0.07	0.14	0.11	0.09	0.11	0.11	0.18	0.07	0.10		
	$t_1$	34	2.81	8E-3	2.5	2.22	0.71	6E-3	9.2	0.53	0.29		
	$t_2$	2E-3	6E-4	4E-4	2E-4	7E-5	5E-5	3E-4	2E-3	1E-4	1E-4		
	$\alpha$	0.81	0.17	1.69	0.94	0.46	0.44	1.29	0.23	0.41	0.65		
	$\beta$	0.89	0.82	0.54	0.81	0.71	0.64	0.21	0.98	0.75	0.81		

Figure 4.15 shows dynamic yield stress and current density of silica-coated MWNTs suspensions with shell thickness of 10, 20 and 40 nm under the external electric field. Dynamic yield stress value of silica-coated MWNTs suspensions with shell thickness of 10, 20 and 40 nm was about 131.9, 220.1 and 187.1 Pa, respectively, under external electric field of 2 kV/mm (figure 4.15 (a)). It indicates that interfacial polarization ability is enhanced with an increase of the silica coating thickness. However, in the case of the S-MWNTs suspension with a shell thickness of 40 nm, viscosity and yield stress values are slightly lower than the S-MWNTs suspension with a shell thickness of 20 nm. Consequently, enhanced ER performance is influenced by the dielectric properties as well as the electrical conductivity of nanoparticles.

Yin *et al.* [174] suggested that nano-particles with a conducting PANI core are difficult to maintain stable inter-particle interactions and the reorganization of chain-like ER structure due to a fast polarization rate. This result proves that there exist an optimum coating thickness to obtain the best balance between the polarization and the conductivity. As shown in the Figure 4.15 (b), the current density of S-MWNTs suspension with a shell thickness of 40 nm measured exclusively less than  $20 \mu\text{A}/\text{cm}^2$ . It is noteworthy that under a DC field, a conductivity mismatch between the two contiguous phases and the interfacial polarization of particles strongly influence ER behavior. As a result, the optimal conductivity mismatch between the two phases is an important factor in the ER effect under a DC field.

To discuss the effect of particle conductivity on ER fluid, furthermore, we prepared a pellet using the Automatic Hydraulic Press (US, Platen Carver 3894) to measure the DC conductivity of particles. DC resistances were measured using a Keithly 6517A Electrometer/High Resistance Meter with a Model 8009 Resistivity Test Fixture capable of measuring surface resistivity as high as  $10^{18}$  ohms/cm. As shown in Figure 4.16, the electrical conductivity of the S-10, S-20 and S-40 particle was  $7.9 \times 10^{-8}$ ,  $6.2 \times 10^{-11}$  and  $7.3 \times 10^{-12}$  S/cm, respectively. We confirmed that the electrical conductivity of particle decrease with an increase shell thickness of silica-coated MWNTs. Therefore, it is essential in the successful design of an ER material to understand the effects of structural and compositional factors that influence the conductivity mismatch of the ER suspension.

The relationship between the dynamic yield stress and the particle volume fraction under electric field strengths is shown in Figure 4.17. The dynamic yield stress values of S-MWNTs based ER fluids gradually increase with an increase of the particle volume fraction. This increment of the dynamic yield stress value with an increase of the particle volume fraction may be attributed to the enhanced inter-particle interactions.

According to equation (4.5), the polarization force ( $F_p$ ) is affected by the permittivity difference between the liquid and solid particles and the electric field strength. The interfacial polarization force between the dispersed dielectric particles will increase with an increase of the particle concentration. The

relationship between the external electric field ( $E$ ) and the polarization force ( $F_p$ ) are given as the following equation:

$$F_p = k\epsilon_m(2r)^2 f^2 E^2 S \quad (4.5)$$

where,  $F_p$  is the electrostatic force,  $k$  is a constant,  $f = (g - 1) / (g + 2)$  and  $g = \epsilon_p / \epsilon_m$ ,  $S$  is a factor related to the particle structure.

The dynamic yield stress value of S-MWNTs suspension with a shell thickness of 20 nm is about 900 Pa at 20 vol%, which is about 25 times the same material at 3 vol.%. The shear stress value of S-MWNTs suspension with a shell thickness of 20 nm is also 4 times higher than the S-MWNTs suspension with a shell thickness of 10 nm at the same volume fraction (10 vol%) under an applied electric field (4 kV/mm). This enhanced ER property is resulted from the chain-like structures formed by induced electrostatic interaction. As mentioned above, the polarizability and the electrical conductivity of chain-like structures are strongly affected by applied electric field strength. Thus, highly-connected structures in high electric field strength provide a sufficient electrostatic interaction, which counteracts the hydrodynamic force under shear flow.

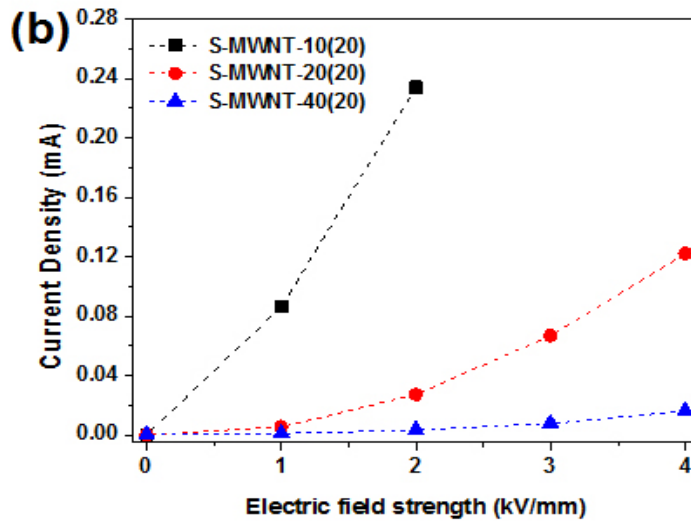
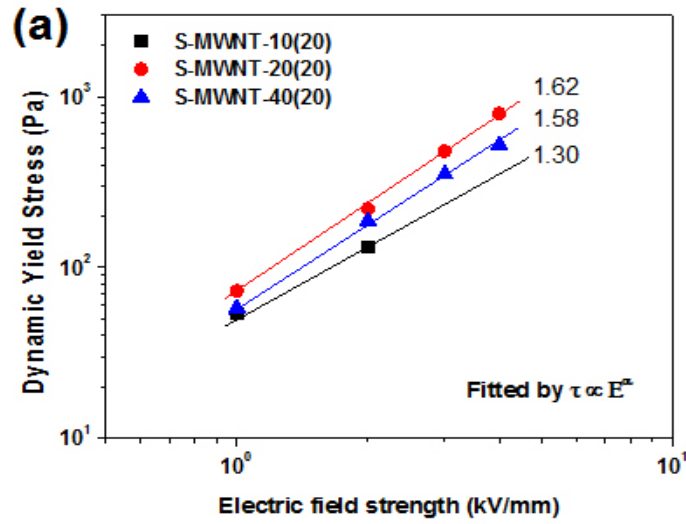


Figure 4.15 (a) Yield stress as a function of electric field strength for 20 vol.% S-MWNTs suspensions with different shell thickness of 10, 20 and 40 nm, (b) Current density of S-MWNTs suspensions with different shell thickness under electric fields

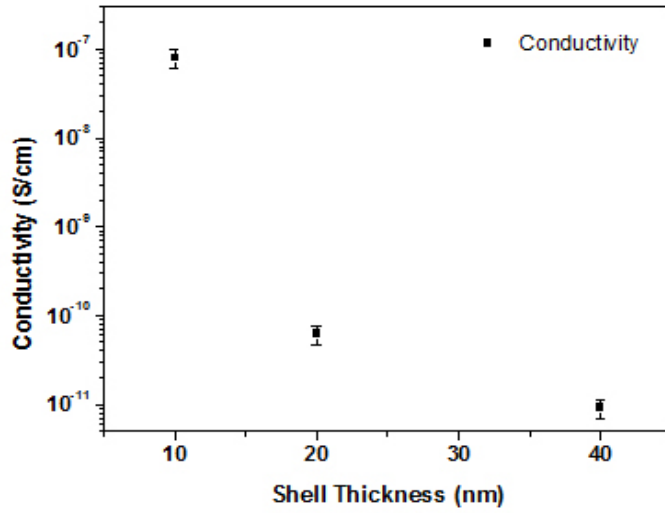


Figure 4.16 The electrical conductivity of S-MWNTs as shell thickness.

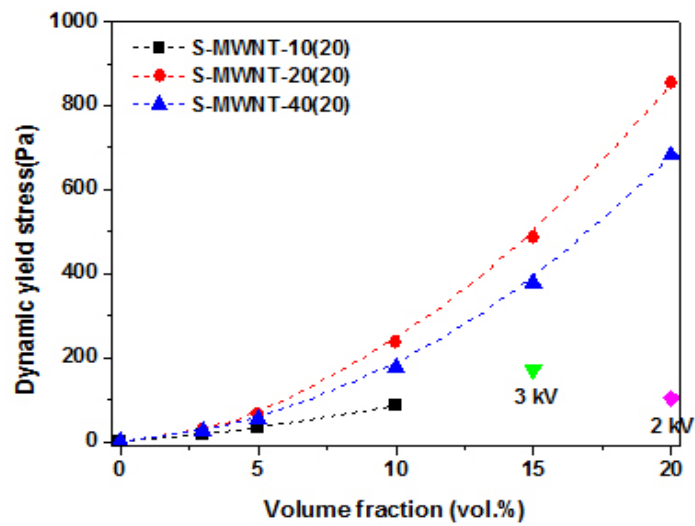


Figure 4.17 The shear stress of S-MWNTs suspensions with different shell thickness as a function of particle volume fraction ( $T = 25\text{ }^{\circ}\text{C}$ ,  $4\text{ kV/mm}$ ).

We prepared inorganic-coated MWNTs suspension with various core-shell structures to observe the effect of a coating sequence on ER fluid. In order to exclude the effect of the shell thickness on ER performance, shell thickness for silica-coated MWNTs and titania-coated MWNTs was adjusted to 40 nm and were named the S-MWNT-40 and T-MWNT-40, respectively. The inner- and outer-shell thicknesses of the ST- and TS-MWNTs were controlled at 20 nm and named the ST-MWNT-40 and TS-MWNT-40, respectively. Figure 4.18 shows the flow curves of the shear stress versus shear rate for ER fluids containing inorganic-coated MWNTs with different shell sequence of 20 vol.% under external electric fields. And optimal fitting parameters were derived from flow curves of T-MWNT-40(20), TS-MWNT-40(20), and ST-MWNT-40(20) suspensions using Bingham and CCJ models and are listed in table 4.5. ER fluids containing inorganic-coated MWNTs with different shell sequence show good ER properties within a wide range of shear rates. The shear stress and viscosity increase with the increase of the electric field strength. Figure 4.19 (a) shows the behavior of the dynamic yield stress of the various inorganic-coated MWNTs based ER fluids under external electric field. The yield stress value of the S-, T-, ST- and TS-MWNTs with a shell thickness 40 nm based ER fluids (20 vol.%) was 796, 3009, 933 and 2123 Pa under the 4 kV/mm, respectively. As we expected, the T-MWNT-40(20) suspension displays notable ER effects due to a high dielectric constant. And, the yield stress value of the ST-MWNT-40(20) based ER fluid is the next higher. It indicates that the feature of inorganic

material coated on the particle surface play a very important role on ER performance. The yield stress value of the TS-MWNT-40(20) suspension is higher than the S-MWNT-40(20) suspension. The surface properties of the particle play a very important role in ER fluids. However, in the case of the particles with core/shell structure, the surface properties of the particle can be changed by the properties of core materials. And we think that ER effect of TS-MWNT-40(20) suspension is better than that of S-MWNT-40(20) suspension because the transfer of electrons of the particles with nanofiber type could be caused by in the edge part as well as the permittivity of TS-MWNT-40(20) suspension is also higher than that of S-MWNT-40(20) suspension.

The correlation between the dynamic yield stress and the external electric field is expressed as the power law relationship  $\tau_y \propto E^\alpha$ . It is found that the exponent  $\alpha$  is slightly different from the value predicted by the dielectric polarization model. When compared to the exponent ( $\alpha=1.71$ ) of the T-40 based ER fluid, the exponent of the ER fluids with different shell sequence are slightly smaller. This may be related to the dielectric constant and electrical conductivity because other factors such as particle shape, size and concentration are the same.

As shown in Figure 4.19 (b), however, the current density value of the T-40 suspension is much higher than the other samples. And the current density value of the ST-40 based ER fluid is the next higher. T-40 suspension shows higher yield stress and current density, while S-40 suspension shows lower yield stress

and current density than the other samples. So we think that ST-40 suspension is the most appropriate ER fluid.

Figure 4.20 shows dynamic yield stress of inorganic-coated MWNTs suspensions with various shell sequence as a function of particle volume fraction. The dynamic yield stress values for all samples gradually increase with an increase of the particle volume fraction. As mentioned above, an interfacial polarization force has taken an influence on inter-particle distances and the degree of polarization. An increase of the polarization force will cause an enhanced ER performance. As shown in Figure 4.21, the electrical conductivity of the T-MWNT-40, TS-MWNT-40, and ST-MWNT-40 particle was  $1.2 \times 10^{-10}$ ,  $3.2 \times 10^{-11}$  and  $9.8 \times 10^{-12}$  S/cm, respectively. We confirmed that the electrical conductivity of particle depends on position of coating particle. It indicates that electrical properties of outermost layer are more influential than intrinsic carbon nanotube conductivity.

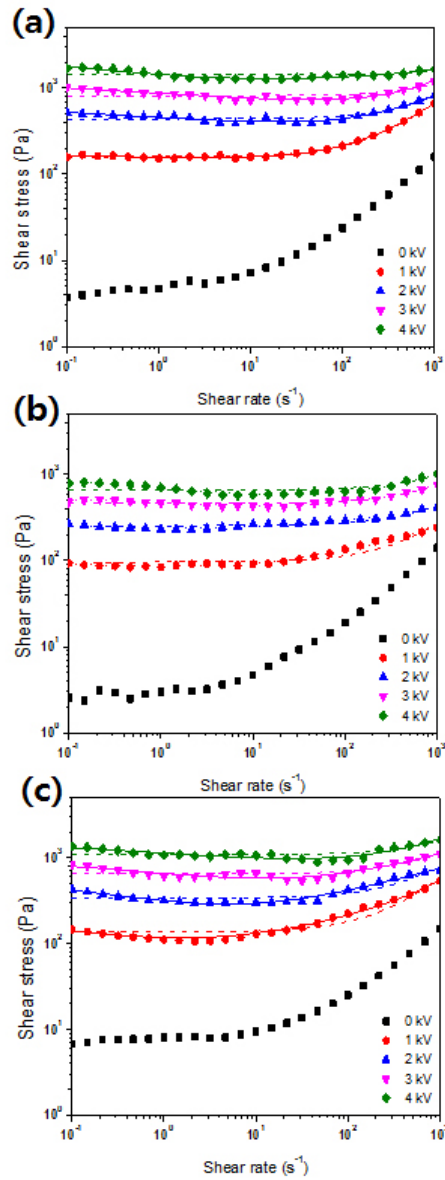


Figure 4.18 Steady flow curves of shear stress as the function of shear rate for (a) T-MWNT-40, (b) TS-MWNT-40, and (c) ST-MWNT-40 suspension under external electric field ( $T = 25\text{ }^{\circ}\text{C}$ , 20 vol.%).

Table 4.5 Optimal parameters in Bingham and CCJ model fitting to flow curves of T-MWNT-40(20), TS-MWNT-40(20), and ST-MWNT-40(5) suspensions according to electric field strengths.

Model	Parameters	T-MWNT-40(20)				TS-MWNT-40(20)			
		Electric field strength (kV/mm)							
		1	2	3	4	1	2	3	4
Bingham	$\tau_0$	159.2	439.7	817.7	1426	96.18	254.1	459.3	660.3
	$\eta_0$	0.52	0.38	0.307	0.181	0.176	0.19	0.306	0.336
CCJ	$\tau_0$	279.4	880.3	1857	3009	101.5	295.9	570.1	933
	$\eta_0$	0.221	0.144	0.456	0.158	0.027	0.063	0.096	0.242
	$t_1$	0.006	0.085	1.742	18.18	2.036	12.48	0.178	1.461
	$t_2$	2E-4	9E-5	0.002	9E-5	6E-5	2E-04	9E-5	3E-4
	$\alpha$	0.046	0.206	0.145	0.39	0.356	0.396	0.347	0.302
	$\beta$	0.213	0.497	0.64	0.92	0.74	0.9	0.744	0.769

Model	Parameters	ST-MWNT-40(20)			
		Electric field strength (kV/mm)			
		1	2	3	4
Bingham	$\tau_0$	135	338.1	644.7	1080
	$\eta_0$	0.451	0.479	0.5	0.528
CCJ	$\tau_0$	207.9	615.2	1297	2124
	$\eta_0$	0.21	0.0175	0.013	0.268
	$t_1$	22.88	2.49	1	0.153
	$t_2$	6E-4	68E-6	1.4E-6	1.2E-4
	$\alpha$	0.363	0.503	0.312	0.248
	$\beta$	0.741	0.724	0.667	0.623

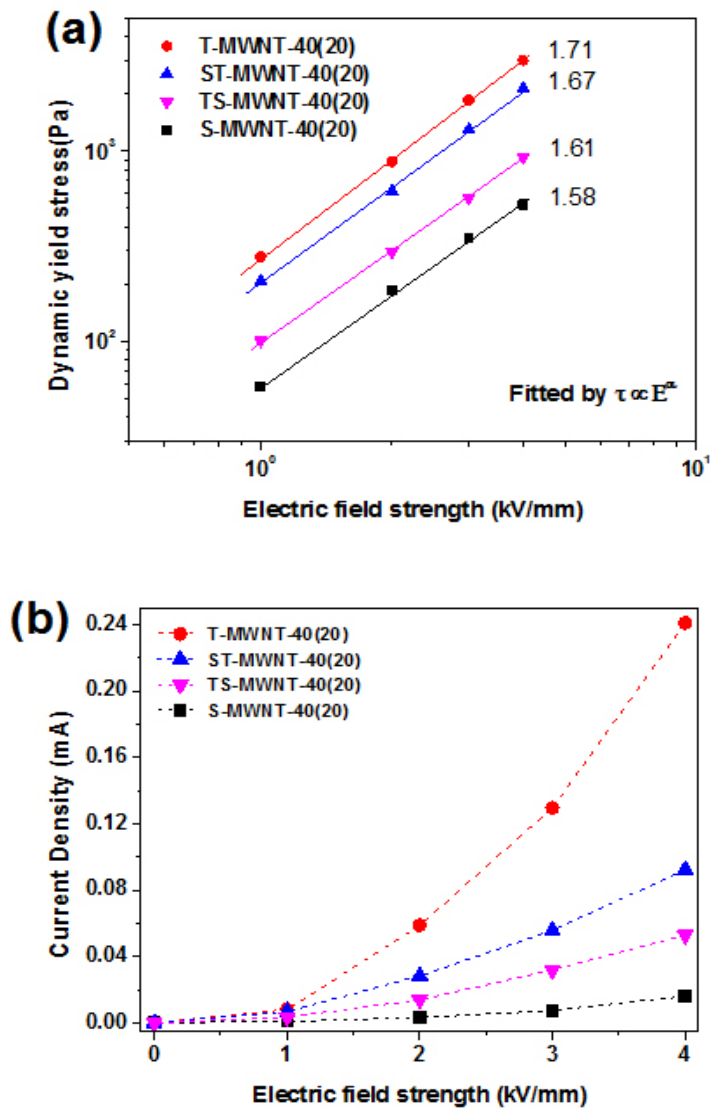


Figure 4.19 (a) Yield stress as a function of electric field strength for inorganic-coated MWNT suspensions with different shell sequences, (b) current density of inorganic-coated MWNT suspensions with different shell sequences under electric fields.

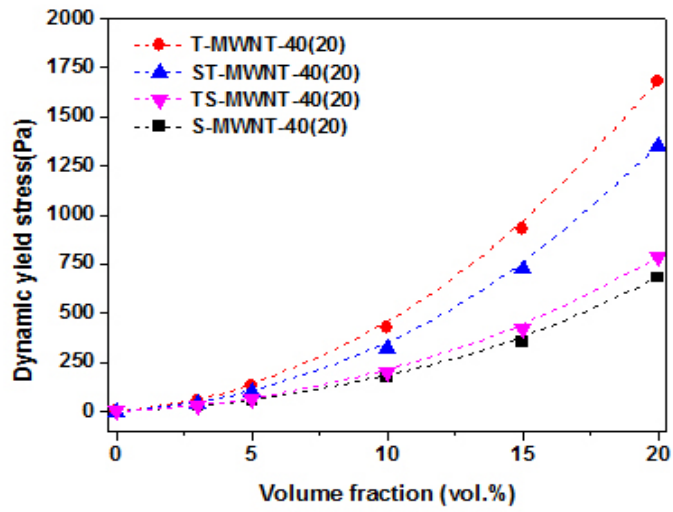


Figure 4.20 Yield stress of inorganic-coated MWNTs suspensions with various shell sequence as a function of particle volume fraction ( $T = 25\text{ }^{\circ}\text{C}$ ,  $4\text{ kV/mm}$ ).

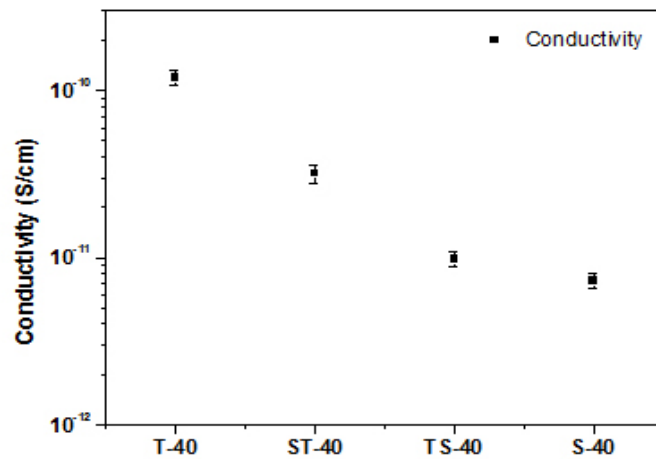
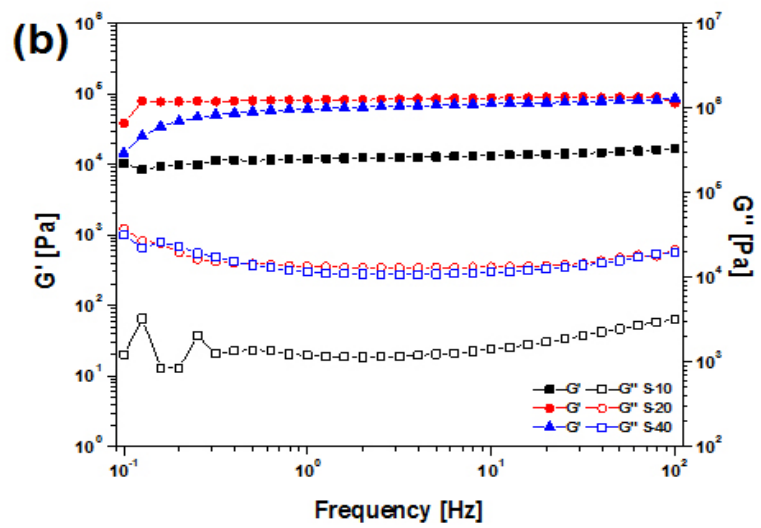
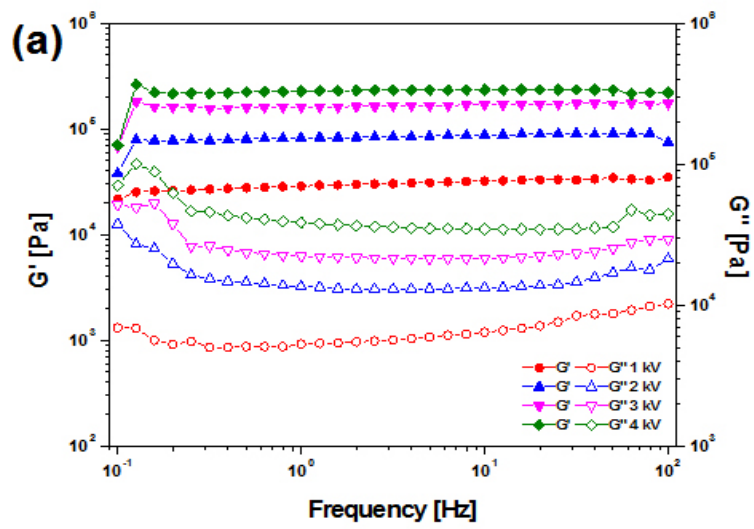


Figure 4.21 The electrical conductivity of inorganic-coated MWNTs with various shell sequence.

Dynamic viscoelastic properties are also important to characterize the rheology of the ER fluids under an external electric field. Figure 4.22 shows the frequency dependence of the storage modulus ( $G'$ ) and loss modulus ( $G''$ ) of various inorganic-coated MWNTs ER fluids at a strain of 0.1% in the linear viscoelastic region. The storage modulus ( $G'$ ) is substantially greater than the loss modulus ( $G''$ ), and  $G'$  and  $G''$  remain at a near plateau in a frequency range from 0.1 to  $10^2$  Hz (Figure. 4.22(a)). At the same time, we observed that the shear modulus increases with an increase in the external electric field strength.

All ER fluids exhibit a solid-like behavior under external electric fields. The storage modulus ( $G'$ ) of S-MWNTs ER fluids with a shell thickness of 20 nm was 6 times higher than that of the S-MWNTs ER fluids with shell thickness of 10 nm under external electric field of 2 kV/mm (figure 4.22 (b)). This indicates that the solidification or interfacial polarization ability of the S-MWNTs ER fluids with a shell thickness of 20 nm is larger than that of the S-MWNTs ER fluids with a shell thickness of 10 nm. Figure 4.22 (c) shows the storage modulus ( $G'$ ) and loss modulus ( $G''$ ) of inorganic-coated MWNTs ER fluids with different shell sequence under an external electric field of 4 kV/mm. The storage modulus of T-40 ER fluid was 10 times higher than that of S-40 ER fluid under an external electric field.



(continued)

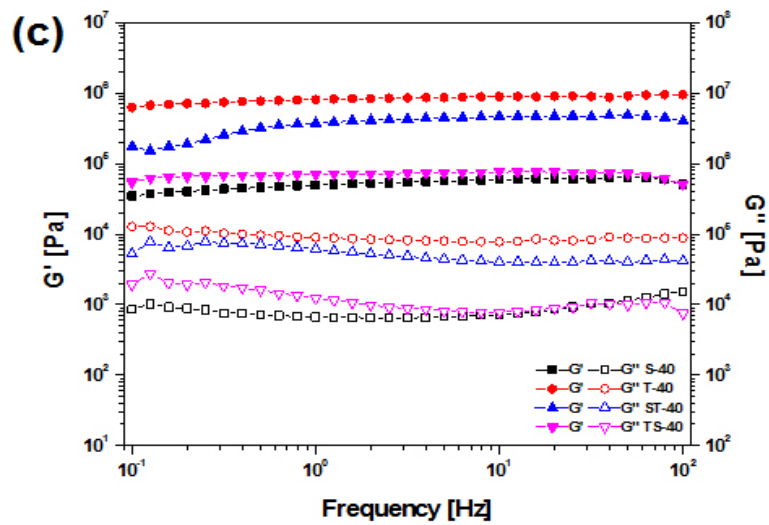


Figure 4.22 Storage modulus ( $G'$ , solid points) and loss modulus ( $G''$ , open points) as a function of frequency for (a) S-MWNT-20(20) suspension under different electric fields and (b) S-MWNTs suspension with different shell thickness under electric field of 2 kV/mm (c) inorganic-coated MWNTs with various shell sequence under electric field of 4 kV/mm ( $T = 25$  °C).

### 4.1.3 Dielectrical properties

The polarization of the dielectric particles and the dielectric properties of the suspension are main factors in the ER response. And the total polarization is the sum of several contributions such as electron, atomic, Debye and interfacial polarization. In particular, interfacial polarization of dispersed particles in medium plays an important role on the ER effect and the dielectric properties were dominant in ER effects. Figure 4.23 shows the dielectric spectra of ER fluids containing S-MWNTs-5, S-MWNTs-10, T-MWNTs-3 and T-MWNTs-5 particles. The dashed lines in the figure 4.23 are generated from the Cole-Cole equation which is useful tool to reveal the relationship between permittivity and ER effects of the ER fluids. The Cole-Cole equation is described by the equation. (4.6).

$$\varepsilon^* = \varepsilon' + i\varepsilon'' = \varepsilon'_\infty + \frac{\varepsilon'_0 - \varepsilon'_\infty}{1 + (i\omega\tau)^{1-\alpha}} \quad (4.6)$$

where,  $\varepsilon'_0$  and  $\varepsilon'_\infty$  are the static and infinite frequency dielectric constant,  $\omega$  is an angle frequencies,  $\tau$  is a dielectric relaxation time denoted by

$$\tau = \frac{1}{2\pi f_{\max}} \quad (\text{where } f_{\max} \text{ is the relaxation frequency defined by a local}$$

maximum of the dielectric loss factor  $\varepsilon''$ ),  $\alpha$  is the scattering degree of relaxation time and  $\Delta\varepsilon' (= \varepsilon'_0 - \varepsilon'_\infty)$  shows the difference between the dielectric constant at 0 and infinite frequency. Among the various parameters,  $\Delta\varepsilon'$  and  $\tau$  respectively represent the magnitude and the rate of the interfacial polarization of ER fluids. These parameters are considered to be important dielectric parameters in determining the ER effects.

The  $\Delta\varepsilon'$  values of S-MWNT-20(5), S-MWNT-20(10), T-MWNT-20(3) and T-MWNT-20(5) were 0.56, 0.89, 0.96 and 2.37, respectively. The  $\Delta\varepsilon'$  values of T-MWNTs ER fluids were higher than that of S-MWNTs ER fluids in the same volume fraction. And the  $\Delta\varepsilon'$  values of suspension increase with increasing volume fraction. This indicates that the magnitude of the interfacial polarization of the T-MWNTs ER fluids is higher than that of S-MWNTs ER fluids. The dielectric parameters such as  $\Delta\varepsilon'$ , dielectric relaxation time ( $\tau$ ) and scattering degree of relaxation time ( $\alpha$ ) of S-MWNT-20(5), S-MWNT-20(10), T-MWNT-20(3) and T-MWNT-20(5) suspensions obtained by Cole-Cole equation are summarized in table 4.6.

However, the  $\tau$  value ( $1.36 \times 10^{-3}$  s) of the T-MWNTs-5 ER fluids was higher than that ( $1.70 \times 10^{-4}$  s) of the S-MWNT-20(5) ER fluids, which signifies that the polarization rate of the latter is slightly faster than that of former. The dielectric response might be mainly attributed to the difference of the dielectric constant of coating layer on the MWNTs. This is because factors such as particle

morphology, shell thickness, core material and the surrounding medium in two different nanoparticles suspension are similar for both suspensions. Therefore, the T-MWNTs ER fluids show a greater polarization response compared to the S-MWNTs ER fluids. Namely, the T-MWNTs ER fluids easily exhibit stronger solid-like behavior, such as a higher static yield stress and storage modulus, compared to ER properties of the S-MWNTs ER fluids.

As shown in Figure 4.23 (b), all the samples show a dielectric loss peak within  $10^2$ - $10^5$  Hz. Generally, when the dielectric loss peak was located in  $10^2$ - $10^5$  Hz, the interfacial polarization was known appropriate in order to achieve enhanced ER effects. When the polarization rate is too fast or too slow, the ER fluids are difficult to maintain stable inter-particle interactions under shear deformation. Usually, an increase in the volume fraction will lead to increased inter-particle contacts and subsequently the development of dc conductivity losses and dipole polarization losses within the suspension. So the results show variation in dielectric constant and relaxation time with change in volume fraction. It has been proved that the dielectric factors of the ER fluids can be controlled by the coating materials on MWNTs and the difference of particle volume fraction.

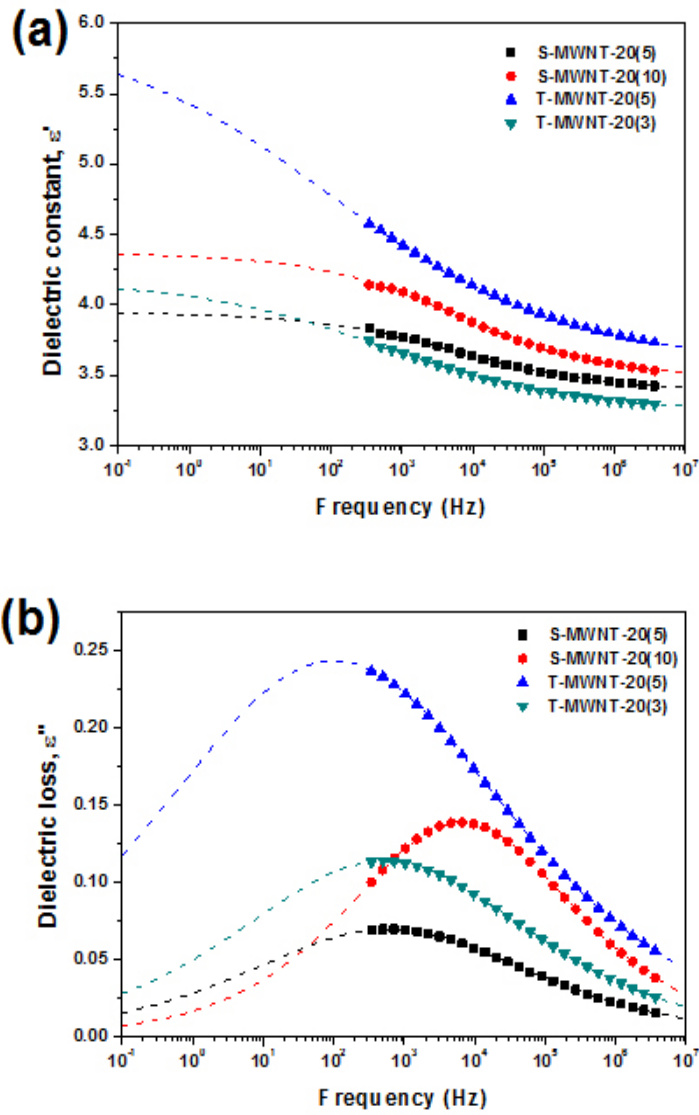


Figure 4.23 Dielectric spectra of suspensions containing S-MWNT-20(5), S-MWNT-20(10), T-MWNT-20(3) and T-MWNT-20(5) nanoparticles ( $T = 25 \text{ }^\circ\text{C}$ ). Fitting lines are generated from the Cole-Cole Equation (4.6).

Table 4.6 Dielectric parameters of S-MWNT-20(5), S-MWNT-20(10), T-MWNT-20(3) and T-MWNT-20(5) suspensions obtained from the Cole-Cole fitting.

Sample	$\varepsilon'_0$	$\varepsilon'_\infty$	$\Delta\varepsilon' = \varepsilon'_0 - \varepsilon'_\infty$	$f_{\max}$	$\alpha$
S-MWNT-20(5)	3.95	3.39	0.56	$9.34 \times 10^2$	0.69
S-MWNT-20(10)	4.37	3.48	0.89	$7.26 \times 10^3$	0.61
T-MWNT-20(3)	4.17	3.24	0.96	$6.94 \times 10^2$	0.69
T-MWNT-20(5)	5.76	3.59	2.17	$1.17 \times 10^2$	0.74

Figure 4.24 shows the dielectric spectra of inorganic-coated MWNTs suspension with various shell sequence. The dielectric parameters of inorganic-coated MWNTs suspensions are summarized in table 4.7. The  $\Delta\varepsilon'$  values of S-40, T-40, ST-40 and TS-40 suspension with different shell sequence were 1.89, 3.5, 3.56, and 1.91 in the same volume fraction (5 vol%), respectively. The  $\Delta\varepsilon'$  value of ST-40 suspension was the highest compared to that of other particle suspension with different shell sequence. Thus the magnitude of the interfacial polarization of the ST-40 suspension is higher than that of particle suspension with different sequence. The  $\tau$  value of  $5.57 \times 10^{-5}$  s for the T-40 based ER fluids was higher than the  $\tau$  value of  $4.45 \times 10^{-5}$  s for the ST-40 based ER fluids, which signifies that the relaxation of the latter is faster than that of former. The dielectric relaxation time of the T-40 based ER fluids is similar to the ST-40 and TS-40 based ER fluids.

The ER fluid including MWNTs coated by titania on the outermost layer easily exhibited strong solid-like behavior such as a higher dynamic yield stress and viscosity, compared to ER properties of the MWNTs ER fluid coated by silica on the outermost layer. Therefore, the sequence and the dielectric constant of coating material on a particle surface play an important role in the dielectric response. And all the samples show a dielectric loss peak within  $10^2$ - $10^5$  Hz. The results of our study provide a new mechanism to find the influential factors on ER activity through tuning the dielectric permittivity and electrical conductivity of nanoparticles.

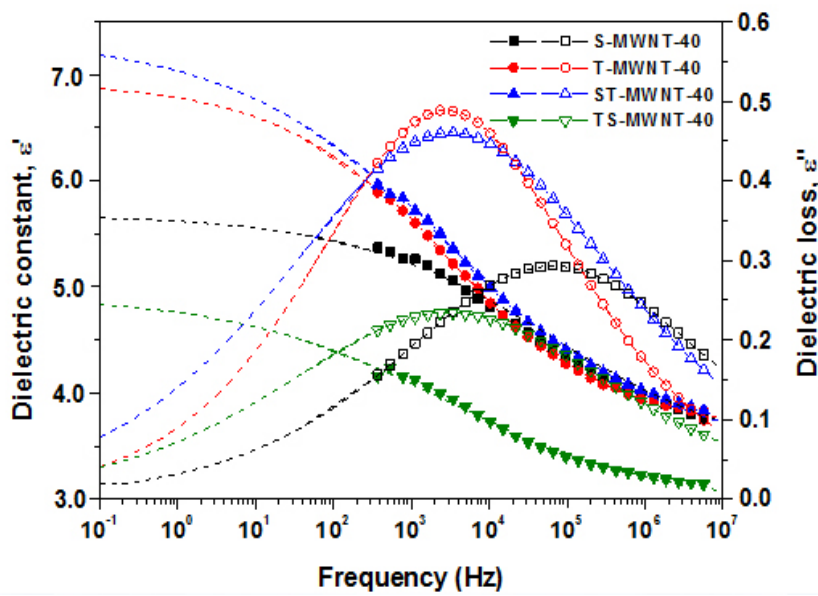


Figure 4.24 Dielectric spectra of suspensions containing S-MWNT-40, T-MWNT-40, ST-MWNT-40 and TS-MWNT-40 (T = 25 °C, 5 vol.%). Fitting lines are generated from the Cole-Cole Equation (4.6).

Table 4.7 Dielectric parameters of S-MWNT-40, T-MWNT-40, ST-MWNT-40 and TS-MWNT-40 suspensions from the Cole-Cole fitting.

Sample	$\epsilon'_{0}$	$\epsilon'_{\infty}$	$\Delta\epsilon' = \epsilon'_{0} - \epsilon'_{\infty}$	$f_{\max}$	$\alpha$
S-40	5.63	3.64	1.89	$7.85 \times 10^4$	0.68
T-40	6.95	3.45	3.5	$2.86 \times 10^3$	0.63
ST-40	7.12	3.59	3.53	$3.58 \times 10^3$	0.70
TS-40	4.86	2.98	1.91	$3.93 \times 10^3$	0.70

#### 4.1.4 Temperature and sedimentation effects

It is very important to investigate the dispersion stability and temperature dependence for ER applications. Figure 4.25 shows the temperature dependence of shear stress (2 kV/mm) of the S-MWNTs and T-MWNTs suspensions. It is found that the both S-MWNTs and T-MWNTs suspensions maintain a very stable shear stress value in the wide temperature range (25 ~80 °C), indicating that the both S-MWNTs and T-MWNTs suspensions possess good temperature stability.

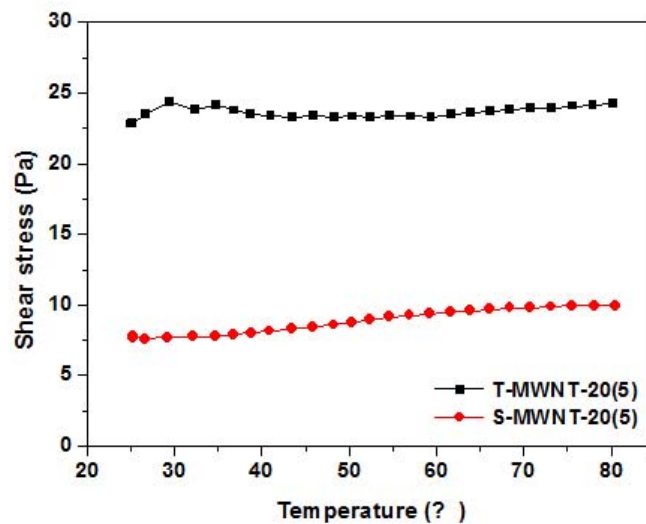


Figure 4.25 Temperature dependence of shear stress (2 kV/mm, shear rate = 10.0 s<sup>-1</sup>) of S-MWNT-20 and T-MWNT-20 suspension (T = 25 °C, 5 vol.%).

Figure 4. 26 shows the temperature dependence of dielectric property of T-MWNTs with 20 nm shell thickness. The dielectric parameters of T-MWNT-20(5) suspensions as temperature changes are summarized in table 4.8. As temperature increases, the dielectric constant slightly increases and the loss peak shifts towards high frequency. It indicates that the polarizability of T-MWNTs nanoparticles become slightly stronger and polarization rate become faster with temperature increase. According to the proposed mechanism [96], as dielectric loss peak shifts towards high frequency within  $10^2$ - $10^5$  Hz and the larger dielectric constant is applied, higher ER activity is achieved. Therefore, the thermal-enhanced polarization of T-MWNTs may be responsible for the increase of its ER efficiency.

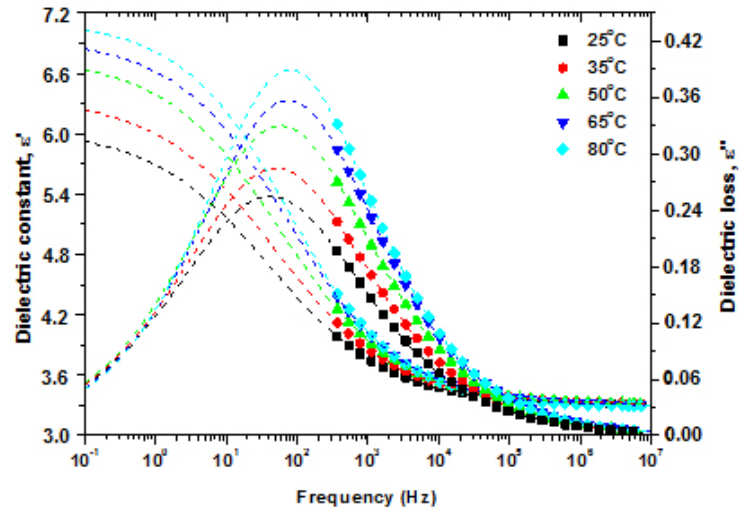


Figure 4.26 Temperature dependence of dielectric property of ER fluid containing T-MWNT-20 (5 vol.%). Fitting lines are generated from the Cole-Cole equation (4.6).

Table 4.8 Dielectric parameters of T-MWNT-20(5) suspensions as temperature changes obtained from the Cole-Cole fitting.

Sample	$\varepsilon'_0$	$\varepsilon'_\infty$	$\Delta\varepsilon' = \varepsilon'_0 - \varepsilon'_\infty$	$\tau$	$\alpha$
25 °C	5.94	3.32	2.62	$3.25 \times 10^{-4}$	0.66
35 °C	6.29	3.31	2.98	$3.06 \times 10^{-4}$	0.63
50 °C	6.64	3.32	3.32	$2.53 \times 10^{-4}$	0.59
65 °C	6.89	3.32	3.57	$1.99 \times 10^{-4}$	0.55
80 °C	7.11	3.29	3.82	$1.77 \times 10^{-4}$	0.51

Figure 4.27 shows the time dependence of sedimentation ratio of S-MWNTs and T-MWNTs suspensions (5 vol.%). The sedimentation is defined as  $R = b/(a + b)$  (%),  $a$  is the height of silicone oil separated from the ER fluid,  $b$  is the height of the ER fluid which is not separated. The greater the sedimentation, the anti-sedimentation property is better. Both the S-MWNTs and T-MWNTs suspensions show good dispersion stability due to the one-dimensional and hollow nanostructure. It is found that the S-MWNTs suspensions tend to settle more slowly compared to the T-MWNTs suspensions. After 10 days, a sedimentation of S-MWNTs is 95.8%, which is slightly higher than that (92.6%) of T-MWNTs suspensions. This is attributed to density difference of two different coating materials.

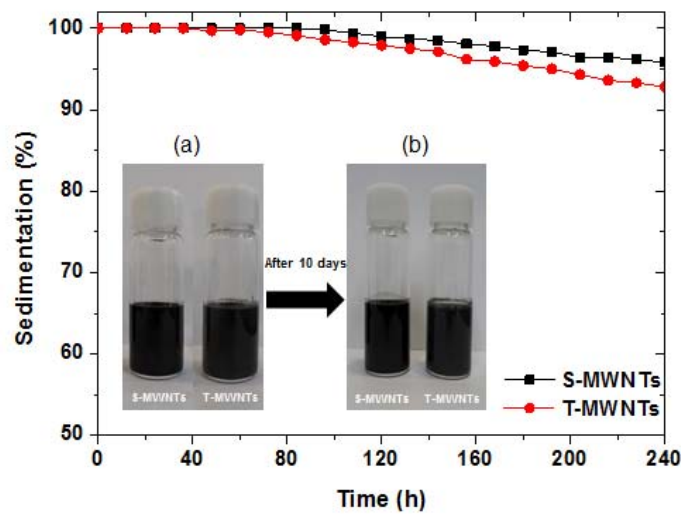


Figure 4.27 Sedimentation as a function of time for S-MWNT-20(5) and T-MWNT-20(5) suspensions ( $T = 25$  °C, 5 vol.%).

Figure 4.28 shows the time dependence of sedimentation of various core/shell structure nanotube suspensions (5 vol.%). All samples show good dispersion stability due to one dimensional and nanotube structure with the high aspect ratio. For the S-MWNTs suspension, the increment of shell thickness had negative effect on sedimentation. For inorganic-coated MWNTs suspension with different shell sequence, after 10 days, a sedimentation (88.2%) of S-MWNT-40 suspension is higher than that (81.5%) of T-MWNTs-40 suspension. It is found that the S-MWNTs suspensions tend to settle more slowly compared to the T-MWNTs suspensions. This is attributed to density difference of two different coating materials.

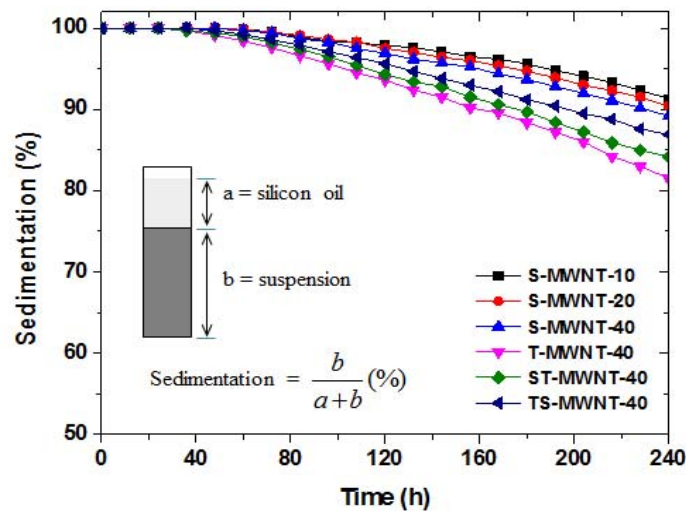


Figure 4.28 Sedimentation as a function of time for suspensions including inorganic-coated MWNTs with various core/shell structures (T = 25 °C, 5 vol.%).

#### 4.1.5 Summary

We have developed an easy route to synthesize core/shell nanotube structure MWNTs coated by amorphous silica or/and titania using a sol-gel process at room temperature. Core/shell structured nanoparticles were characterized by TEM, XRD, FT-IR and EDX spectroscopy. And the S-MWNTs and T-MWNTs ER fluids possessed wide range ER performance including high ER efficiency and high shear stress. It has been found that the T-MWNTs ER fluids showed a stronger ER effect compared to the S-MWNTs ER fluids at the same particle volume fraction. It has been confirmed that the dielectric performance including high permittivity and low dielectric loss of the T-MWNTs ER fluids has much higher than that of the S-MWNTs ER fluids at the same particle volume fraction. It has been found that the high permittivity is mainly due to interfacial polarization. The permittivity of the MWNTs based ER fluids can be controlled by the coating materials on MWNTs as well as volume fraction of ER particles, which provides a new route to tuning the permittivity and electrical conductivity of the MWNTs for the ER fluids development.

The S-MWNTs suspension with different shell thickness and inorganic-coated MWNTs suspension with different shell sequence also possessed wide range ER performance including high ER efficiency and high yield stress. We found that the ER effect of the S-MWNTs suspension increases with an increase

of the shell thickness. However, the S-MWNTs suspension with a shell thickness of 20 nm showed a stronger ER effect than S-MWNTs with different shell thickness of 10 and 40 nm.

We suggest that ER behavior is influenced by the dielectric properties and the electrical conductivity of nanoparticles. In the case of inorganic-coated MWNTs with different sequence, the ER effect and dielectric performance of the T-MWNTs ER fluids appeared much higher than the S-MWNTs ER fluids at the same particle volume fraction. However, the high current density of T-MWNTs could be restricted in the application of ER fluids because the high current density of ER fluids can cause an electrical short under the low electric field. Therefore, we believe that the ST-MWNTs ER fluid has high potential in the application of ER fluids due to high ER performance, low current density and high dispersion stability. The permittivity of the MWNTs based ER fluids can be controlled by the coating materials on MWNTs. The results of our study can provide a new mechanism to find influential factors on ER activity through tuning the dielectric permittivity and electrical conductivity of nanoparticle suspensions.

## 4.2. Titania-coated graphene sheets

### 4.2.1. Synthesis and characterization

HR-TEM and EDS analysis were used to identify the graphene oxide sheets and titania-coated graphene sheets produced in this study. The TEM image given in Figure 4.29 (a) shows that the graphene oxide sheets was 1 layer thick, and the electron diffraction pattern inserted in the same Figure 4.29 (a) shows the typical six-fold symmetry of graphene. As shown in Figure 4.29 (b), the titania-coated graphene sheets were analyzed with elemental mapping by energy dispersive spectrometry (EDS). The titania-coated graphene was enriched with titanium (Ti) and oxygen (O), indicating a uniform distribution of the TiO<sub>2</sub> nanoparticles throughout the whole graphene oxide sheet. The EDS analysis also indicated the presence of C (5.52%), O (27.21%), and Ti (67.27%), which proved that the TiO<sub>2</sub> nanoparticles were successfully coated on the graphene oxide sheets. It is possible that the TiO<sub>2</sub> coated on the graphene sheet could result in a relatively lower intensity of carbon content compared to the higher intensity of titanium content.

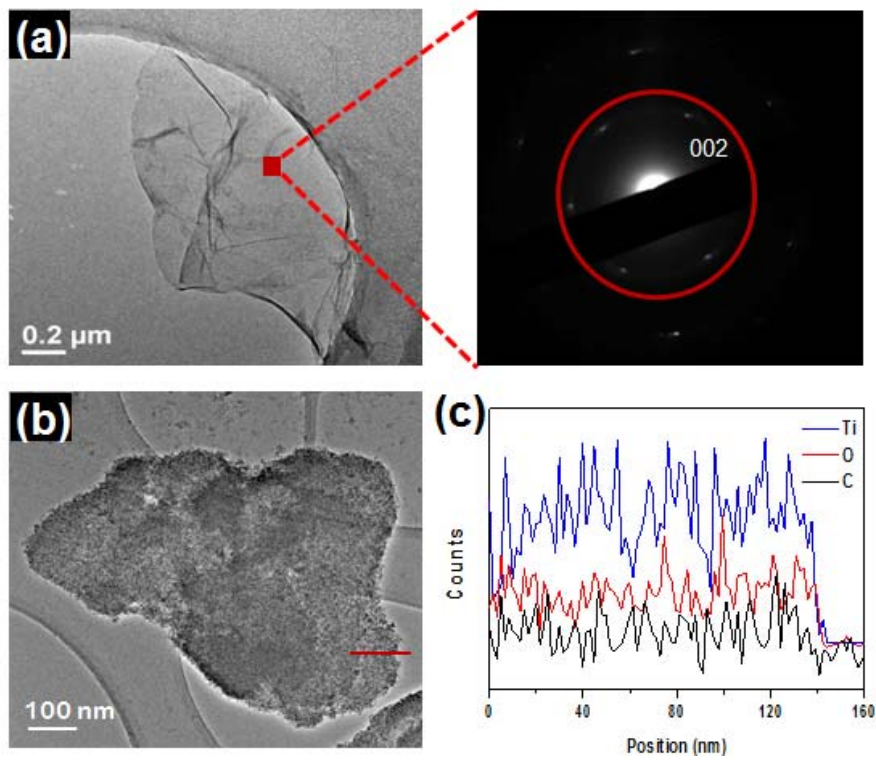


Figure 4.29 (a) TEM image of GO sheets and EDX pattern of the boxed area in (a), (b) TEM image of TCGSs and (c) EDS mapping of titanium (Ti), oxygen (O) and carbon (C), by EDS analysis on the selected area of the TCGSs.

Figure 4.30 shows the FT-IR spectra of GO sheets and TCGSs. For the GO sheets, the peak at  $3426\text{ cm}^{-1}$  was attributed to deformation of the -OH bond of the GO sheets. The peaks at  $1045$  and  $1720\text{ cm}^{-1}$  were also associated with the stretching of the C-O and C=O bond by carboxyl groups, respectively. The stretching vibration of the C=C was observed as a band at  $1627\text{ cm}^{-1}$  by GO sheet main chain. After the sol-gel reaction, the characteristic peaks of titania were observed, which indicates that the titania were synthesized on the GO sheet. The peak at between  $500$  and  $800\text{ cm}^{-1}$  is attributed to Ti-O-Ti bending vibration, while the carbonyl group band at  $1045$  and  $1720\text{ cm}^{-1}$  disappeared. This evidence proved that the carbonyl groups were changed to Ti-O-C bonds.

The GO sheets and TCGSs were characterized by high-resolution X-ray diffraction (HR-XRD) to observe the structural change of the particles. The interlayer distance can be calculated via the relationship between lattice intervals and the angle of reflection according to Bragg's law ( $n\lambda = 2d \sin \theta$ ). As shown in figure 4.31, the  $2\theta$  peak of GO sheets was at  $10.27^\circ$ , indicating that the graphite was fully exfoliated into graphene oxide sheets with an interlayer distance of  $0.89\text{ nm}$ . The TCGSs exhibited very weak XRD peaks corresponding to the (101), (004), (200), (211), (204), (200), and (215) planes for the anatase structure of  $\text{TiO}_2$  nanoparticle. It indicates that most  $\text{TiO}_2$  grown on GO sheets is in an amorphous phase.

As shown in figure 4.32, the surface chemistry of the TCGSs was investigated using the X-ray photoelectron spectrum (XPS). Binding energy,

FWHM, and peak area percentage of TCGSs, as determined after curve fitting of the XPS high resolution spectra are listed in table 4.9. The TCGSs contains three elements, C, O and Ti at 285, 530 and 457 eV in the XPS survey spectrum in figure 4.32(a), respectively. As shown in figure 4.32(b), the C 1s core level spectrum was deconvoluted into different four peaks. The peak at 284.4 eV is a signal of carbon element originated from the graphitic sp<sup>2</sup> carbon atoms. The peaks at 286.5, 288.6 and 290.3 eV are assigned to C–O bonds, carbonyls (C=O) bonds and carboxylates (O–C=O) bonds, respectively. These functional groups in the GO sheets undergo an esterification reaction with -OH groups of the Ti precursor and form covalent bonds of C–O–Ti or O–C–O–Ti. The corresponding O 1s region is shown in figure 4.32(c), which is asymmetric and is deconvoluted into different three peaks. The main peak at 530.1 eV is assigned the Ti–O bond in TiO<sub>2</sub> particles while the peaks at 532.1 and 533.1 eV is raised from the Ti–O–H or C–O bond and the H–O bond, respectively. The Ti2p XPS spectra in figure 4.32(d) shows the binding energy peaks for Ti2p<sub>1/2</sub> and Ti2p<sub>3/2</sub> located at 464.3 and 458.5 eV with a peak separation of 5.8 eV, implying the presence of the normal state of Ti<sup>4+</sup> in the TCGSs. The deconvoluted Ti2p spectrum confirmed low-intensity peak at 461.1 eV, which were assigned to the Ti–C bond. These results indicated that TiO<sub>2</sub> nanoparticles were chemically linked onto the GO sheets through the sol-gel reaction.

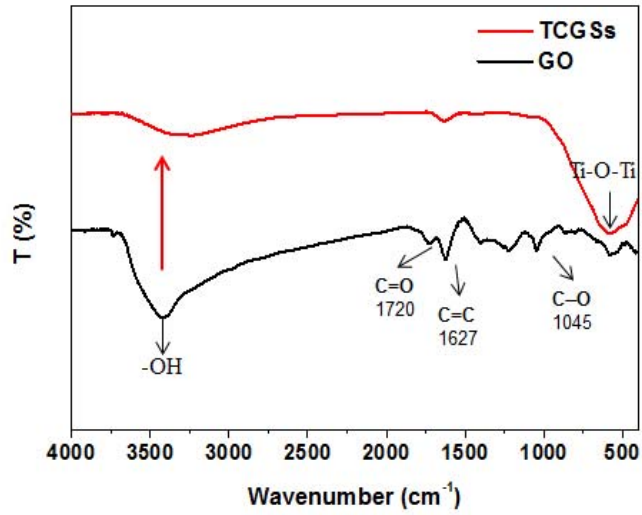


Figure 4.30 FT-IR spectra of GO sheets and TCGSs.

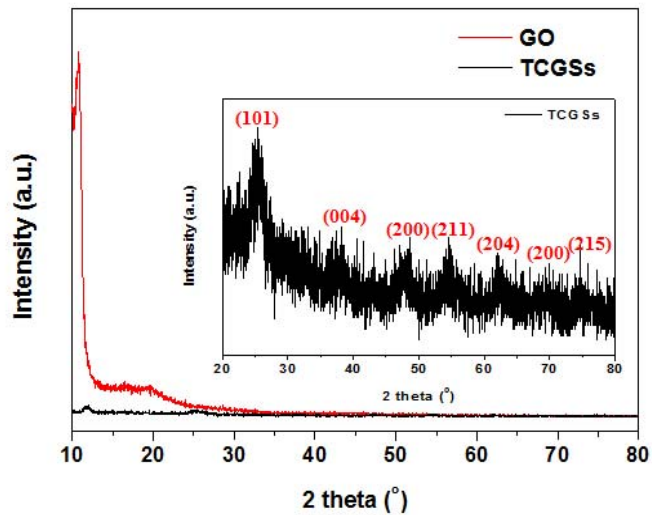
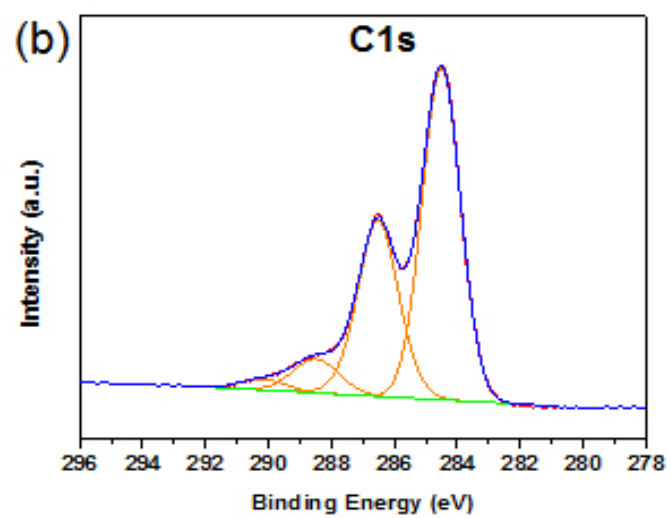
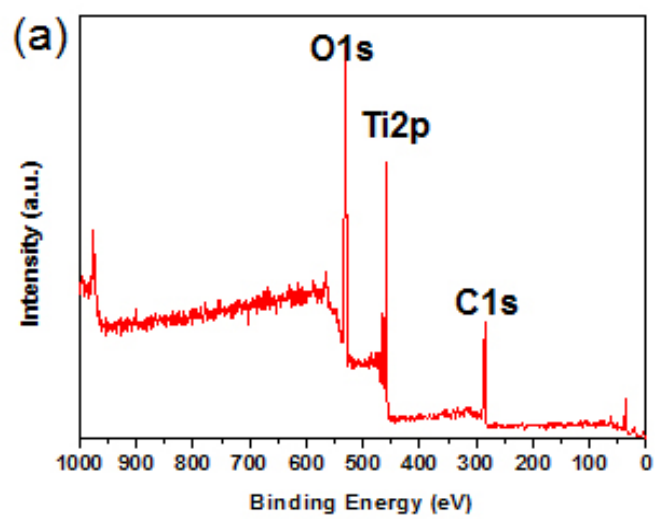


Figure 4.31 (a) XRD patterns of GO sheets and TCGSs (b) the magnified XRD patterns of TCGSs.



(continued)

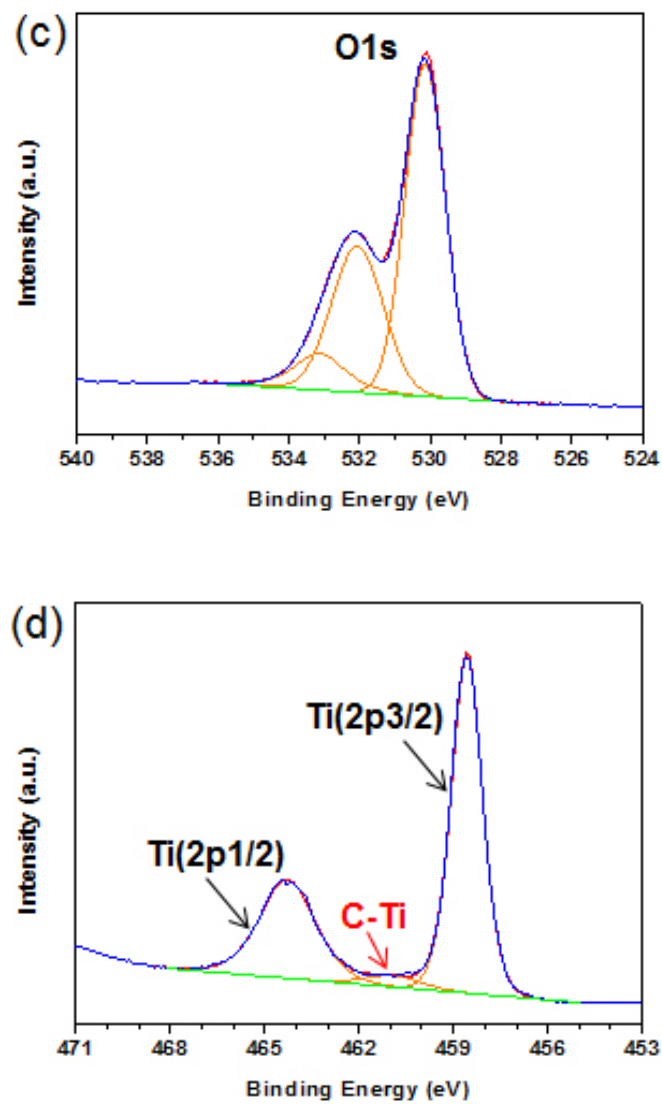


Figure 4.32 (a) XPS spectra of the TCGs and high-resolution XPS spectra of (b) C 1s, (c) O 1s, and (d) Ti 2p.

Table 4.9. Binding energy, FWHM, and peak area percentage of TCGSs, as determined after curve fitting of the XPS high resolution spectra.

Name	Peak BE	FWHM eV	Area (P) CPS.eV	Area %
C1s	284.51	1.47	2168.45	10.59
C1s	286.52	1.57	1235.93	6.03
C1s	288.5	1.75	267.07	1.30
C1s	290.16	1.75	83.8	0.41
O1s	530.15	1.36	4630.48	27.49
O1s	532.06	1.75	3185.53	15.55
O1s	533.13	1.75	856.62	4.18
Ti2p3	458.57	1.2	4624.48	22.58
Ti2p1	464.27	2.16	2430.4	11.87

### 4.2.2. Rheological properties

A microstructural change of granular TiO<sub>2</sub> and TCGSs suspensions was observed using an optical microscope (OM) under an applied electric field. The gap distance between the two parallel electrodes was set up 1 mm. As shown in figure 4.33, granular TiO<sub>2</sub> nanoparticles (P25) appear slightly fibrillation structures. However, randomly distributed TCGSs particles were rapidly transformed into chain-like structures which was formed with connection to the neighboring particles along the applied electric field direction.

Figure 4.34 shows the flow curves of the shear stress and viscosity as a function of shear rate for 5 vol.% TCGSs suspension under external electric fields. And optimal fitting parameters were derived from flow curves of TCGSs suspensions using Bingham and CCJ models and are listed in table 4.10. When the external electric field was not applied, the TCGSs suspension showed typical Newtonian fluid behavior, in which the shear stress increased linearly with increasing shear rate. However, the TCGSs suspension is transformed into Bingham plastic behavior within a wide range of shear rates under external electric fields. It indicates that the electric field induced electrostatic interactions between particles can effectively cause the reorganization of particle chain structure. This strong interaction was attributed to interfacial polarization between titania-coated nanoparticles. As shown in figure 4.34(a), a plateau

region indicates that the re-formation of the destroyed chain-like structures could overcome hydrodynamic shear flow under an applied electric field. The shear stress and viscosity of TCGSs suspension also increased with increasing electric field strength.

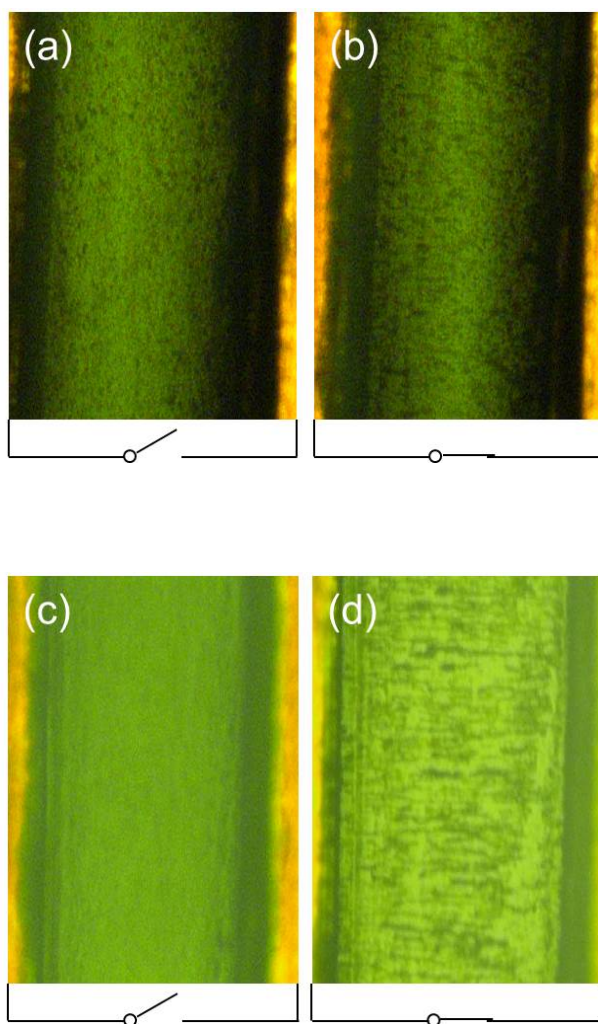


Figure 4.33 Microscope images of chain formation in a silicone oil suspension of P25 and TCGSs (1 wt% in silicone oil) (a, c) without an electric field and (b, d) with) an applied electric field of 1 kV/mm. The gap distance between the two electrodes was 1.0 mm.

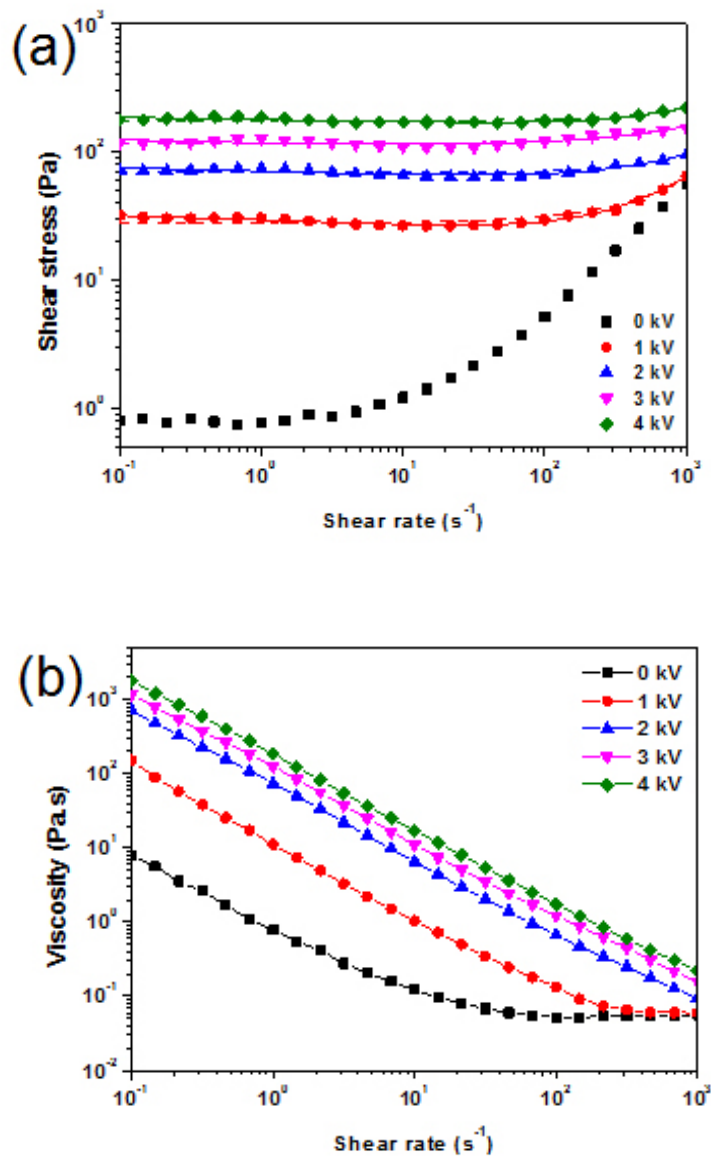


Figure 4.34 (a) Shear stress and (b) viscosity as a function of shear rate for 5 vol.% TCGSs suspension under an applied electric field strength.

Table 4.10 Optimal parameters in Bingham and CCJ model fitting to flow curves of 5 vol.% TCGSs suspension according to electric field strengths.

Model	Parameters	TCGSs(5)				T-MWNT-20(5)	
		Electric field strength (kV/mm)					
		1	2	3	4	1	2
Bingham	$\tau_0$	28.2	69.12	118.1	176.5	13.3	25.63
	$\eta_0$	0.034	0.026	0.043	0.042	0.07	0.077
CCJ	$\tau_0$	35.79	89.3	133.4	203.1	15.3	45.56
	$\eta_\infty$	0.042	0.027	0.044	0.043	0.057	0.038
	$t_1$	0.045	0.089	0.006	0.004	5.145	49.23
	$t_2$	0.158	6.4E-6	1.1E-5	0.007	0.003	6.1E-4
	$\alpha$	0.088	0.087	0.078	0.041	0.199	0.595
	$\beta$	0.783	0.306	0.546	0.287	0.819	0.822

Figure 4.35 shows the dynamic yield stress as a function of electric field strength for the TCGSs suspensions. The correlation between the dynamic yield stress and the external electric field is expressed as the power law relationship as  $\tau_y \propto E^\alpha$ . The dynamic yield stress of TCGSs suspension is proportional to  $E_0^{1.4}$  in a measured electric field range. Although many ER fluids correspond to the polarization model ( $\alpha = 2$ ), the decrease of the gap between the conducting particles in the fluid could cause abnormal electrical response through electrical breakdown under high electric field strengths. The  $\alpha$  (1.4) of TCGSs suspension is similar to  $\alpha$  (1.42) of the T-MWNTs suspension. However, the dynamic yield stress of TCGSs suspension is higher than that of T-MWNTs. This indicates that TCGSs with large specific surface area show stronger shear resistant than T-MWNTs. The TCGSs suspension showed lower current density compared to the T-MWNTs suspension. It is because of lower electrical conductivity of graphene oxide than that of functionalized MWNTs.

Figure 4.36 shows the dynamic yield stress as a function of particle volume fraction for the TCGSs suspensions. The dynamic yield stress of TCGSs based ER fluids gradually increased with increasing the particle volume fraction under fixed electric field strength. It indicates that the interfacial polarization force between particles increase with an increase of the particle concentration. The dynamic yield stress value of TCGSs suspension with 5 vol.% is about 178.8 Pa

under  $4 \text{ kV mm}^{-1}$ , which is about 18 times compared the TCGSs suspension with 1 vol.%.

Frequency effect on the elasticity modulus is an important parameter for understanding the dynamic viscoelastic properties of the ER materials at vibration damping experiments. Figure 4.37 shows the change in storage modulus ( $G'$ ) and loss modulus ( $G''$ ) as a function of frequency at a strain of 0.1% in the linear viscoelastic region. The storage modulus ( $G'$ ) is significantly greater than the loss modulus ( $G''$ ). It indicates that TCGSs suspension exhibit a solid-like behavior under external electric fields. At the same time, it is observed that the shear modulus increase with increasing external electric field strength. It indicates that the increase of electric field strength induces the stronger interparticle interactions, leading to higher rigidity of chain-like structures formed by the dispersed particles. Meanwhile, at low frequencies,  $G'$  becomes independent of frequency because of the stiffer three-dimensional network, which is sufficiently strong to transmit the elastic force through interparticle interactions in the dispersion.

Creep-recovery tests of TCGSs suspension were performed to investigate their viscoelastic properties with or without an electric field (1.5 kV/mm). The creep-recovery experiments are very useful to obtain an insight into the interactions and the mobility of particles. In order to observe time-dependent deformations, the shear stress of 20 Pa was applied to ER fluids for 30 s and then the shear stress was removed. As shown in figure 4.38, the creep deformation

under sustained loading can be divided into two stages. In the creep phase, strain ( $\gamma$ ) of a viscoelastic material increases with time under constant stress ( $\tau$ ), and in the recovery phase, the time-dependent deformation may be recoverable with time after the removal of applied stress. A typical creep-recovery curve for nonlinear viscoelastic behavior is inserted into figure 4.38 and composed of the following three regions:

$$\gamma(t) = \gamma_s + \gamma_d(t) + \gamma_v(t) \quad (4.7)$$

where  $\gamma_s$  is the instantaneous strain,  $\gamma_d(t)$  is the retarded elastic strain, and  $\gamma_v(t)$  is the viscous flow or irreversible component of the strain.

As shown in figure 4.38, the difference in their creep-recovery behaviors between two different electric field strengths is clearly seen. In the absence of an applied electric field, the creep deformation is much larger than that of an electric field under  $1.5 \text{ kV}\cdot\text{mm}^{-1}$  condition. It indicates that TCGSs suspension under zero electric field deforms easily and TCGSs particles show the weak interaction as compared with the electric field with  $1.5 \text{ kV}\cdot\text{mm}^{-1}$ . Also, the strain linearly increased with time under applied stress, which was characterized as ideally viscous material, and recovery was not observed when the applied stress was removed. On the other hand, under an electric field ( $1.5 \text{ kV}/\text{mm}$ ), the TCGSs suspension first showed an instantaneous strain ( $\gamma_s$ ) and elastic strain ( $\gamma_d$ )

followed by a viscous flow ( $\gamma_v$ ) in 30 s. After the applied stress was removed, the elastic recovery ( $\gamma_e$ ) was observed and a reversible viscoelastic recovery ( $\gamma_v$ ) was occurred. It indicates that the electrified dispersions apparently behave like an elastic solid.

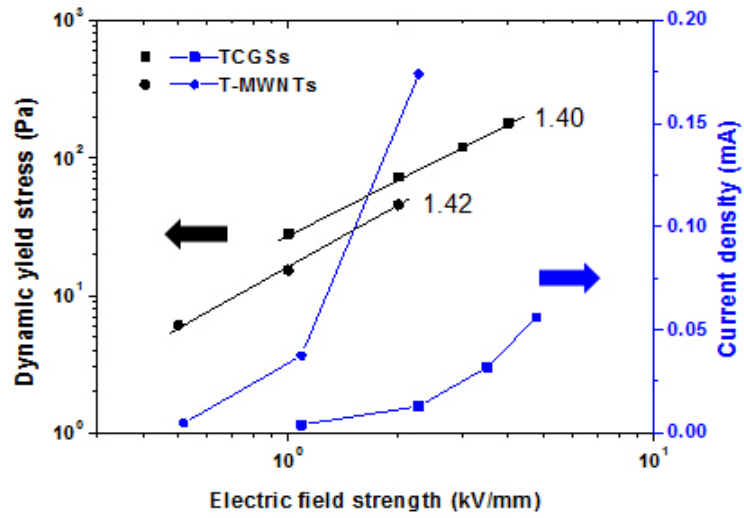


Figure 4.35 Dynamic yield stress and current density as a function of electric field strength for TCGSs and T-MWNTs suspension with 5 vol.%.

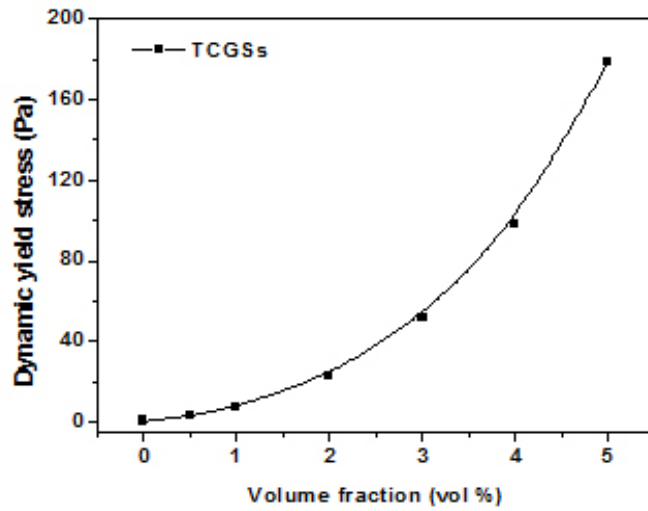


Figure 4.36 Dynamic yield stress as a function of volume fraction for TCGSs suspension under external electric field of 4 kV/mm.

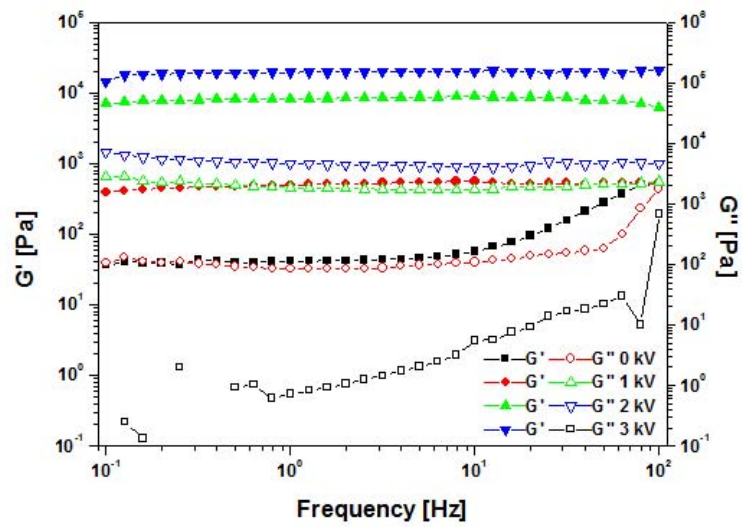


Figure 4.37 Storage modulus ( $G'$ , solid points) and loss modulus ( $G''$ , open points) as a function of frequency for TCGSs suspension 5 vol.% under different electric fields.

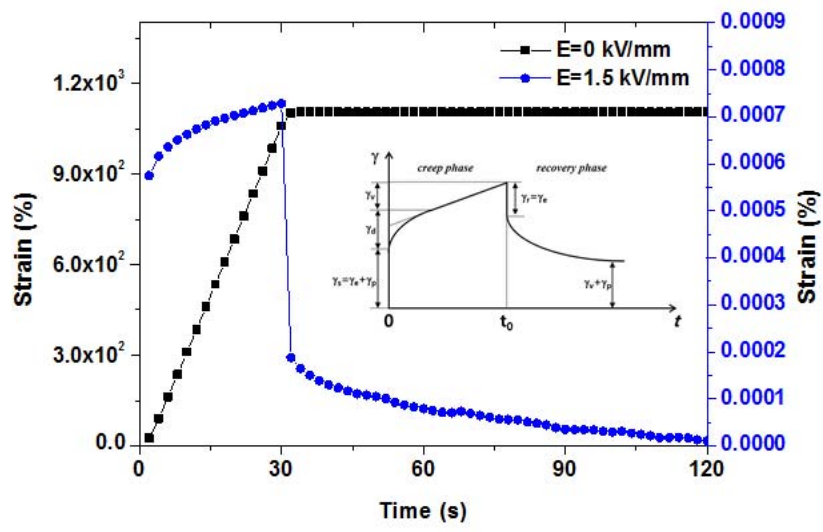


Figure 4.38 Creep-recovery behavior of ER fluids containing TCGSs with 5 vol.% ( $T = 25\text{ }^{\circ}\text{C}$ ).

### 4.2.3. Dielectrical properties

Figure 4.39 shows the permittivity and dielectric loss as a function of the frequency of TCGSs suspensions. The dashed lines are obtained from the Cole-Cole equation which is a useful tool to investigate the relationship between permittivity and ER effects of the ER fluids. The Cole-Cole equation is described by the following equation (4.6).

Among the various parameters, a large polarizability ( $\Delta\epsilon'$ ) and the rate of the interfacial polarization range ( $\tau$ ) are widely acknowledged for good ER materials. The dielectric properties of the TCGSs suspension were examined with a LCR meter in the frequency range of 40–10<sup>7</sup> Hz. From the curve fitting, the  $\Delta\epsilon'$  value of TCGSs suspension was 2.11, which is similar to the T-MWNTs based ER fluids (2.17). However, the relaxation time of T-MWNTs is faster than that of TCGSs. This is caused by entanglement difference of carbon-based nanomaterials and different specific surface area between T-MWNTs and TCGSs. Furthermore, the dielectric loss value of T-MWNTs is higher than that of TCGSs because the ends of the T-MWNTs were not covered completely by TiO<sub>2</sub> after sol-gel synthesis as shown in figure 4.39. And it was attributed to the high electrical conductivity of T-MWNTs network in suspension compared to the TCGSs network in suspension.

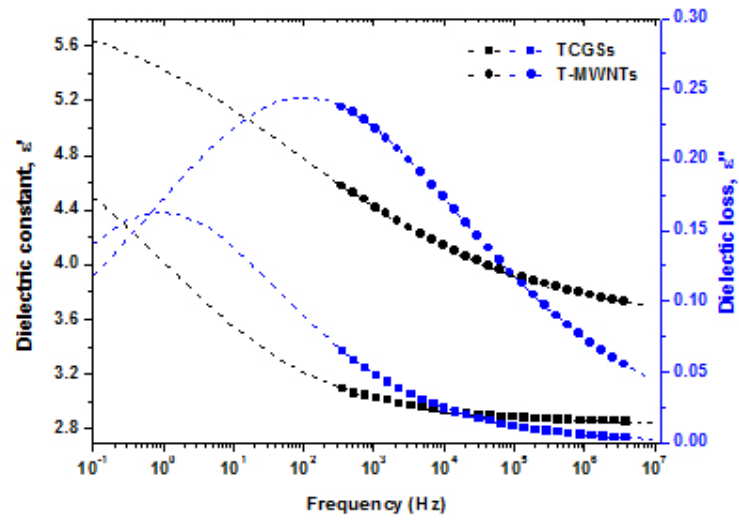


Figure 4.39 Permittivity and dielectric loss factor as a function of the frequency of 5 vol.% TCGSs and T-MWNTs suspension. The dash lines are obtained from equation (4.6).

#### **4.2.4. The effect of T-MWNTs and TCGSs mixture fluids**

To observe mixture effect of T-MWNTs and TCGSs, T-MWNT/TCGSs mixture suspensions at the different weight ratios of 9:1, 7:3, 5:5, 3:7 and 1:9 were prepared by blending T-MWNTs and TCGSs by ultra-sonication and stirring. The T-MWNT/TCGSs mixture suspensions showed the good stability and ER properties of standing over one month without any insoluble bundles or precipitates.

As shown in figure 4.40, the T-MWNT/TCGSs mixture suspension with 3:7 ratio showed the highest dynamic yield stress, while the T-MWNT/TCGSs mixture suspension with 9:1 ratio showed the highest current density compared to the T-MWNTs only or TCGSs only suspension. It indicates that interaction and connection between 1D and 2D nanomaterials is very effective at increasing interference in the shear flow as well as electrical conductivity.

The mixture suspensions show an increase in the yield stress and viscosity compared to the T- MWNTs only or TCGSs only suspensions. It indicated that the mixture suspensions have better dispersion of the T-MWNTs in the presence of TCGSs as well as the interaction between T-MWNTs and TCGSs can act as a strong shear resistant. In the mixture system, packing is more complex, with the 1D MWNTs bridging adjacent 2D graphene sheets. These contacts can prevent the planar contacts of graphene sheets. At the same time, the graphene sheets

may provide steric and electrostatic stabilization, preventing MWNTs re-agglomeration. Thus, one can imagine that the mixture colloids are more prone to form a loosely packed 3D nanoparticle network in the medium. Such ease of forming a 3D network in the sediment may also explain the lower electrical percolation threshold observed in the mixture suspension.

Moreover, electrical conductivity of MWNTs/graphene sheet mixture film with addition of small quantities of graphene can be enhanced without reducing the optical transmittance. In general, mixture nanocomposites show an improvement in the electrical conductivity on account of the free volume theory, since the incorporation of a second nanoparticle reduces the space available between the nanofillers forming a percolated structure with ease, achieving electrical conductivity and lower percolation threshold. In our case the conductive nature of both fillers causes that TCGSs acts as bridges among T-MWNTs, thus facilitating the formation of conductive paths in the mixture composites.

The frequency dependence of dielectric properties of suspension including dielectric particles is also very important for its wide application. Therefore, the frequency dependence of dielectric properties of T-MWNTs/TCGSs mixture suspensions (3 wt%) with various weight ratios were carefully investigated at room temperature and the results are shown in figure 4.41. The  $\Delta\epsilon$  of the mixture suspension slightly decreases from 0.487 to 0.382 with increasing TCGSs, whereas for the dielectric loss of the mixture suspension, the mixture suspension

with 1:9 weight ratio shows a relatively high dielectric loss value within  $10^2 \sim 10^5$  Hz. The dielectric loss is mainly regarded as the contribution of two distinct effects: direct current (DC) conductance and interfacial polarization. The loss of DC conductance dominates at low frequencies, whereas the loss of interfacial polarization dominates at high frequencies. The direct connection path between T-MWNTs and TCGSs leads to a high DC conductance, which contributes to a high dielectric loss and a strong frequency dependence of dielectric loss at low frequency range.

The outstanding performance of T-MWNTs/TCGSs mixture suspension results from a unique interconnected nanostructure with high contact points as well as a large surface area, which shows a synergic effect and improves the interfacial interaction between inter-particles and conducting 3D network.

Finally, the dynamic yield stress and  $\tau_y / \phi^2$  of various anhydrous core-shell ER particle suspensions are listed in table 4.12. The dynamic yield stress of ER particle suspension was determined by characteristic of main component and shell material. And particle made up of titania and conductivity polymer or carbon nanomaterials showed high ER performance. However, current density of ER suspension is not to be underestimated.

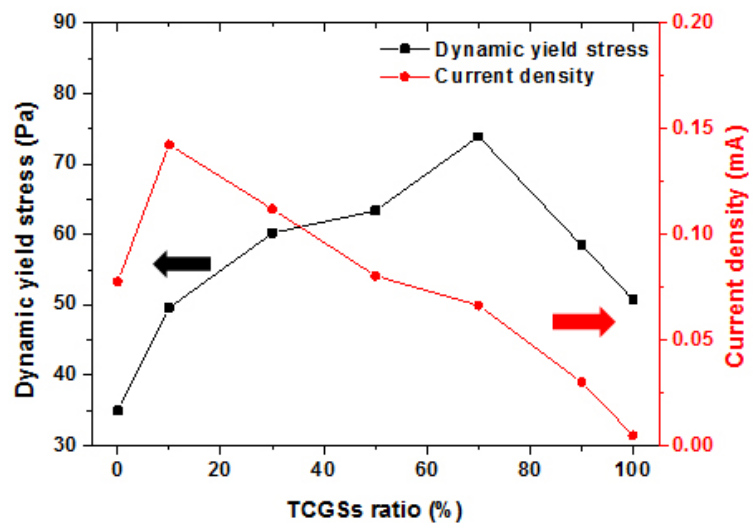


Figure 4.40 Dynamic yield stress and current density of T-MWNTs/TCGSs mixture suspensions with 3 vol.% as a function of TCGSs ratio.

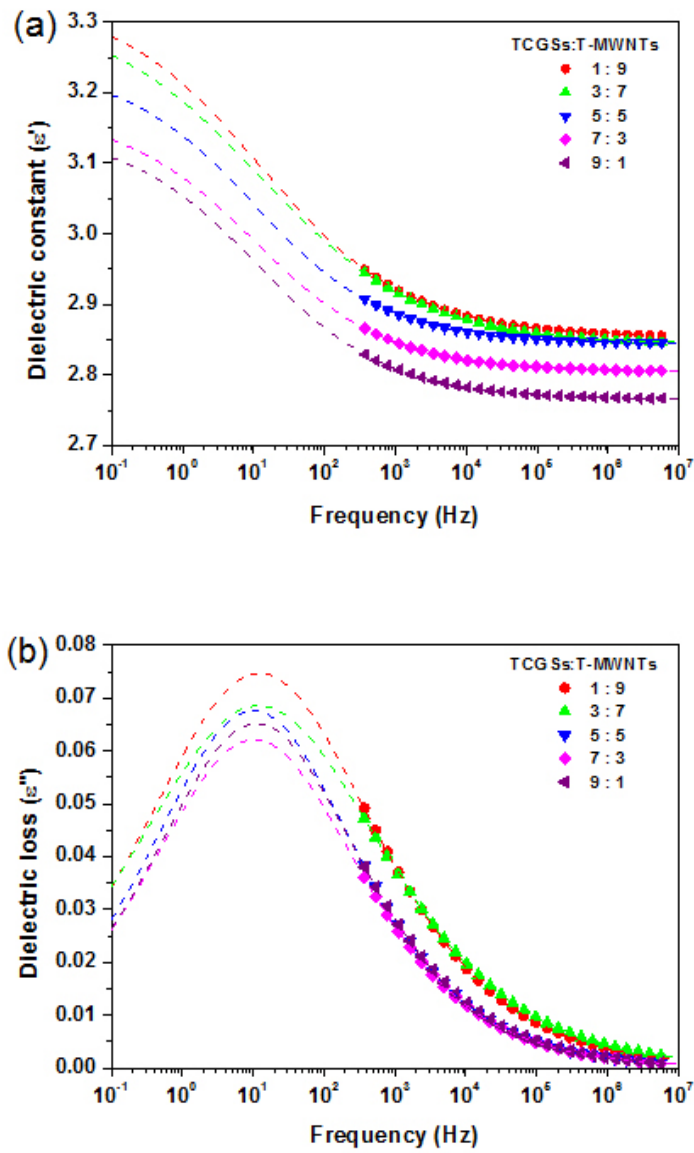


Figure 4.41 (a) Dielectric constant and (b) dielectric loss of T-MWNTs/TCGSs mixture suspensions with 3 vol.% as a function of frequency ( $T = 25$  °C). Fitting lines are generated from the Cole-Cole equation (4.6).

Table 4.11 Dielectric parameters of T-MWNTs/TCGSs mixture suspensions as TCGSs contents ratio obtained from the Cole-Cole fitting.

TCGSs : T-MWNTs	$\epsilon'_0$	$\epsilon'_\infty$	$\Delta\epsilon' = \epsilon'_0 - \epsilon'_\infty$	$\tau$	$\alpha$
1:9	3.31	2.86	0.45	$1.12 \times 10^{-2}$	0.71
3:7	3.29	2.85	0.44	$1.10 \times 10^{-2}$	0.64
5:5	3.25	2.84	0.41	$1.46 \times 10^{-2}$	0.64
7:3	3.20	2.81	0.39	$1.51 \times 10^{-2}$	0.69
9:1	3.14	2.76	0.38	$1.22 \times 10^{-2}$	0.58

Table 4.12 The comparison of dynamic yield stress and  $\tau_y / \phi^2$  of various core-shell ER particle suspensions.

(under 2kV/mm)					
Type of particles (vol%)	Dynamic yield stress (Pa)	$\tau_y / \phi^2$	Type of particles (vol%)	Dynamic yield stress (Pa)	$\tau_y / \phi^2$
PANI coated Titanate (5)	55	2.2	MWNT coated PMMA (10)	30	0.3
Silica particle coated PANI (10)	90	0.9	MWNT barium titanate (49)	4500	1.87
Titania coated PANI (10)	330~400	3.3~4	MWNT coated silica (6)	25	0.69
Titanate coated PANI (5)	60	2.4	Polyaniline/MWNTs (10)	130	1.3
Titania coated silica nanotube (15)	2750	12.2	MWNT coated PS (5)	80	3.2
Silica coated MWNTs-20 (5)	7.5	0.3	MWNT coated PAN (15)	200	0.88
Titania coated MWNTs-20 (5)	45.5	1.8	Titania coated graphene (5)	75	3
Silica coated MWNTs-20 (20)	220.1	0.55	TCGS/T-MWNTs Hybrid (3)	74	8.22
Silica coated MWNTs-40 (20)	187.1	0.46	PPy coated graphene (5)	300	12
Titania coated MWNTs-40 (20)	880.3	2.2	Graphene coated PS (15)	10.8	0.048
Silica-titania coated MWNTs-40 (20)	615.2	1.6	Silica coated graphene (9)	78	0.96
Titania-silica coated MWNTs-40 (20)	295.9	0.74	PANI coated graphene (10)	500	5

ER materials with 1 dimensional structure  
ER materials including graphene

ER materials including MWNT

#### 4.2.5. Summary

2D sandwich-like titania-coated graphene sheets was successfully synthesized by sol-gel process using TBT as titania particle precursor. The titania-coated graphene sheets have the high dielectric performance including high permittivity and low dielectric loss. It has been found that the high permittivity is mainly due to interfacial polarization. Conductivity of the titania-coated graphene sheets was brought into the suitable range for ER measurements. The results showed that the titania-coated graphene sheets suspensions possessed versatile ER performance including high ER effect and good dispersion stability. The creep-recovery tests revealed that the titania-coated graphene sheets show purely viscous behavior under  $E = 0$  kV/mm and show recoverable viscoelastic behavior under  $E = 1.5$  kV/mm conditions. Finally, the titania-coated MWNT/graphene sheets mixture suspension showed the good stability of standing as well as the good performance in ER effects. Electrical conductivity of mixture suspension was improved due to a unique interconnected nanostructure with high contact points and a large surface area, which shows a synergic effect and improves the interfacial interaction between inter-particles and conducting 3D network.

### **4.3. The fiber mats including ER fluid**

#### **4.3.1. Characterization**

Coaxial electrospinning has been usually done with two polymer solutions which are both independently electrospinnable. However, silicone or mineral oil and conductive polymers were non-electrospinnable owing to low molecular weight, limited solubility, or lack of viscoelastic properties [175-177]. In this study, there are many challenges in obtaining such a clean morphology. However, we adjusted viscosity of non-electrospinnable core materials and selected shell material being effectively electrospinnable by itself as well as acting as a guide for the non-electrospinnable core.

Figure 4.42 and figure 4.43 show the SEM and TEM images of the ER fluids/PET core-sheath fiber mats with different ER particle content and different feeding rate of inner solution. Relatively uniform and bead-free ER fluids/PET core-sheath fibers were prepared via coaxial electrospinning. Continuous fibers with bead-free morphology could be formed under the following parameters: outer (PET) solution concentration was 12 wt% as optimal condition, voltage was set as 13-15 kV and the feeding rate of inner and outer solution were set as 0.3 mL/h and 2.0 mL/h, respectively. The surface of

the electrospun fibers containing from 0 to 2 wt% of inorganic-coated MWNTs was very smooth as well as the inorganic-coated MWNT was fully incorporated in core part. In case of the fibers containing 4 wt% of inorganic-coated MWNTs, low surface roughness and unevenness were observed. However, considerable aggregation and local irregularities were observed as the inorganic-coated MWNTs content increased to 8 wt%. Also, the irregular surface and bead of the fiber structure can influence the mechanical properties of the composite samples. Generally, to improve the morphological properties of the fabricated composite fibers containing inorganic-coated MWNTs, the dispersion condition is very critical and plays a significant role in achieving effective properties.

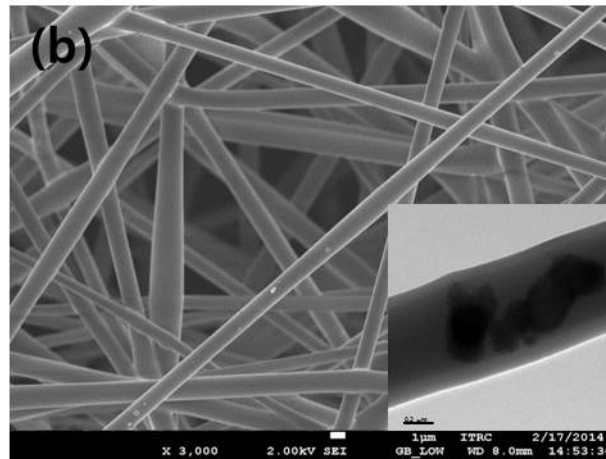
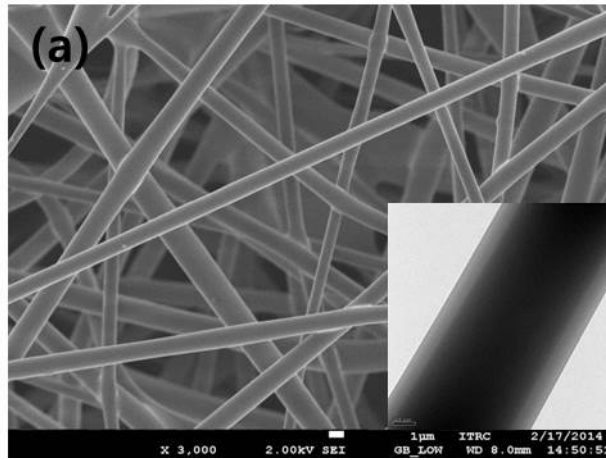
Change in the average diameter of fiber samples versus the inorganic-coated MWNTs concentration is shown in figure 4.44. The diameter of the fibers which were measured from each sample is determined by the inorganic-coated MWNTs content. With increasing the concentration of inorganic-coated MWNTs in the solution from 0 to 4 wt%, the mean diameter of fibers slightly increased from  $928 \pm 58$  nm to  $1407 \pm 105$  nm. When inorganic-coated MWNTs concentration was increased to 8 wt%, however, the average diameter increased, furthermore showed bimodal size distribution. It indicated that the increase in fiber diameter was caused by an increase of core conductivity and aggregation of particles.

In the electrospinning process, the viscosity and conductivity of the core solution are very important parameters, which can affect the composite fiber

diameters and the uniformity of fiber surface. As described above, mostly with increasing the viscosity and conductivity of the electrospinning solution, the average diameter of fibers increased. With increasing of inorganic-coated MWNTs concentration of the ER fluids from 0 wt% to 4 wt%, the viscosity and conductivity of solution were slightly increased. However, when the inorganic-coated MWNT concentration was increased to 8 wt%, the viscosity and conductivity increased noticeably. The viscosity and conductivity of core solution are listed in table 4.13.

Table 4.13 The change in viscosity and conductivity values against core particle concentration.

Solution properties	1 wt%	2 wt%	4 wt%	8 wt%
Viscosity (Pa·s)	13.85	14.27	14.35	16.75
Conductivity (S/m)	$8.40 \times 10^{-12}$	$6.71 \times 10^{-12}$	$2.02 \times 10^{-10}$	$1.90 \times 10^{-9}$



(continued)

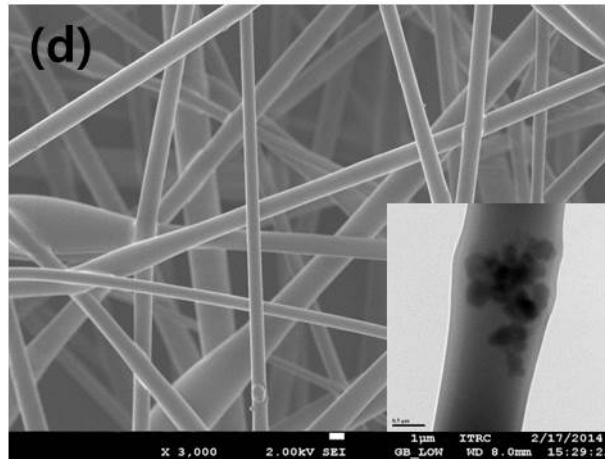
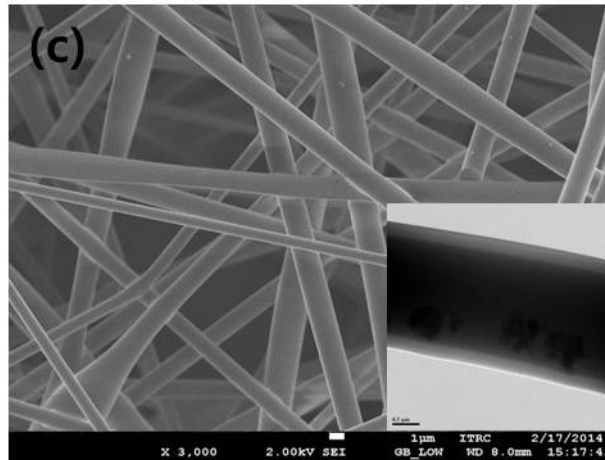


Figure 4.42 SEM and TEM images of the core (ERF)/sheath (PET) fiber mats with the ST-MWNTs concentrations of (a) 1 wt%, (b) 2 wt%, (c) 4 wt%, and (d) 8 wt%.

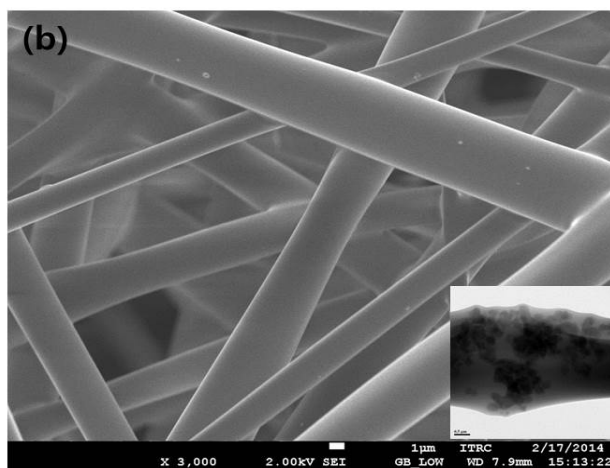
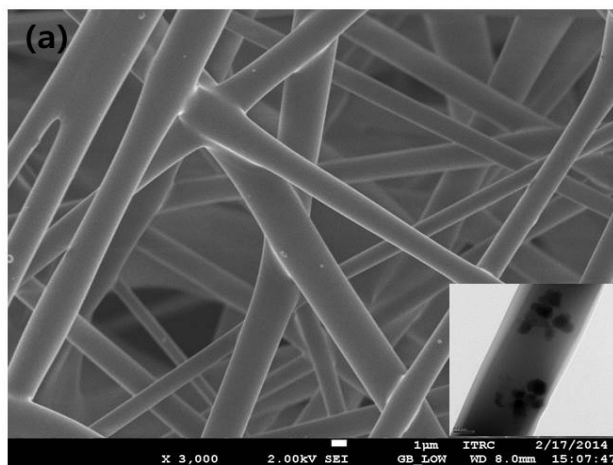


Figure 4.43 SEM and TEM images of core (ERF)/sheath (PET) fiber mats fabricated at different core flow rates of (a) 0.45 ml/h, and (b) 0.6 ml/h, when the sheath flow rate was fixed at 2 ml/h.

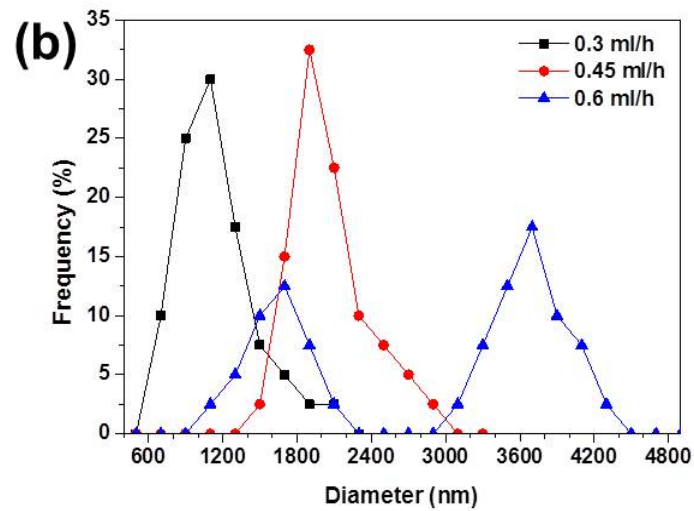
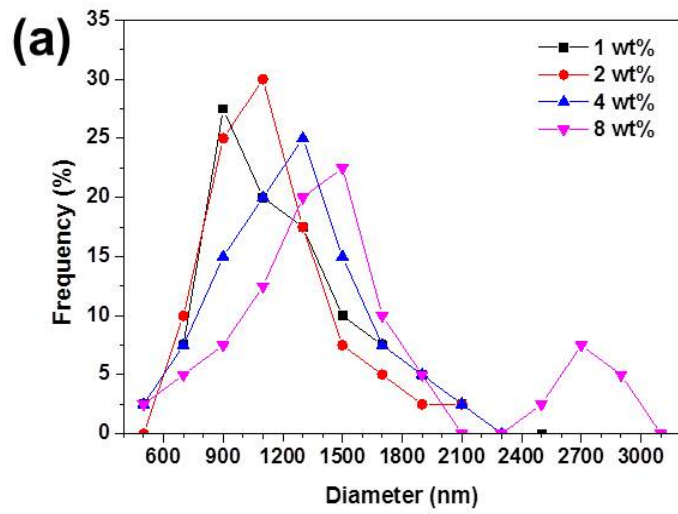


Figure 4.44 Diameter distribution diagrams of core (ERF)/sheath (PET) fiber (a) as various concentrations of core fluids and (b) as under different core flow rate (4 wt% core particles).

### 4.3.2. Mechanical properties

The mechanical properties of the electrospun fiber mats with core-sheath structure, obtained from different core particle concentrations, were measured by the universal testing machine (Instron, 5566) under different electric field strength. The specimens of fiber mat were cut into 100 mm x 20 mm rectangular shapes as shown in figure 4.45 Tensile testing was performed using a 10 N load cell at extension rate of 50 mm/min. The strength of the nanofiber mat was calculated from Equation (4.8). The modulus and elongation at break were obtained from the stress–strain curves. The mechanical data were acquired with five independent experiments, and all data were displayed as mean values and standard deviation.

$$\sigma(Mpa) = \frac{\rho(g / cm^3) \times F(cN)}{T(cm) \times A(g / m^2)} \quad (4.8)$$

where  $\sigma$  is tensile strength,  $\rho$  is density,  $F$  is tensile force,  $T$  is the thickness of the nanofiber sample, and  $A$  is cross-sectional area density.

The specimens were loaded in tensile tests both with and without an electric field but the results obtained under zero electric fields as different core particle concentrations were not presented because the value of tensile test existed in

standard deviation. It is thought that random orientation or interaction between particles in silicon oil was not doing enough to resist tensile strength under zero electric field.

The modulus and elongation at break of fiber mats were obtained from the stress-strain curves. The mechanical data were obtained with five independent samples, and all data were shown as mean values and standard deviation. Representative uniaxial stress-strain curves for different particle concentrations in core solution under external electric field (140 V/mm) and 4 wt% fiber mats under different electric fields are shown in figure 4.46.

As it can be seen from figure 4.46(a), the initial portion of the stress-strain curve exhibits the typical elastic behavior, corresponding to a high resistance to deformation due to cohesive forces in the fiber assembly. With increasing the inorganic-coated MWNTs concentration to core solution in the range from 0 wt% to 4 wt%, the fiber mats transformed flexible into brittle and the tensile strength and modulus increased obviously under external electric field. Compared to the fiber mats including only silicone oil, the tensile strength of the fiber mats containing 4 w% ER particles is increased by 37.6%, and the tensile modulus is increased by 42.8%. This is because the interaction between the inorganic-coated MWNTs was caused by interfacial polarization induced by external electric fields and the perpendicular component to the tensile axis of such dipole-dipole interactions can act as a resistance force against the tensile stress. As the dipole-dipole interaction is inversely proportional to the square of

distance between the nanoparticles, this instant reinforcement effect of inorganic-coated MWNTs nanoparticles under an electric field is more prominent in the initial stage of tensile deformation. Once polarization has been established, the interaction of interparticle columbic forces leads to the formation of a fibrillated network.

Consequently, further improvement was observed in modulus values than tensile strength values. With the tensile deformation progressed, the distance between the nanoparticles increases along the tensile axis, while decreases along the direction perpendicular to the tensile axis. Upon further tensile deformation, the distance between the nanoparticles perpendicular to the tensile axis become close enough to form aggregations due to the dipole-dipole interaction. Such aggregations act as stress concentrators, decreasing the strain. However, when inorganic-coated MWNTs were increased to 8 wt%, the tensile strength and modulus decreased. The increase of core particles can cause the collapse of core-sheath structure as well as form unstable fiber structure due to agglomeration of the particles. Table 4.14 shows the tensile strength, modulus and elongation at break as the variation of the inorganic-coated MWNT concentrations in the electrospun fibers.

As shown in figure 4.46(b), with increasing the external electric field strength, the ERF/PET core-sheath fiber mats showed the increase of tensile strength and modulus, but showed the decrease of breaking strain. This is because the strong interaction between particles was induced with increasing the

external electric fields. The tensile test results as a function of electric fields are listed in table 4.15.

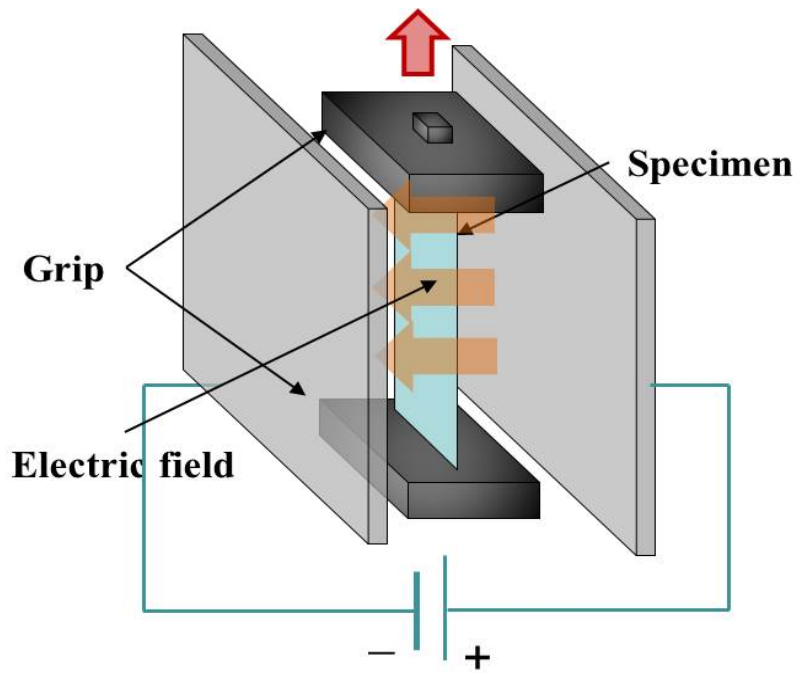


Figure 4.45 A schematic diagram of tensile test with an electric field.

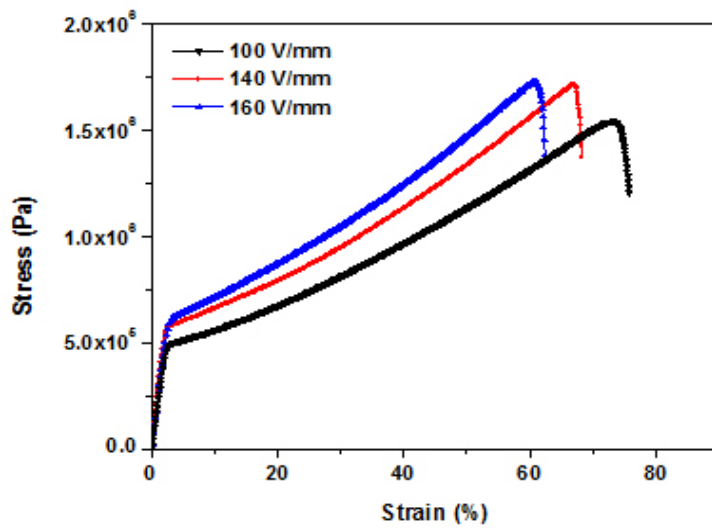
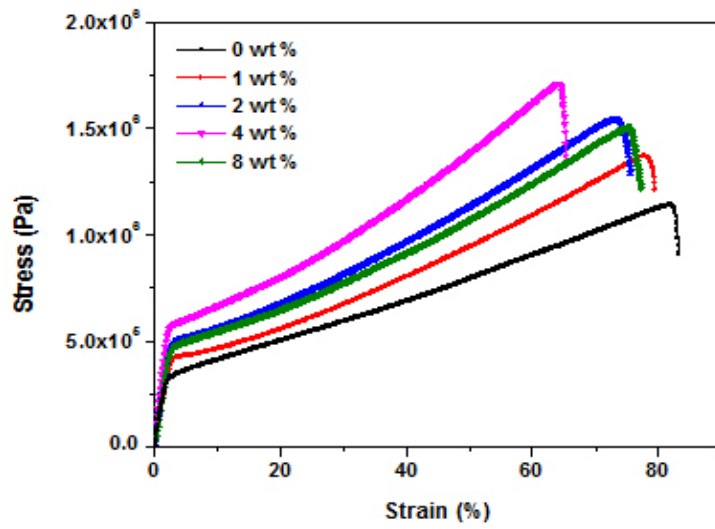


Figure 4.46 Typical stress-strain curves of core (ERF)/sheath (PET) fiber mats (a) as various concentrations of core fluids and (b) fiber mats including 4 wt% core particles as under different external electric fields.

Table 4.14 Tensile properties of the fiber mats with and without an electric field.

Sample	Tensile strength (MPa)	Elongation at break (%)	Modulus (MPa)
0 wt%	1.19±0.008	82±1.51	16.13±0.86
1 wt%	1.21±0.025	81±2.12	21.29±1.45
2 wt%	1.35±0.034	81±2.46	23.83±0.32
4 wt%	1.39±0.017	78±2.54	25.21±1.62
8 wt%	1.26±0.054	81±3.98	24.11±2.02
1 wt% (140 V/mm)	1.35±0.025	78±3.23	23.39±0.52
2 wt% (140 V/mm)	1.72±0.034	72±2.86	26.78±0.48
4 wt% (140 V/mm)	1.91±0.017	65±2.54	28.21±1.32
8 wt% (140 V/mm)	1.49±0.054	74±3.98	25.53±0.58

Table 4.15 Tensile properties of fiber mats as different electric fields.

Sample	Tensile strength (MPa)	Elongation at break (%)	Modulus (MPa)
100 V/mm (4 wt% )	1.59±0.08	75±3.51	26.52±0.89
140 V/mm (4 wt% )	1.91±0.017	65±2.54	28.21±1.32
160 V/mm (4 wt% )	1.95±0.024	62±2.86	29.87±1.95

### 4.3.3. Summary

With the addition of inorganic-coated MWNTs in core solution from 1 to 8 wt%, an obvious increase in the viscosity and conductivity was observed. We also fabricated core/sheath typed fiber mats consisting of inorganic-coated MWNTs suspension/PET by co-axial electrospinning techniques. We confirmed that inorganic-coated MWNTs were well embedded in the electrospun fibers from TEM images. With increasing the particle concentrations, the average fiber diameter increased as well as the surface roughness of fibers was slightly increased. The analysis of the mechanical properties of the fiber mats reveals that they exhibit an enhancement in the tensile strength and the tensile modulus with increasing of the particle concentration and the external electric field, as compared to the fiber mats without particles. This is because interaction between particles increases with increasing of the particle concentration and the external electric field. As the particle concentration is further increased, the tensile strength and modulus are decreased, which is attributed to the unstable fiber structure and the particle aggregation. Thus, it can be seen that the homogeneous dispersion of inorganic-coated MWNTs is comparably important for an excellent composite fiber mats. The results of our study can be led to the application of field-responsive protection.

## 5. Conclusions

First, a facile route to synthesize nanofibrous inorganic-coated MWNTs was fabricated using sol-gel process in a room temperature. The titania-coated MWNTs ER fluids showed a stronger ER effect compared to the silica-coated MWNTs ER fluids at the same particle volume fraction. The dielectric properties including high permittivity and low dielectric loss of the titania-coated MWNTs ER fluids has much higher than that of the silica-coated MWNTs ER fluids. It has been found that the high permittivity is mainly due to interfacial polarization.

Second, the silica-coated MWNTs suspension with different shell thickness and inorganic-coated MWNTs suspension with different shell sequence were fabricated. The ER performance of the S-MWNTs suspension increases with an increase of the shell thickness. However, the S-MWNTs suspension with a shell thickness of 40 nm showed weaker ER effect than S-MWNTs suspension with shell thickness of 20 nm. It indicates that ER behavior is influenced by the dielectric properties and the electrical conductivity of nanoparticles. In the case of inorganic-coated MWNTs with different sequence, the ER effect and

dielectric performance of the T-MWNTs ER fluids appeared much higher than the S-MWNTs ER fluids at the same particle volume fraction. However, the high current density of T-MWNTs could be restricted in the application of ER fluids because the high current density of ER fluids can cause an electrical short under the low electric field. Therefore, it is expected that the ST-MWNTs ER fluid has high potential in the application of ER fluids due to high ER performance, low current density and high dispersion stability. The permittivity of the MWNTs based ER fluids can be controlled by the coating materials on MWNTs.

Third, 2D sandwich-like titania-coated graphene sheets was synthesized by sol-gel process to compare the effect as dimension of particles. The TCGSs suspension showed the similar  $\Delta\varepsilon_0'$  comparison to T-MWNT-20 but dielectric loss of TCGSs suspension was lower than that of T-MWNT-20 suspension. The TCGSs suspensions possessed versatile ER performance including high ER effect and good dispersion stability. The TCGSs suspension show purely viscous behavior under  $E = 0$  kV/mm but recoverable viscoelastic behavior under  $E = 1.5$  kV/mm. The T-MWNT/TCGSs mixture suspension showed the good stability of standing and the outstanding performance in ER effects and electric conductivity due to a unique interconnected nanostructure with highly contact numbers and a large surface area, which shows a synergic effect and improves the interfacial interaction between inter-particles and conducting 3D network.

Finally, we fabricated ERF/PET core/sheath fiber mats by co-axial electrospinning techniques. Inorganic-coated MWNTs suspension was well embedded in the electrospun fibers. With increasing the core particle concentrations, the average fiber diameter increased as well as the surface roughness of fibers was slightly increased. The mechanical properties of the fiber mats exhibited an enhancement in the tensile strength and the tensile modulus with increasing of the particle concentration and the external electric field, as compared to the core/sheath fiber mats without particles. This is because interaction between particles increases with increasing of the particle concentration and the external electric field. The results of our study can be led to the application of field-responsive protection.

## 6. Bibliography.

- [1] Winslow WM, Induced fibrillation of suspensions, *J. Appl. Phys.* 1949, 20, 1137-40.
- [2] Wen WJ, Huang XX, Yang SH, Lu KQ, Sheng P, The giant electrorheological effect in suspensions of nanoparticles, *Nat. Mater.* 2003, 2, 727-30.
- [3] Zhang JW, Gong XQ, Liu C, Wen WJ, Sheng P, Electrorheological fluid dynamics, *Phys. Rev. Lett.* 2008, 101, 194503.
- [4] Qiao YP, Zhao X, Electrorheological effect of carbonaceous materials with hierarchical porous structures, *Colloid. Surface. A.* 2009, 340, 33-9.
- [5] Yin JB, Zhao XP, Xiang LQ, Xia X, Zhang ZS, Enhanced electrorheology of suspensions containing sea-urchin-like hierarchical Cr-doped titania particles, *Soft Matter* 2009, 5, 4687-97.
- [6] Weiss KD, Carlson JD, Nixon DA, Viscoelastic properties of magnetorheological and electrorheological fluids, *J. Intel. Mat. Syst. Str.* 1994, 5, 772-5.
- [7] Hao T, Electrorheological fluids. *Adv. Mater.* 2001, 13, 1847-57.
- [8] Tang H, Luo CR, Zhao XP, Sonic resonance in a sandwiched

- electrorheological panel, *J. Appl. Phys.* 2005, 98, 016103.
- [9] Filisko FE, Radzilowski LH, An intrinsic mechanism for the activity of aluminosilicate based electrorheological materials, *J. Rheol.* 1990, 34, 539-52.
- [10] Tian Y, Meng YG, Wen SZ, Electrorheology of a zeolite/silicone oil suspension under dc fields, *J. Appl. Phys.* 2001, 90, 493-6.
- [11] Yin JB, Zhao XP, Preparation and enhanced electrorheological activity of TiO<sub>2</sub> doped with chromium ion, *Chem. Mater.* 2004, 16, 321-8.
- [12] Gao ZW, Zhao XP, Two roles of guest and crosslinked degree on hydrosoluble beta-cyclodextrin polymer electrorheological fluids, *Polymer* 2004, 45, 1609-15.
- [13] Sung JH, Park DP, Park BJ, Choi HJ, Jhon MS, Phosphorylation of potato starch and its electrorheological suspension, *Biomacromolecules*, 2005, 6, 2182-8.
- [14] Block H, Kelly JP, Qin A, Watson T, Materials and mechanisms in electrorheology, *Langmuir* 1990, 6, 6-14.
- [15] Fang FF, Lee BM, Choi HJ, Electrorheologically intelligent polyaniline and its composites, *Macromol. Res.* 2010, 18, 99-112.
- [16] Cho MS, Choi HJ, Ahn WS, Enhanced electrorheology of conducting polyaniline confined in MCM-41 channels, *Langmuir* 2004;20(1):202-7.
- [17] Yin JB, Zhao XP, Preparation and electrorheological activity of mesoporous rare-earth-doped TiO<sub>2</sub>, *Chem. Mater.* 2002, 14, 4633-40.
- [18] Bao W, Zheng J, Wu XF, Cao JG, Yang ZJ, Ren N, et al, Short axis contact

in the chaining of ellipsoidal particles of polar molecule dominated electrorheological fluid, *J. Phys-Condens. Mat.* 2010, 22, 324105.

- [19] Kojima Y, Matsuoka T, Takahashi H, Electrorheological properties of suspension of diphenyldiacetylene annealed under elevated pressure, *J. Appl. Polym. Sci.* 1994, 53, 1393-6.
- [20] Yin JB, Xia XA, Xiang LQ, Zhao XP, Temperature effect of electrorheological fluids based on polyaniline derived carbonaceous nanotubes, *Smart. Mater. Struct.* 2011, 20, 015002.
- [21] Tam WY, Yi GH, Wen WJ, Ma HR, Loy MMT, Sheng P, New electrorheological fluid: Theory and experiment, *Phys. Rev. Lett.* 1997, 78, 2987-90.
- [22] Liu YD, Fang FF, Choi HJ, Core-shell structured semiconducting PMMA/Polyaniline snowman-like anisotropic microparticles and their electrorheology, *Langmuir* 2010, 26, 12849-54.
- [23] Yin JB, Zhao XP, Titanate nano-whisker electrorheological fluid with high suspended stability and ER activity, *Nanotechnology* 2006, 17, 192-6.
- [24] Yin JB, Zhao XP, Xia X, Xiang LQ, Qiao YP, Electrorheological fluids based on nano-fibrous polyaniline, *Polymer* 2008, 49, 4413-9.
- [25] Cheng QL, Pavlinek V, He Y, Li CZ, Saha P, Electrorheological characteristics of polyaniline/titanate composite nanotube suspensions, *Colloid. Polym. Sci.* 2009, 287, 435-41.
- [26] Yin JB, Xia X, Xiang LQ, Qiao YP, Zhao XP, The electrorheological effect

- of polyaniline nanofiber, nanoparticle and microparticle suspensions, *Smart Mater. Struct.* 2009, 18, 095007.
- [27] Yin JB, Xia XA, Xiang LQ, Zhao XP, Conductivity and polarization of carbonaceous nanotubes derived from polyaniline nanotubes and their electrorheology when dispersed in silicone oil, *Carbon* 2010, 48, 2958-67.
- [28] Mrlik M, Pavlinek V, Saha P, Quadrat O, Electrorheological properties of suspensions of polypyrrole-coated titanate nanorods, *Appl. Rheol.* 2011, 21, 52365.
- [29] Xia XA, Yin JB, Qiang PF, Zhao XP, Electrorheological properties of thermo-oxidative polypyrrole nanofibers, *Polymer* 2011, 52, 786-92.
- [30] Yin JB, Zhao XP, Electrorheology of nanofiber suspensions, *Nanoscale. Res. Lett.* 2011, 6, 256.
- [31] Kim T, Jung G, Yoo S, Suh KS, Ruoff RS, Activated graphene-based carbons as supercapacitor electrodes with macro- and mesopores, *Acs Nano* 2013, 7, 6899-905.
- [32] Suk JW, Lee WH, Lee J, Chou H, Piner RD, Hao YF, Enhancement of the electrical properties of graphene grown by chemical vapor deposition via controlling the effects of polymer residue, *Nano Lett.* 2013, 13, 1462-7.
- [33] Wu ZC, Chen ZH, Du X, Logan JM, Sippel J, Nikolou M, Transparent, conductive carbon nanotube films, *Science* 2004, 305, 1273-6.
- [34] Kim JY, Jeong T, Baik CW, Park SH, Han I, Kim GH, Field-emission performance and structural change mechanism of multiwalled carbon

- nanotubes by oxygen plasma treatment, *Thin Solid Films* 2013, 547, 202-6.
- [35] Zhang L, Wang ZP, Xu C, Li Y, Gao JP, Wang W, High strength graphene oxide/polyvinyl alcohol composite hydrogels, *J. Mater. Chem.* 2011, 21, 10399-406.
- [36] Nagahara LA, Amlani I, Lewenstein J, Tsui RK, Directed placement of suspended carbon nanotubes for nanometer-scale assembly, *Appl. Phys. Lett.* 2002, 80, 3826-8.
- [37] Oliva-Aviles AI, Aviles F, Sosa V, Oliva AI, Gamboa F, Dynamics of carbon nanotube alignment by electric fields, *Nanotechnology* 2012, 23, 465710.
- [38] Liu XM, Spencer JL, Kaiser AB, Arnold WM, Electric-field oriented carbon nanotubes in different dielectric solvents, *Curr. Appl. Phys.* 2004, 4, 125-8.
- [39] Oh SY, Oh MK, Kang TJ, Characterization and electrorheological response of silica/titania-coated MWNTs synthesized by sol-gel process, *Colloid. Surface. A.* 2013, 436, 354-62.
- [40] Oh SY, Kang TJ, Electrorheological response of inorganic-coated multi-wall carbon nanotubes with core-shell nanostructure, *Soft Matter* 2014, 10, 3726-37.
- [41] Zhang WL, Choi HJ, Fast and facile fabrication of a graphene oxide/titania nanocomposite and its electro-responsive characteristics, *Chem. Commun.* 2011, 47, 12286-8.
- [42] Hong JY, Lee E, Jang J, Electro-responsive and dielectric characteristics of graphene sheets decorated with TiO<sub>2</sub> nanorods, *J. Mater. Chem. A.* 2013, 1,

117-21.

- [43] Park SJ, Cho MS, Lim ST, Choi HJ, Jhon MS, Electrorheology of multiwalled carbon nanotube/poly(methyl methacrylate) nanocomposites, *Macromol. Rapid. Comm.* 2005, 26, 1563-6.
- [44] Kim B, Lee YH, Han SJ, Ryu JH, Suh KD, Electrorheological properties of carbon nanotubes-coated monodisperse polymeric microspheres, *Colloid. Surface. A.* 2007, 298, 245-51.
- [45] Yin JB, Wang XX, Chang RT, Zhao XP, Polyaniline decorated graphene sheet suspension with enhanced electrorheology, *Soft Matter* 2012, 8, 294-7.
- [46] Hu HT, Wang XB, Wang JC, Liu FM, Zhang M, Xu CH, Microwave-assisted covalent modification of graphene nanosheets with chitosan and its electrorheological characteristics, *Appl. Surf. Sci.* 2011, 257, 2637-42.
- [47] Yang SY, Lin WN, Huang YL, Tien HW, Wang JY, Ma CCM, Synergetic effects of graphene platelets and carbon nanotubes on the mechanical and thermal properties of epoxy composites, *Carbon* 2011, 49, 793-803.
- [48] Chatterjee S, Nafezarefi F, Tai NH, Schlagenhaut L, Nuesch FA, Chu BTT, Size and synergy effects of nanofiller mixtures including graphene nanoplatelets and carbon nanotubes in mechanical properties of epoxy composites, *Carbon* 2012, 50, 5380-6.
- [49] Hanai T, Sekine K, Theory of dielectric relaxations due to the interfacial polarization for 2-component suspensions of spheres, *Colloid. Polym. Sci.* 1986, 264, 888-95.

- [50] Davis LC, Finite-element analysis of particle-particle forces in electrorheological fluids, *Appl. Phys. Lett.* 1992, 60, 319-21.
- [51] Greiner A, Wendorff JH, Electrospinning: A fascinating method for the preparation of ultrathin fibres, *Angew. Chem. Int. Edit.* 2007, 46, 5670-703.
- [52] Celebioglu A, Uyar T, Electrospinning of nanofibers from non-polymeric systems: Electrospun nanofibers from native cyclodextrins, *J. Colloid. Interf. Sci.* 2013, 404, 1-7.
- [53] Shin C, Filtration application from recycled expanded polystyrene, *J. Colloid. Interf. Sci.* 2006, 302, 267-71.
- [54] Tian LL, Prabhakaran MP, Ding X, Kai D, Ramakrishna S, Emulsion electrospun vascular endothelial growth factor encapsulated poly(l-lactic acid-co-epsilon-caprolactone) nanofibers for sustained release in cardiac tissue engineering, *J. Mater. Sci.* 2012, 47, 3272-81.
- [55] Li YF, Rubert M, Aslan H, Yu Y, Howard KA, Dong MD, Ultraporous interweaving electrospun microfibers from PCL-PEO binary blends and their inflammatory responses, *Nanoscale* 2014, 6, 3392-402.
- [56] Agarwal S, Greiner A, On the way to clean and safe electrospinning-green electrospinning: emulsion and suspension electrospinning, *Polym. Advan. Technol.* 2011, 22, 372-8.
- [57] Gopal R, Kaur S, Feng CY, Chan C, Ramakrishna S, Tabe S, Electrospun nanofibrous polysulfone membranes as pre-filters: Particulate removal, *J. Membrane. Sci.* 2007, 289, 210-9.

- [58] Boudriot U, Dersch R, Greiner A, Wendorff JH, Electrospinning approaches toward scaffold engineering - A brief overview, *Artif. Organs.* 2006, 30, 785-92.
- [59] Yoshimoto H, Shin YM, Terai H, Vacanti JP, A biodegradable nanofiber scaffold by electrospinning and its potential for bone tissue engineering, *Biomaterials* 2003, 24, 2077-82.
- [60] Patel AC, Li SX, Yuan JM, Wei Y, In situ encapsulation of horseradish peroxidase in electrospun porous silica fibers for potential biosensor applications, *Nano Lett.* 2006, 6, 1042-6.
- [61] Ding B, Kim JH, Miyazaki Y, Shiratori SM, Electrospun nanofibrous membranes coated quartz crystal microbalance as gas sensor for NH<sub>3</sub> detection, *Sensor. Actuat. B-Chem.* 2004, 101, 373-80.
- [62] Kessick R, Tepper G, Electrospun polymer composite fiber arrays for the detection and identification of volatile organic compounds, *Sensor. Actuat. B-Chem.* 2006, 117, 205-10.
- [63] Yoshida K, Kikuchi M, Park JH, Yokota S, Fabrication of micro electro-rheological valves (ER valves) by micromachining and experiments, *Sensor. Actuat. a-Phys.* 2002, 95, 227-33.
- [64] Qi MC, Shaw MT, Sedimentation-resistant electrorheological fluids based on PVAL-coated microballoons, *J. Appl. Polym. Sci.* 1997, 65, 539-47.
- [65] Jolly MR, Bender JW, Carlson JD, Properties and applications of commercial magnetorheological fluids, *J. Intel. Mat. Syst. Str.* 1999, 10, 5-

13.

- [66] Klass DL, Martinek TW, Electroviscous fluids. I. Rheological properties, *J. Appl. Phys.* 1967, 38, 67.
- [67] Klass DL, Martinek TW, Electroviscous fluids. 2. Electrical properties, *J. Appl. Phys.* 1967, 38, 75.
- [68] Stangroom JE, Electrorheological fluids, *Phys. Technol.* 1983, 14, 290-6.
- [69]Adriani PM, Gast AP, A microscopic model of electrorheology, *Phys. Fluids.* 1988, 31, 2757-68.
- [70] Klingenberg DJ, Vanswol F, Zukoski CF, The small shear rate response of electrorheological suspensions. 1. Simulation in the point-dipole limit, *J. Chem. Phys.* 1991, 94, 6160-9.
- [71] Chen Y, Sprecher AF, Conrad H, Electrostatic particle-particle interactions in electrorheological fluids, *J. Appl. Phys.* 1991, 70, 6796-803.
- [72] Anderson RA, Electrostatic forces in an ideal spherical-particle electrorheological fluid, *Langmuir* 1994, 10, 2917-28.
- [73] Clercx HJH, Bossis G, Many-body electrostatic interactions in electrorheological fluids, *Phys. Rev. E.* 1993, 48, 2721-38.
- [74] Davis LC, The metal-particle insulating oil system : An ideal electrorheological fluid, *J. Appl. Phys.* 1993, 73, 680-3.
- [75] Davis LC, Polarization forces and conductivity effects in electrorheological fluids, *J. Appl. Phys.* 1992, 72, 1334-40.
- [76] Yin JB, Guan LT, Zhao XP, Electrorheological behavior of rare earth-doped

- barium titanate suspensions, *Progress in Natural Science* 2002, 12, 278-83.
- [77] Zukoski CF, Material properties and the electrorheological response, *Annu. Rev. Mater. Sci.* 1993, 23, 45-78.
- [78] Rankin PJ, Klingenberg DJ, The electrorheology of barium titanate suspensions, *J. Rheol.* 1998, 42, 639-56.
- [79] Atten P, Foulc JN, Felici N, A conduction model of the electrorheological effect, *Int. J. Mod. Phys. B.* 1994, 8, 2731-45.
- [80] Foulc JN, Atten P, Felici N, Macroscopic model of interaction between particles in an electrorheological fluid, *J. Electrostat.* 1994, 33, 103-12.
- [81] Hao T, Kawai A, Ikazaki F, Mechanism of the electrorheological effect: Evidence from the conductive, dielectric, and surface characteristics of water-free electrorheological fluids, *Langmuir* 1998, 14, 1256-62.
- [82] Hao T, Kawai A, Ikazaki F, Dielectric criteria for the electrorheological effect, *Langmuir* 1999, 15, 918-21.
- [83] Hao T, Kawai A, Ikazaki F, The yield stress equation for the electrorheological fluids, *Langmuir* 2000, 16, 3058-66.
- [84] Hao T, Xu ZM, Xu YZ, Correlation of the dielectric properties of dispersed particles with the electrorheological effect, *J. Colloid. Interf. Sci.* 1997, 190, 334-40.
- [85] J.E. Stangroom, *GB Patent* 1983, 2119392.
- [86] H. Block, J.P. Kelley, *US Patent* 1987, 1501635.
- [87] W.M. Winslow, *U.S. Patent* 1947, 2417850.

- [88] Xu YZ, Liang RF, Electrorheological properties of semiconducting polymer-based suspensions, *J. Rheol.* 1991, 35, 1355-73.
- [89] Hao T, The interfacial polarization-induced electrorheological effect, *J. Colloid. Interf. Sci.* 1998, 206, 240-6.
- [90] Wagner KW, The theory of incomplete dielectricity, *Ann. Phys-Berlin.* 1913, 40, 817-55.
- [91] Morgan SO, Yager WA, White AH, Dielectric polarization in solids, *J. Am. Chem. Soc.* 1933, 55, 2171-2.
- [92] Jones TK, Scott RA, Sillars RW, The structure and electrical properties of surfaces of semiconductors. 1. Silicon carbide, *P. Phys. Soc. Lond. A.* 1949, 62, 333.
- [93] Weiss KD, Margida AJ, Carlson JD, Nixon DA, ER fluid inks : A rainbow of possibilities, *Abstr. Pap. Am. Chem. S.* 1994, 208, 20.
- [94] Deinega YF, Popko KK, Kovganich NY, Temperature dependence of the electroviscous effect and dielectric parameters of suspensions of hydrated substances in hydrocarbons, *Heat Transfer-Sov. Res.* 1978, 10, 50.
- [95] Kawai A, Uchida K, Kamiya K, Gotoh A, Yoda S, Urabe K, Effect of dielectric property of hydrous dispersoid on electrorheology, *Int. J. Mod. Phys. B.* 1996, 10, 2849-55.
- [96] Ikazaki F, Kawai A, Uchida K, Kawakami T, Edamura K, Sakurai K, Mechanisms of electrorheology: The effect of the dielectric property, *J. Phys. D. Appl. Phys.* 1998, 31, 336-47.

- [97] Klingenberg DJ, Zukoski CF, Studies on the steady-shear behavior of electrorheological suspensions, *Langmuir* 1990, 6, 15-24.
- [98] Bossis G, Lemaire E, Volkova O, Clercx H, Yield stress in magnetorheological and electrorheological fluids: A comparison between microscopic and macroscopic structural models, *J. Rheol.* 1997, 41, 687-704.
- [99] Hao T, Xu YZ, Chen YH, Xu M, Dielectric polarization of electrorheological suspensions, *Chinese. Phys. Lett.* 1995, 12, 573-6.
- [100] Conrad H, Sprecher AF, Choi Y, Chen Y, The temperature-dependence of the electrical-properties and strength of electrorheological fluids, *J. Rheol.* 1991, 35, 1393-410.
- [101] Treasurer UY, Filisko FE, Radzilowski LH, Polyelectrolytes as inclusions in electrorheologically active materials : Effect of chemical characteristics on ER activity, *J. Rheol.* 1991, 35, 1051-68.
- [102] H. Block, J.P. Kelly, *GB Patent* 1985, 2170510.
- [103] D.G. Bytt, *GB Patent* 1987, 2189803.
- [104] F.E. Filisko, W.E. Amstrong, *U.S. Patent* 1988, 4744914.
- [105] Wysocki JJ, Adams J, Haas W, Electroviscosity of a cholesteric liquid-crystal mixture, *J. Appl. Phys.* 1969, 40, 3865.
- [106] Honda T, Sasada T, Electroviscous effect in n-hexane/acetone mixtures, *Jpn. J. Appl. Phys.* 1978, 17, 2075-6.
- [107] Yang IK, Shine AD, Electrorheology of a nematic poly(normal-hexyl

- isocyanate) solution, *J. Rheol.* 1992, 36, 1079-104.
- [108] Tajiri K, Ohta K, Nagaya T, Orihara H, Ishibashi Y, Doi M, Electrorheological effect in immiscible polymer blends, *J. Rheol.* 1997, 41, 335-41.
- [109] Yao N, Jamieson AM, Electrorheological behavior of side-chain liquid-crystalline polysiloxanes in nematic solvents, *Macromolecules* 1997, 30, 5822-31.
- [110] Negita K, Electrorheological effect in the nematic phase of 4-n-pentyl-4'-cyanobiphenyl, *J. Chem. Phys.* 1996, 105, 7837-41.
- [111] Ha JW, Yang SM, Rheological responses of oil-in-oil emulsions in an electric field, *J. Rheol.* 2000, 44, 235-56.
- [112] Choi SB, Lee TH, Lee YS, Han MS, Control performance of an electrorheological valve based vehicle anti-lock brake system, considering the braking force distribution, *Smart. Mater. Struct.* 2005, 14, 1483-92.
- [113] Han YM, Nguyen QH, Choi SB, Unsteady flow modeling of an electrorheological valve system with experimental validation, *Smart. Mater. Struct.* 2009, 18, 085005.
- [114] Monkman GJ, Dielectrophoretic enhancement of electrorheological robotic actuators, *Mechatronics* 1993, 3, 305-13.
- [115] Krivenkov K, Ulrich S, Bruns R, Extending the operation range of electrorheological actuators for vibration control through novel designs, *J. Intel. Mat. Syst. Str.* 2012, 23, 1323-30.

- [116] Shulman ZP, Korobko EV, Levin ML, Binshtok AE, Bilyk VA, Yanovsky YG, Energy dissipation in electrorheological damping devices, *J. Intel. Mat. Syst. Str.* 2006, 17, 315-20.
- [117] Choi SB, Lee DY, Rotational motion control of a washing machine using electrorheological clutches and brakes, *P. I. Mech. Eng. C-J. Mec.* 2005, 219, 627-37.
- [118] Hartsock DL, Novak RF, Chaundy GJ, ER fluid requirements for automotive devices, *J. Rheol.* 1991, 35, 1305-26.
- [119] Liu YJ, Davidson R, Taylor P, Touch sensitive electrorheological fluid based tactile display, *Smart. Mater. Struct.* 2005, 14, 1563-8.
- [120] Liu YD, Lee BM, Park TS, Kim JE, Choi HJ, Booh SW, Optically transparent electrorheological fluid with urea-modified silica nanoparticles and its haptic display application, *J. Colloid. Interf. Sci.* 2013, 404, 56-61.
- [121] Garg DP, Anderson GL, Structural damping and vibration control via smart sensors and actuators, *J. Vib. Control.* 2003, 9, 1421-52.
- [122] Novoselov KS, Geim AK, Morozov SV, Jiang D, Zhang Y, Dubonos SV, Electric field effect in atomically thin carbon films, *Science* 2004, 306, 666-9.
- [123] Iijima S, Helical microtubules of graphitic carbon, *Nature* 1991, 354, 56-8.
- [124] Kroto HW, Heath JR, O'Brien SC, Curl RF, Smalley RE, C60: Buckminsterfullerene, *Nature* 1985, 318, 162-3.

- [125] Fuhrer MS, Lau CN, MacDonald AH, Graphene: Materially better carbon, *Mrs. Bull.* 2010, 35, 289-95.
- [126] Sarma SD, Life cycle of a nanosilver based water candle filter: Examining issues of toxicity, risks, challenges and policy implications, *J. Biomed. Nanotechnol.* 2011, 7, 83-4.
- [127] Peres NMR, Colloquium: The transport properties of graphene: An introduction, *Rev. Mod. Phys.* 2010, 82, 2673-700.
- [128] Bonaccorso F, Sun Z, Hasan T, Ferrari AC, Graphene photonics and optoelectronics, *Nat. Photonics.* 2010, 4, 611-22.
- [129] Thompson BC, Frechet JMJ, Organic photovoltaics: Polymer-fullerene composite solar cells, *Angew. Chem. Int. Edit.* 2008, 47, 58-77.
- [130] Brabec CJ, Gowrisanker S, Halls JJM, Laird D, Jia SJ, Williams SP, Polymer-fullerene bulk-heterojunction solar cells, *Adv. Mater.* 2010, 22, 3839-56.
- [131] Yang WR, Ratinac KR, Ringer SP, Thordarson P, Gooding JJ, Braet F, Carbon nanomaterials in biosensors: Should you use nanotubes or graphene?, *Angew. Chem. Int. Edit.* 2010, 49, 2114-38.
- [132] Pumera M, Ambrosi A, Bonanni A, Chng ELK, Poh HL, Graphene for electrochemical sensing and biosensing, *Trac-Trend. Anal. Chem.* 2010, 29, 954-65.
- [133] Liu YX, Dong XC, Chen P, Biological and chemical sensors based on graphene materials, *Chem. Soc. Rev.* 2012, 41, 2283-307.

- [134] Tian HC, Liu JQ, Wei DX, Kang XY, Zhang C, Du JC, Graphene oxide doped conducting polymer nanocomposite film for electrode-tissue interface, *Biomaterials* 2014, 35, 2120-9.
- [135] Nezakati T, Tan A, Seifalian AM, Enhancing the electrical conductivity of a mixture POSS-PCL/graphene nanocomposite polymer, *J. Colloid. Interf. Sci.* 2014, 435, 145-55.
- [136] Yu DR, Kim GH, Effects of multi-walled carbon nanotube (MWCNT) content on physical properties and cell structure in ethylene vinyl acetate copolymer (EVA)/MWCNT nanocomposite foams, *Polym-Plast. Technol.* 2013, 52, 699-703.
- [137] Bianco A, Kostarelos K, Partidos CD, Prato M, Biomedical applications of functionalised carbon nanotubes, *Chem. Commun.* 2005, 571-7.
- [138] Slonczewski JC, Weiss PR, Band structure of graphite, *Phys. Rev.* 1958, 109, 272-9.
- [139] McClure JW, Diamagnetism of graphite, *Phys. Rev.* 1956, 104, 666-71.
- [140] Wallace PR, The band theory of graphite, *Phys. Rev.* 1947, 71, 476.
- [141] Haldane FDM, Model for a quantum Hall-effect without Landau levels: Condensed-matter realization of the “parity anomaly”, *Phys. Rev. Lett.* 1988, 61, 2015-8.
- [142] Fradkin E, Critical-behavior of disordered degenerate semiconductors. 2. Spectrum and transport-properties in mean-field theory, *Phys. Rev. B.* 1986, 33, 3263-8.

- [143] Semenoff GW, Condensed-matter simulation of a 3-dimensional anomaly, *Phys. Rev. Lett.* 1984, 53, 2449-52.
- [144] Zhang YB, Tan YW, Stormer HL, Kim P, Experimental observation of the quantum Hall effect and Berry's phase in graphene, *Nature* 2005, 438, 201-4.
- [145] Novoselov KS, Geim AK, Morozov SV, Jiang D, Katsnelson MI, Grigorieva IV, Two-dimensional gas of massless Dirac fermions in graphene, *Nature* 2005, 438, 197-200.
- [146] Lee C, Wei XD, Kysar JW, Hone J, Measurement of the elastic properties and intrinsic strength of monolayer graphene, *Science* 2008, 321, 385-8.
- [147] Hoffman DM, Heinz RE, Doll GL, Eklund PC, Optical reflectance study of the electronic-structure of acceptor-type graphite-intercalation compounds, *Phys. Rev. B.* 1985, 32, 1278-88.
- [148] MacKenzie JD, Sol-gel research: Achievements since 1981 and prospects for the future, *J. Sol-Gel Sci. Techn.* 2003, 26, 23-7.
- [149] Blum J, Rosenfeld A, Gelman F, Schumann H, Avnir D, Hydrogenation and dehalogenation of aryl chlorides and fluorides by the sol-gel entrapped RhCl(3), -Aliquat 336 ion pair catalyst, *J. Mol. Catal. a-Chem.* 1999, 146, 117-22.
- [150] Schubert U, Catalysts made of organic-inorganic mixture materials, *New J. Chem.* 1994, 18, 1049-58.
- [151] Lin J, Brown CW, Sol-gel glass as a matrix for chemical and biochemical

- sensing, *Trac.Trend. Anal. Chem.* 1997, 16, 200-11.
- [152] Banet P, Cantau C, Rivron C, Tran-Thi TH, Nanoporous sponges and proven chemical reactions for the trapping and sensing of halogenated gaseous compounds, *Actual Chimique* 2009, 30-5.
- [153] Xomeritakis G, Tsai CY, Jiang YB, Brinker CJ, Tubular ceramic-supported sol-gel silica-based membranes for flue gas carbon dioxide capture and sequestration, *J. Membrane. Sci.* 2009, 341, 30-6.
- [154] Zeng ZR, Qiu WL, Yang M, Wei X, Huang ZF, Li F, Solid-phase microextraction of monocyclic aromatic amines using novel fibers coated with crown ether, *J. Chromatogr. A.* 2001, 934, 51-7.
- [155] Gvishi R, Narang U, Ruland G, Kumar DN, Prasad PN, Novel, organically doped, sol-gel-derived materials for photonics: Multiphase nanostructured composite monoliths and optical fibers, *Appl. Organomet. Chem.* 1997, 11, 107-27.
- [156] Levy D, Recent applications of photochromic sol-gel materials, *Mol. Cryst. Liq. Cryst. A.* 1997, 297, 31.
- [157] Dunn B, Zink JJ, Optical-properties of sol-gel glasses doped with organic-molecules, *J. Mater. Chem.* 1991, 1, 903-13.
- [158] Levy D, Esquivias L, Sol-gel processing of optical and electrooptical materials, *Adv. Mater.* 1995, 7, 120-9.
- [159] Dunn B, Farrington GC, Katz B, Sol-gel approaches for solid electrolytes and electrode materials, *Solid State Ionics* 1994, 70, 3-10.

- [160] Dulay MT, Quirino JP, Bennett BD, Zare RN, Bonded-phase photopolymerized sol-gel monoliths for reversed phase capillary electrochromatography, *J. Sep. Sci.* 2002, 25, 3-9.
- [161] Doshi J, Reneker DH, Electrospinning process and applications of electrospun fibers, *J. Electrostat.* 1995, 35, 151-60.
- [162] Son WK, Youk JH, Lee TS, Park WH, The effects of solution properties and polyelectrolyte on electrospinning of ultrafine poly(ethylene oxide) fibers, *Polymer* 2004, 45, 2959-66.
- [163] Huang ZM, He CL, Yang AZ, Zhang YZ, Hang XJ, Yin JL, Encapsulating drugs in biodegradable ultrafine fibers through co-axial electrospinning, *J. Biomed. Mater. Res. A.* 2006, 77, 169-79.
- [164] Peng XH, Santulli AC, Sutter E, Wong SS, Fabrication and enhanced photocatalytic activity of inorganic core-shell nanofibers produced by coaxial electrospinning, *Chem. Sci.* 2012, 3, 1262-72.
- [165] Yu Y, Gu L, Wang CL, Dhanabalan A, van Aken PA, Maier J, Encapsulation of Sn@carbon nanoparticles in bamboo-like hollow carbon nanofibers as an anode material in lithium-based batteries, *Angew. Chem. Int. Edit.* 2009, 48, 6485-9.
- [166] Yang YK, Qiu SQ, Cui W, Zhao Q, Cheng XJ, Li RKY, A facile method to fabricate silica-coated carbon nanotubes and silica nanotubes from carbon nanotubes templates, *J. Mater. Sci.* 2009, 44, 4539-45.
- [167] Wang XF, Fernando KAS, Watson V, Bunker CE, Synthesis of graphene

- oxide from graphite using modified Hummer's method and related studies, *Abstr. Pap. Am. Chem. S.* 2012, 244.
- [168] Liu YY, Tang J, Chen XQ, Wang RH, Pang GKH, Zhang YH, Carbon nanotube seeded sol-gel synthesis of silica nano-particle assemblies, *Carbon* 2006, 44, 165-7.
- [169] Kim M, Hong J, Lee J, Hong CK, Shim SE, Fabrication of silica nanotubes using silica coated multi-walled carbon nanotubes as the template, *J. Colloid. Interf. Sci.* 2008, 322, 321-6.
- [170] Ramasamy P, Seo DM, Kim SH, Kim J, Effects of TiO<sub>2</sub> shells on optical and thermal properties of silver nanowires, *J. Mater. Chem.* 2012, 22, 11651-7.
- [171] Lee D, Kim JW, Kim BG, A new parameter to control heat transport in nanofluids: Surface charge state of the particle in suspension, *J. Phys. Chem. B.* 2006, 110, 4323-8.
- [172] Cho MS, Choi HJ, To KW, Effect of ionic pendent groups on a polyaniline-based electrorheological fluid, *Macromol. Rapid. Comm.* 1998, 19, 271-3.
- [173] Wu JH, Xu GJ, Cheng YC, Liu FH, Guo JJ, Cui P, The influence of high dielectric constant core on the activity of core-shell structure electrorheological fluid, *J. Colloid. Interf. Sci.* 2012, 378, 36-43.
- [174] Yin JB, Xia X, Wang XX, Zhao XP, The electrorheological effect and dielectric properties of suspensions containing polyaniline@titania

nanocable-like particles, *Soft Matter* 2011, 7, 10978-86.

- [175] Song T, Zhang YZ, Zhou TJ, Lim CT, Ramakrishna S, Liu B, Encapsulation of self-assembled FePt magnetic nanoparticles in PCL nanofibers by coaxial electrospinning, *Chem. Phys. Lett.* 2005, 415, 317-22.
- [176] McCann JT, Li D, Xia YN, Electrospinning of nanofibers with core-sheath, hollow, or porous structures, *J. Mater. Chem.* 2005, 15, 735-8.
- [177] Li D, Xia YN, Electrospinning of nanofibers: Reinventing the wheel?, *Adv. Mater.* 2004, 16, 1151-70.

## Korean Abstract

전기유변(Electo-Rheological, 전기변성) 유체는 전기장 인가 시 고체의 성질로 변화하는 유체로서, 차량용 엔진 마운트, 클러치, 댐퍼 및 각종 전기적 제어가 필요한 기계부품에 사용되는 특수 유체이다.

전기유변유체는 비전도성 유체 내부에 전기유변입자들이 분산되어 있어 전기장이 가해지면 입자 내부의 전하가 분리되고 이들 입자들 사이에 정전기적인 힘이 작용하여 전기장 방향으로 입자들이 배열하게 된다. 이는 유체의 유동을 억제함으로써 순간적으로 유체의 점성을 증가시킨다. 이러한 변화는 가변적이며, 수 마이크로 초로 매우 빠르게 일어난다.

기존 전기유변입자는 수 마이크로 사이즈로서 다양한 단점을 가지고 있고 이를 극복하기 위한 다양한 물질이 개발되고 있다. 최근 1 디멘전한 모폴로지를 가지며 다른 특성을 갖는 2 가지 물질을 하이브리드하여 각자의 특성을 부각시켜 시너지 효과를 이루기 위한 연구들이 진행되고 있다.

본 연구에서는 기존의 전기유변입자가 갖는 다양한 단점(낮은 전단응력, 낮은 분산안정성,)을 극복하고 산업적 응용을 앞당기기 위해 카본나노물질을 지지체로 이용하고 졸-겔 합성법을 통해 유전특성을 갖는 무기물이 코팅된 전기유변입자를 제조하고 이의 ER 특성을 관찰하였다. 유전율이 상이한 무기물질에 따른 ER 특성, 코팅 두께 변화에 따른 ER 특성과 코팅물질의 코팅배열 변화에 따른 ER 특성을 분석하였다. ER 유체의 분산안정성 및 온도의존성 또한 분석, 평가하였다. 이는 탄소나노재료가 갖는 비표면적, 비중, 기계적 특성과 무기물질이 갖는 유전특성을 함께 구현하고 시너지를 극대화하여 높은 전기반응형 유체를 제작하였다. 또한 dual core 노즐 전기방사 장치를 이용하여 섬유내부로 ER 유체를 함침시켜 제조된 복합재료는 전기장 하에서 기계적 특성이 향상되는 스마트한 성질을 보였다.

유전율이 상대적으로 큰 티타니아가 코팅된 카보나노튜브 유체가 실리카가 코팅된 카본나노튜브 유체보다 더 높은 전단응력을 보였지만 전기장하에서 산화반응을 보이는 metal oxide 의 경우 전류밀도를 증가시키는 요인으로 인해 전기장의 세기 증가에 한계를 주었다. 코팅 두께를 달리하여 제조된 실리카 코팅 카보나노튜브 유체를 통해 전기유변입자가 필요로하는 적정한 전도도가 존재하며 이를 충족시킬 시에 전기장하에서 전단응력의 향상을 준다는 것을

알 수 있었다. 티타니아 코팅된 카본나노튜브의 경우 높은 전류밀도의 감소를 위해 2 중 코팅을 실시하였으며, 이는 전류밀도를 낮추고 전단응력을 향상시킬 수 있었다. 그래핀과 카본나노튜브의 ER 에 차이를 확인하기 위해서 동일하게 티타니아가 코팅된 ER 물질을 제조하고 이의 전기유변특성을 관찰하였다. 카본나노튜브보다 그래핀에 의해 제조된 유체가 더 낮은 전기전도도와 높은 비표면적으로 인해 더 높은 ER 특성을 얻었다.

마지막으로 전기유변유체가 함침된 core/sheath 구조를 갖는 섬유 웹의 제작을 통해 전기장의 증가와 코어입자의 양의 증가와 함께 기계적 특성이 향상됨을 확인하였다. 이는 스마트 복합재료로의 응용을 가능하게 할 것으로 기대된다.

**주요어:** 탄소나노물질, 무기물코팅, 전기유변유체, 지능형복합재료

**학 번:** 2006-23054